北海道大学
HOKKAIDO UNIVERSITY

Meteorological application of a dense GNSS network utilizing atmospheric delay gradient and crustal subsidence: The 2018 disastrous rain episode in SW Japan

大気遅延勾配と地殻上下変動を利用した稠密 GNSS 網の
気象学的応用：平成 30 年 7 月豪雨の事例研究

by

Syachrul Arief

シャフルル・アリーフ

A thesis submitted for the degree of Doctor of Philosophy

Department of Natural History Sciences,
Graduate School of Science, Hokkaido University

September 2020

Abstract

Heavy rain from late June to early July 2018 brought disastrous flood in Southwest (SW) Japan, especially in Kyushu. By using a dense array of Global Navigation Satellite System (GNSS) receivers in Japan GEONET, I study this episode with two different space geodetic approaches, i.e., measurements of atmospheric water vapor and crustal deformation due to surface water load.

The first approach is the recovery of precipitable water vapor (PWV) using the zenith wet delays (ZWD). Because atmospheric water vapor concentrates in relatively low altitudes, 2-D distribution of ZWDs often represent that of elevation of the observing stations rather than the relative humidity of the air column above the stations. To overcome the difficulty, I reconstructed ZWDs converted to sea-level values by spatially integrating the tropospheric delay gradient (azimuthal asymmetry of water vapor) vectors from coastal GNSS stations. I also calculated convergence of such delay gradients, equivalent to water vapor convergence (WVC) index proposed by Shoji (2013). I found that extreme rainfall occurs in the region and time, where both the sea-level ZWD and the WVC index are high. I confirmed this was the case also for similar disastrous heavy rain episodes in SW Japan in 2017 July and 2019 August.

Next, I studied vertical crustal movements associated with surface water loads brought by heavy rainfall, using the official F3 solution of the GEONET station coordinates. Rainwater would act as the surface load and depress the ground to a detectable level. I removed common mode errors by adjusting ~100 reference stations to the median positions over a 1-month period using the Helmert transformation. I confirm land subsided by up to ~ 2 cm in some areas where major floods occurred. Land subsidence was observed to recover with a time constant of 1-2 days, which reflects the rapid drainage of rainwater into the sea due to the large topographic slope of the Japanese Islands and the proximity of the flooded areas to the sea. Then, I estimated the distribution of surface water load over the entire SW Japan using the GNSS station subsidence as the input. The estimated distribution of surface water resembled to the rainfall distribution from the AMEDAS rain gauge data from Japan Meteorological Agency (JMA).

Then, I compared the amount of water of the 2018 heavy rain episode using the three ways, i.e. (1) spatially integrated PWV, (2) cumulative rainfall from AMEDAS rain gage, and (3) surface water distribution estimated from crustal subsidence. Cumulative rain was larger than atmospheric PWV, which is reasonable considering that

29 the atmospheric water vapor only represents the capacity of the “bucket” to carry seawater to land. Regarding the
30 comparison of the rain gauge data and the surface water estimated from crustal subsidence, the latter largely
31 exceeded the former. One may point out that the AMEDAS stations tend to be built in low-altitude valleys and
32 may not represent true amount of rainfall over the whole land. I compared cumulative rain from the AMeDAS
33 rainfall data and radar rain-gauge analyzed precipitation and confirmed that AMeDAS rain gauge data do not
34 seriously underestimate real precipitation. The problem may come from the GEONET station distributions. They
35 tend to be located in low-elevation densely populated area, and stormwater may concentrate on their vicinity.
36 Thick sedimentary layers beneath the GEONET stations may also locally reduce the crustal rigidity.

37 I performed similar studies using GNSS data taken at stations in Indonesia. I processed the raw GNSS data to
38 estimate ZTD and PWV values using open-source software packages such as goGPS. I validated the derived
39 tropospheric parameters by comparing them with those from other research centers, such as University of Nevada
40 Reno (UNR). Next, I applied the methods to the disastrous heavy rain events that caused floods in Jakarta in early
41 January 2020 and studied the time series of PWV and vertical coordinates. I confirmed the enhancement of PWV
42 prior to the heavy rainfall onset and significant subsidence of GNSS stations located in the flooded area.

43

Acknowledgments

I would like to thank my supervisor, Prof. Kosuke Heki, for his support, encouragement, and guidance for four years. The time he spent working with me has greatly improved the quality and increased the depth of this research,

I would also like to express my gratitude to all my colleagues in the Space Geodesy laboratory and Seismology Laboratory, Faculty of Science Hokkaido University. Specifically to teachers: Prof. Furuya and Dr. Youichiro Takada were always actively giving input in the "Zemi" week when I made presentations,

I also would like to thank Prof. Kiyoshi Yomogida and Dr. Kazunori Yoshizawa for their constructive comments. For all of Natural History Science Department members, many thank for all of your supports, also for the BIG, RISET-PRO KEMRISTEKDIKTI Scholarship program from the Indonesian Government,

I also visited MRI/JMA (Meteorological Research Institute/Japan Meteorological Agency) in Tsukuba and met Dr. Yoshinori Shoji, for discussions related to GNSS Meteorology in Japan. Thank you very much for the input in the preparation of this thesis.

I also want to thank the staff at the Faculty and the Graduate School of Sciences who helped me both in the learning process and interactions with the environment while in Sapporo,

Finally, I also thank my family, my wife, my daughter, and my younger brother, for giving me freedom and support throughout my education to make me think that anything is possible. Without their encouragement and understanding for years, I would not have been able to complete this research process.

Contents

Chapter 1. Introduction

1.1 Background

One of the similarities between Indonesia and Japan is their geographical setting. The both countries belong to Asia. Besides the geographical similarity, Indonesia and Japan are also located in the Asia-Pacific ring-of-fire where multiple tectonic plates meet. This brings these two countries natural disasters such as volcanic eruptions, large earthquakes, and tsunamis. In addition to such solid earth origin disasters, the two countries suffer from floods caused by heavy rains. For this kind of natural disasters, we should explore common methods to mitigate them. Such a meteorological disaster often causes a lot of casualties and losses of properties. In this study, I pick up the occurrence of a disastrous heavy rain episode that attacked SW Japan in early July 2018. In Indonesia, I focus on the heavy rain that occurred early in January 2020 in Jakarta.

In recent times, they deployed many ground stations tracking satellites of Global Navigation Satellite System (GNSS), including the American Global Positioning System (GPS). People have been using them not only for positioning and crustal deformation studies, but also for various fields especially for remote sensing of atmosphere, such as tropospheric water vapor and ionospheric electrons. Among others, the new word “GNSS (GPS) meteorology” was introduced by Bevis et al. (1992) to signify researches making use of GNSS for sensing of the earth’s atmosphere using the delay of microwave signals from GNSS satellites. This changed the mind of researchers who considered atmospheric refraction of GNSS signals just an error affecting the positioning accuracies.

In this research, I used the approach of ground-based GNSS-meteorology and give its technical and theoretical explanations in Chapter 2. GNSS Meteorology has many advantages as listed below.

- GNSS data are not affected by weather conditions, i.e. GNSS is an all-weather sensor.

- GNSS data are continuously acquired using permanent ground stations.

- GNSS data has a high temporal resolution with typical sampling interval of 30 seconds.

- GNSS has high accuracy for the estimation of tropospheric delays and its azimuthal asymmetry.

- GNSS is not dependent on other meteorological instruments. GNSS stations are sometimes equipped with meteorological sensors, but GNSS data can be obtained independently.

- GNSS data has a long-term stability suitable for studying climate changes.

As a conventional sensor of atmospheric water vapor, we have been using radiosonde and water vapor radiometers. Radiosonde can make vertical humidity profiles, but it is operated only twice a day in only 10-20 stations in Japan. Water vapor radiometers are not suitable for measurements during rain. In contrast, we have ~1,300 permanent GNSS stations called GEONET (GNSS Earth Observation Network) operated by GSI (Geospatial Information Authority) recording data every 30 seconds regardless of weather conditions. Hence, GNSS-meteorology is a promising technique for meteorology and climatology in Japan.

1.2 GNSS Meteorology in Japan and in Indonesia

As the institutions participating the GNSS meteorology project, “GNSS/MET Japan”, two essential organizations in Japan started cooperation, GSI and JMA. GSI is the mapping agency of the Japanese government, and it operates the nationwide GEONET with the primary purpose as the dense land survey infrastructure and sensors of crustal deformation. On the other hand, JMA is responsible for providing information on weather, climate, ocean, volcanoes, and earthquakes in Japan and for maintaining the equipment for relevant observations.

GNSS meteorology in Japan entered the stage of implementing concrete actions supported by the two institutions. According to Shoji et al. (2009), the early research activity started when Japanese geodesists and meteorologists held the first workshop on "GNSS Tropospheric Delay" at the Mizusawa Astrogeodynamic Observatory, National Astronomical Observatory (NAO), Japan, being led by Isao Naito of NAO. There, they recognized the importance of water vapor information from GNSS data with the advice of Nobutaka Man’nouji of JMA. After a feasibility study led by Hiromichi Tsuji of GSI, the Japanese GNSS meteorology project "GNSS/MET JAPAN" was launched in 1997. The detail of the "GNSS/MET JAPAN" project is compiled in the special issue of Earth Planets and Space published in 1998 (Tsuda et al., 1998).

PWV data from GNSS have been assimilated in the mesoscale model of JMA to improve weather forecast accuracy since 2009 (Shoji, 2015). The latest developments in GNSS meteorology in Japan includes the recent innovation for receiving GNSS signals on the sea. Shoji et al. (2017) installed GNSS antennas on a JMA's research

192 vessel and estimated tropospheric parameters such as PWV. They confirmed that their results agree with PWV
193 from radiosonde observations.

194 From the perspective of geodesy, Heki (2020) suggested that geodesy would play a transdisciplinary role in Japan
195 in future. He gave an example of meteorological application of the dense GNSS network through the measurement
196 of PWV and crustal subsidence caused by surface stormwater. I follow this concept in this study, i.e. I tried to
197 study the 2018 heavy rain episode in SW Japan from multiple aspects using GNSS. One of them is the PWV
198 approach (Chapter 3) and the other is the crustal movement approach (Chapter 4). I am finishing my PhD study
199 with the hope that it can further enhance the transdisciplinary nature of GNSS and geodesy in Japan and the world.

200 Next, what about the GNSS meteorology in Indonesia? In Indonesia, the number of GNSS stations is still around
201 200 in spite of its large geographical dimension. The density of the GNSS station is much less than in Japan,
202 where ~1300 stations are deployed. As for the GNSS meteorological researches in Indonesia, I found several
203 theses by students at the university of higher education. For example, the Master Thesis by Susilo, with the title
204 "Monitoring Precipitable Water Vapor (PWV) in the West Java Region Using Continuous GNSS", followed by
205 an undergraduate thesis by Fikri Bamahry with the title "PWV Monitoring Over East Java Region Using
206 Continuous GNSS".

207 Because the distribution of GNSS stations is still limited in number, the spatial approach of GNSS meteorology
208 (e.g. detailed mapping of water vapor distribution) is still difficult, and the studies are limited to those by the
209 temporal approach (e.g. time series analysis of water vapor at a certain station). In general, they only discuss how
210 to determine the value of PWV in Indonesia using commercial software packages. So far, there are no real political
211 movements driven by the Indonesian government for GNSS meteorology.

212 In this research, I will try to apply the GNSS meteorological approach for real phenomena in Indonesia with the
213 hope of making GNSS meteorology a part of the new policy put forward in Indonesia. The first part for the case
214 in Indonesia, I will estimate tropospheric parameters from raw GNSS data available in the Receiver-INdependent
215 EXchange format (RINEX format). Then I demonstrate how to determine the PWV values with the open-source
216 software packages. They are described in Chapter 5. In Chapter 6, I study the heavy rain episode in January 2020
217 in Jakarta, and try to detect crustal subsidence analyzing the time series of PWV and vertical coordinates of GNSS
218 stations.

219

1.3 Research Objectives

In general, the purpose of this study is to explore how GNSS can be used for meteorological purposes including its potential for studying crustal movements due to heavy rains. I study the cases of heavy rains in Kyushu, Japan, in 2017-2019 and in Jakarta, Indonesia, in 2020.

What I did in this study is summarized as follows.

1. To demonstrate the benefit of utilizing tropospheric delay gradients.

2. To analyze PWV to improve our understanding of water vapor dynamics during heavy rains.

3. To calculate water vapor concentration (WVC) index and study its behavior together with the in-situ rainfall data from AMEDAS (Automated Meteorological Data Acquisition System) stations of JMA.

4. To study the temporal evolution of these quantities during the three heavy rain episodes in SW Japan in summer 2017-2019.

5. To analyze the role of heavy rain as a carrier of water in July 2018 in SW Japan, by inverting surface water distribution using vertical crustal movement data.

6. To obtain tropospheric parameters from Indonesian GNSS network (INACORS-BIG) RINEX data.

7. To study PWV behaviors before and after the heavy rain episode in early 2020 in Jakarta.

8. To reveal vertical crustal movements during heavy rain episode in Jakarta in early 2020.

1.4 Thesis Structure

The structure of this thesis starts from the explanation of the background, why the research was performed, what is the importance of this research, how the research was conducted and what is expected to be achieved in this research. Then I describe the overview of the objectives of this study in general and specifically. The ending of Chapter 1 is the explanation of the structure of this thesis.

Chapter 2 contains the basics of the ground-based GNSS Meteorology, from the description of atmospheric layers to methods to estimate tropospheric delays.

In Chapter 3, I tried to apply the GNSS meteorology to the disastrous heavy rainfall in SW Japan in July 2018 using tropospheric data from the UNR data base.

In Chapter 4, for the case of heavy rainfall in early July 2018, I studied crustal subsidence by water load using the daily coordinate data from the dense GNSS network. In this chapter I reveal the link between precipitation and the deformation of underlying crust.

In Chapter 5, I describe the GNSS meteorology studies in Indonesia. It starts with the demonstration of the estimation of zenith total delay (ZTD) values from raw GNSS data given in RINEX format using the goGPS open-source software. I confirmed the accuracy of the estimated tropospheric parameter with the results from International GNSS Service (IGS) and UNR.

In Chapter 6, concerning the meteorological application of GNSS in Indonesia, I tried to apply it to the torrential rain events that caused flooding in Jakarta in early January 2020. Here I also detected the vertical crustal movements associated with the heavy rainfalls in Jakarta.

Finally, in Chapter 7, I present the conclusions of the whole content of this thesis and make recommendations for future.

.

Chapter 2. Ground-based GNSS Meteorology

In this chapter, I will write about the fundamental principles of GNSS meteorology. Starting with the explanations of atmospheric layers, path delay, and refractivity, how to retrieve PWV from GNSS-derived zenith delays. Then I write on the models used for the determination of tropospheric delay parameters.

Based on the position of the GNSS receivers for monitoring atmospheric properties, GNSS meteorology can be classified into two basic categories (Businger et al. 1996), namely the space-based and the ground-based GNSS Meteorology. In the space-based GNSS meteorology, they receive microwave signals with receivers on board Low Earth Orbit (LEO) satellites with near-global coverage. Received signals are processed to obtain profiles of atmospheric refractivity. This method is also called as GNSS Radio Occultation (GNSS-RO) (Ware et al. 1996). The refractivity profiles are converted to profiles of various atmospheric properties such as temperature, water vapor content in the lower part of atmosphere, and electron density in the ionosphere. In the ground-based GNSS meteorology, they receive phases of microwave signals at points fixed on the ground, and estimate atmospheric delays (due to dry air and water vapor) included in the phase observables. Figure 2.1 compares the space-based and the ground-based GNSS meteorology.

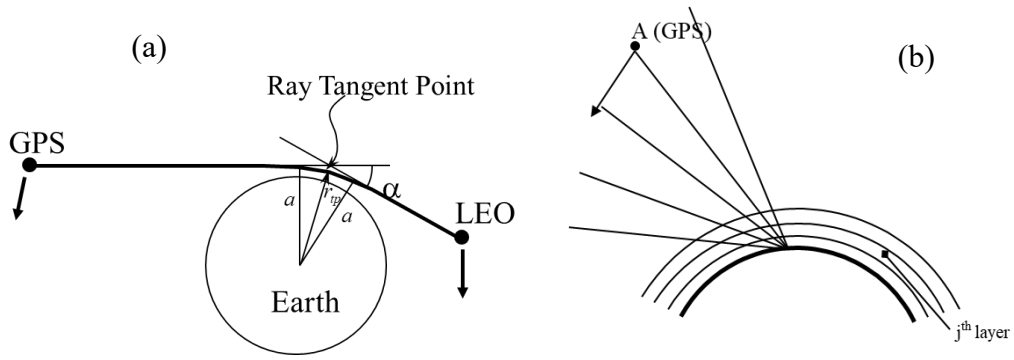

Figure 2.1 (a) Space-based GNSS meteorology to obtain refractivity profiles of the atmosphere, and (b) ground-based GNSS meteorology to estimate atmospheric delay of the GNSS signal, or "zenith tropospheric delay (ZTD)". Such delay is converted to "precipitable water vapor (PWV)". (*by Christian Rocken GCOS, May 2006*).

2.1 Atmosphere Layers

The solid Earth is surrounded by various kinds of gases which constitute the Earth's atmosphere. Most of the atmosphere (about 80% in weight) is within 16 km of the surface of the Earth. There are no exact "higher ends" of the atmosphere. It just gets thinner and thinner until it merges with the space. The atmosphere of the Earth can

be divided into several distinct layers, thereby facilitating specific scientific researches such as weather forecasting, studies of global warming, and space weather, and so on.

The troposphere is the lowest layer of the Earth's atmosphere, which extends from the Earth's surface to a height of 9-18 km depending on altitude and weather conditions (Sturman and Tapper, 2006). It contains 99% of water vapor and aerosols. The weather and clouds occur in this layer. The stratosphere extends between 18 and 50 kilometers above the Earth's surface. Air flow in the stratosphere is mostly horizontal. The layer of ozone, a particularly reactive form of oxygen protecting human from ultraviolet radiation, is located within the stratosphere. Above the stratosphere is the mesosphere whose altitude ranges from 50 to 80 km. The temperature drops to about -100 ℃ in this layer, and hence it is the coldest region of the atmosphere. This layer protects the Earth from meteoroids which burn up in this region. The ionosphere (thermosphere) starts at a height about 70-80 km and continues for hundreds of kilometers. It is often assumed that the ionosphere has the average height of 350 km (Xu, 2007). It contains many ions and free electrons (plasma), which are created when sunlight hits atoms and tears off some electrons. The ionosphere layer reflects low frequency radio waves, which makes long-distance radio communication possible.

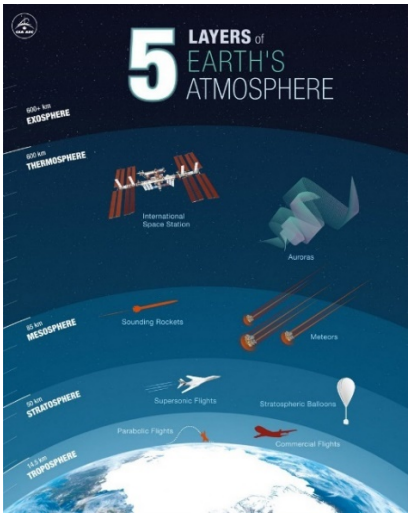

Figure 2.2 Layers of the atmosphere surrounding the Earth (© Canadian Space Agency)

GNSS signals are bent by ionosphere and troposphere when they propagate from satellites to receivers. The first order of ionospheric effect can be eliminated by using ionosphere-free linear combinations of the carrier phases if dual-frequency receivers are used. This is because the ionosphere is a dispersive medium, i.e., the ionospheric delay is frequency-dependent (Xu, 2007; Yan et al., 2014). However, unlike the ionosphere, the troposphere is a non-dispersive medium at the GNSS carrier frequencies (e.g. 1.2 and 1.5 GHz for GPS). In other words, the

tropospheric effects on the GNSS signal propagation are independent from the microwave frequencies of the carrier.

2.2 Sources of Errors in Positioning using GNSS

2.2.1 Space segment errors

Positioning errors due to space segment consist of two types. One is the satellite ephemeris error, and the other is the satellite clock error. Satellite ephemeris errors occur due to inaccuracies in satellite orbit. This orbital error can be decomposed into three components relative to the satellite movement directions, namely radial, along-track and cross-track. The error in the radial direction is small compared to the error in the other two directions. This is favorable for positioning purposes because the influence on the measurement of the apparent range (distance between satellite and receiver) is the largest for the radial component. The Kalman filtering technique is widely used to derive ephemeris parameters (Enge and Misra, 2006). The basic measurement carried out in the GNSS receivers is the transit times of the signals between the satellites and the receiver, which are determined by the difference between the signal transmission time from the satellite and the reception time measured by the receiver (Enge and Misra, 2006). Therefore, the accuracy of the clock is essential. An error of 1μs can cause an offset of about 300 m because the distance between the satellite and the receiver is obtained by multiplying the travel time by the speed of light (Zinas, 2016). To keep the satellite clock error as small as possible, each GNSS satellite carries an atomic clock. The atomic clocks suffer from noise and drifts, and their corrections need to be made. Such clock corrections are necessary in the data analysis and are stored in navigation files made during the measurements (Enge and Misra, 2006).

2.2.2 User segment errors

There are two types of user segment errors. One is the receiver clock error, and the other is the multipath error. Usually, microwaves received in the direct line-of-sight paths are received. However, the signal can also go through several paths, after being reflected by surrounding objects or by the ground before reaching the receiver. Multipath is longer than the direct path and therefore suffers from delays (Enge and Misra, 2006). Multipath signals can be characterized by their amplitude, i.e. its signals are usually weaker than direct signals. When several waves are received simultaneously, an interference occurs. Then, the multipath signals change the phase and amplitudes of the direct path signals to some extent (Yedukondalu, 2011).

2.2.3 Atmospheric errors

Because GNSS signals travel through the atmosphere, they are influenced by the ionosphere and the troposphere. These two layers cause two different kinds of delays. Such delays need to be corrected for accurate positioning purposes.

Ionospheric delays can only be measured by using dual-frequency GNSS receivers. The ionosphere ranges in altitude from ~50 km to over 1000 km above the earth's surface, and large number of free electrons and ions are included there. Ionization is caused by the solar radiation, and free electrons cause refraction of the transmitted satellite signal. Because physical characteristics are governed by the Sun, the difference between day and night is very large. During the day, the molecules are decomposed into positive ions and electrons, and thus the electron density increases. However, when the Sun goes down, such ions and electrons recombine, and the electron density decreases.

The speed of the radio signals depends on the electron density, number of electrons per unit volume, in the propagation medium. Therefore, the total delay reflects a quantity called 'total electron content' (TEC). TEC signifies the total number of electrons integrated along the propagation path and expressed as number of electrons found in a 1 m^2 cross-section column extending from the satellite to the receiver. One way to eliminate ionosphere delays is to use a linear combination of the L1 and L2 phases. The ionospheric group delays at frequency L1 and L2 from code measurements are:

$$I_{L_1} = \frac{f_{L2}^2}{f_{L1}^2 - f_{L2}^2}(\rho L2 - \rho L1) \tag{2.1}$$

$$I_{L_2} = \frac{f_{L1}^2}{f_{L1}^2 - f_{L2}^2}(\rho L2 - \rho L1) \tag{2.2}$$

Where IL1 and IL2 stand for ionospheric delays in the L1 and L2 frequency bands respectively, f_{L1} and f_{L2} stand for the L1 and L2 frequencies, ρL1 and ρL2 stand for code measurements in the L1 and L2 bands, respectively

(Enge and Misra, 2006). Since TEC is large and highly time-variable in the equatorial region, it is essential to determine the ionospheric delays accurately. Better insight into ionospheric variations in the Ugandan region, Africa, is explained by Koning (2016), and a suitable way of determining the ionospheric delay component is explained there.

The tropospheric delay consists of two components: the hydrostatic component, mostly dependent on dry gas, and the wet component coming from the water content in the air. The former component accounts for ~90% of the total delay, but the spatio-temporal variation is far more significant in the latter component. The dry component of the tropospheric zenith total delay (ZTD) is called the Zenith Hydrostatic Delay (ZHD) and is estimated by using models and the accurate pressure measurements at the GNSS station (Gabor, 1997). The wet component of the zenith troposphere is called the Zenith Wet Delay (ZWD). ZWD can be calculated by subtracting ZHD from ZTD; the relationship between the two is as follows (Yedukondalu, 2011).

$$ZTD = ZHD + ZWD \tag{2.3}$$

In this thesis, I tried to learn how to get the ZTD value using the goGPS software. Then I validate the ZTD acquisition process from goGPS, by comparing the ZTD values published from IGS (International GNSS Service) and UNR (University of Nevada, Reno). In the last part of the thesis, I compare the precipitable water vapor (PWV) values from the GNSS stations processed by goGPS, with the PWV values from radiosondes in the same area. In the last part, I analyze ZTD and PWV to study the behavior of ZTD at certain times to explore the possibility of using ZTD information in Indonesia for meteorological purposes.

2.3 Path Delay and Refractivity

2.3.1 Path delay in the atmosphere

The propagation speed v of GNSS signals in the atmosphere can be expressed as

$$v = c/n \tag{2.4}$$

where n is the refractive index and c is the speed of light. Sometimes, it is expressed as $n = c_0 / c$ where c and c_0 are the speed of light in the atmosphere and in the vacuum, respectively. n is a complex number. Its real part relates to the absorption of signals, whereas the imaginary part corresponds to the delay and bending (Hall et al., 1996).

According to the Snell's law, for the neutral horizontally stratified atmosphere,

$$n_i \sin z_i = n_{i+1} \sin z_{i+1} \tag{2.5}$$

where z_i and z_{i+1} are the zenith angles of the arriving radio signal for the layers i and $i+1$. n_i and n_{i+1} are the corresponding refractive indices. Although the refractive index n depends on atmosphere pressure, temperature, and relative humidity conditions, its value is close to unity. This makes the so-called atmospheric refractivity N (in mm/km, or ppm) more convenient to be used instead of n.

$$N = (n - 1) \times 10^6 \tag{2.6}$$

The electro-magnetic (or optical) distance L of a GNSS signal propagating along the path S through the atmosphere will be

$$L = \int c dt = \int c/v \, ds = \int_s n(s) ds \tag{2.7}$$

Let D be the straight-line distance of a GNSS signal in the atmosphere. The atmospheric delay ΔL can be expressed as

$$\begin{aligned} \Delta L &= L - D \\ &= \int_s n(s) ds - D \\ &= \int_s [n(s) - 1] \, ds + \int_s ds - D \\ &= 10^{-6} \int_s N(s) ds + S - D \end{aligned} \tag{2.8}$$

As such, ΔL contains the two factors. Firstly, the traveling speed of GNSS signal in a region of finite density is slower than in a vacuum (Böhm and Schuh, 2013). Such a "slowing" effect appears as the first term of the right-hand side of equation (2.8). The $S - D$ part of equation (2.8) is called the "bending" effect due to the signal bending in response to the gradients in the index of refraction of the atmosphere. The bending effect is approximately 1 cm or less, which is much smaller than the slowing effect. Usually, the bending term is, by convention, considered to be a part of the hydrostatic delay (Kleijer, 2004)

2.3.2 Calculation of refractivity

In the troposphere, the refractivity N can be divided into dry and wet (water vapor) parts according to (Smith and Weintraub, 1953). That is

$$N = N_d + N_v \tag{2.9}$$

Where N_d and N_v are the refractivity of dry air and water vapor, respectively. Equation (2.9) is useful because the contributions of the dry gases can be expressed as a function of pressure, temperature, and humidity (Smith and Weintraub, 1953) for frequencies up to 20 GHz (Thayer, 1974):

$$N_d = \quad k_1 \, Pd/TZ_d^{-1} \tag{2.10}$$

$$N_v = \quad [k_2 \frac{e}{T} + k_3 \frac{e}{T^2} \quad]Z_v^{-1} \tag{2.11}$$

where P_d and e are the partial pressures of dry air and water vapor in Pa (Nm^{-2}). T is the tropospheric temperature. Z_d and Z_v are the compressibility factors of dry air and water vapor, respectively. k_1, k_2, and k_3 are three empirically derived constants.

The compressibility factors in equation (2.10) and (2.11) are given by

$$Z_d = \frac{PM_d}{\rho_d RT} \tag{2.12}$$

and

$$Z_v = \frac{PM_v}{\rho_v RT} \tag{2.13}$$

where P and T are the tropospheric pressure and temperature, respectively. M_d and M_v are the molar mass of dry air (0.028964 kg.mol^{-1}) and water vapor (0.018016 kg.mol^{-1}), respectively. The values ρ_d and ρ_v are the densities of dry air and water vapor, respectively, and R is the gas constant with recommended value 8.3144621±0.0000075 J.K^{-1} .mol^{-1} (Mohr et al., 2012). Obviously, for an ideal gas, the compressibility factor is 1. The inverse compressibility factors can also be given by the empirical formulas. A widely used model using a least-squares fitting to thermodynamic data by Owens (1967) is

$$Z_d^{-1} = 1 + P_d[\ 57.97.10^{-8}\ (1 + \frac{0.52}{T}) - 9.4611.10^{-4}\ \frac{T-273.15}{T^2}] \tag{2.14}$$

$$Z_v^{-1} = 1 + 1650\ \frac{e}{T^3}\ [1 - 0.1317(T - 273.15) + 1.75.10^{-4}(T - 273.15)^2 + 1.44.10^{-6}\ (T - 273.15)^3] \tag{2.15}$$

Moist air contains both dry gases and water vapor. Hence the density of moist air ρ_m is the summation of the dry gas density ρ_d and the water vapor density ρ_v. With equations (2.10) and (2.11), along with the equations of state for dry air and water vapor, equation (2.9) can be expanded as

$$\begin{aligned} N &= k_1 R_d\ \rho_d + k_2 R_v\ \rho_v + k_3\ \frac{e}{T^2}\ Z_v^{-1} \\ &= k_1 R_d\ \rho_m - k_1 R_d\ \rho_v + k_2 R_v\ \rho_v + k_3\ \frac{e}{T^2}\ Z_v^{-1} \\ &= k_1 R_d\ \rho_m + \left(k_2 - k_1 \frac{R_d}{R_v}\right) R_v\ \rho_v + k_3\ \frac{e}{T^2}\ Z_v^{-1} \\ &= k_1 \frac{R}{M_d}\ \rho_m + \left(k_2 - k_1 \frac{M_v}{M_d}\right) \frac{e}{T} Z_v^{-1} + k_3\ \frac{e}{T^2}\ Z_v^{-1} \end{aligned} \tag{2.16}$$

where R_d and R_v are the specific gas constants of dry gases and water vapor, respectively.

$$k'_2 = k_2 - k_1 \frac{M_v}{M_d} \tag{2.17}$$

Then equation (2.16) becomes,

$$N = k_1 \frac{R}{M_d} \rho_m + \left(k'_2 \frac{e}{T} + k_3 \frac{e}{T^2}\right) Z_v^{-1} \tag{2.18}$$

$$= N_h + N_w$$

The first term N_h is called hydrostatic refractivity, which depends only on the density of moist air ρ_m. The second term N_w is non-hydrostatic refractivity, which is also called wet refractivity. N_w is dependent only on the partial pressure e of water vapor and temperature T.

2.4 Retrieval of PWV from GNSS Derived Zenith Delays

2.4.1 Tropospheric delays derived from refractivity

According to Section 2.3, instead of dividing the refractivity into dry and water vapor parts following equations (2.9) – (2.11), one can also divide it into the hydrostatic and the wet parts (Davis et al., 1985) following equation (2.18). It should be noted that in the two cases, dry refractivity N_d and hydrostatic refractivity N_h are not identical, as part of N_h is caused by water vapor. However, this separation of N_h and N_w will not affect but facilitate the calculation of the total refractivity N (Böhm and Schuh, 2013). This is because the hydrostatic refractivity N_h can be simply calculated using surface pressure measurements. Putting equation (2.18) into equation (2.8) gives

$$\Delta L = 10^{-6} \int_S N_h (S) ds + 10^{-6} \int_S N_h (S) ds + S - D = \Delta L_h + \Delta L_w + S - D \tag{2.19}$$

where ΔL_h and ΔL_w are the hydrostatic and wet delays along the path S, respectively. The $S - D$ part is relatively small and usually considered to be part of the hydrostatic delay, as is mentioned in Section 2.3.1.

The atmospheric delay contains the ionospheric part and the tropospheric part. The former can be eliminated using ionosphere-free linear combinations of the phases of the two L-band carrier waves, and the latter contains the hydrostatic and wet delay. In GNSS data processing, it is common that the tropospheric path delay of a signal is mapped from a vertical component using proper mapping functions. Normally, mapping functions are elevation dependent. As such, the corresponding tropospheric path delay becomes

$$\Delta L = z_t \,.\, mf_t \tag{2.20}$$

$$\Delta L_h = z_h \,.\, mf_h \tag{2.21}$$

$$\Delta L_w = z_w \,.\, mf_w \tag{2.22}$$

$$z_t = z_h + z_w \tag{2.23}$$

$$\Delta L = \Delta L_h + \Delta L_w = z_h \,.\, mf_h + z_w \,.\, mf_w \tag{2.24}$$

where

z_t represents ZTD in troposphere,

z_h represents ZHD in troposphere,

z_w represents ZWD in troposphere,

mf_t represents the total mapping function,

mf_h represents the hydrostatic mapping function,

mf_w represents the wet mapping function.

2.4.2 Mapping function

According to the expressions of path delays in equations (2.20) – (2.22), mapping functions are similar to 1/sin (E). However, the determination of the mapping functions, in reality, is far more complicated due to the bending and slowing effects in the atmosphere. The accuracies of mapping functions are vital in high-accuracy positioning applications. This is because zenith delays, station heights, and clocks in GNSS observation equations are highly correlated. Any error in mapping functions will result in corresponding errors in other parameters, especially the station height and the clock offset.

In this research, I used tropospheric delay data from the UNR database (Blewitt et al., 2018). They estimated tropospheric parameters using the GIPSY / OASIS-II Version 6.1.1 software with the Precise Point Positioning (PPP) technique (Zumberge et al., 1997). They follow the 2010 IERS convention (Gérard and Luzum, 2010) and used the Global Mapping Function (Böhm et al., 2006a) and troposphere gradient model of Chen and Herring (1997).

The Global Mapping Function (GMF) model is developed in the Vienna University of Technology (Böhm et al., 2006a). The coefficients of the GMF were obtained from an expansion of the VMF1 parameters into spherical harmonics on a global grid. The implementation of GMF is simple as only the station coordinates, and the day

of the year (DOY) are needed as input. An updated model of GPT/GMF called GPT2 is presented by Lagler et al. (2013). The updates include the usage of more NWP data, refinement of the horizontal and height resolutions, refinement of temperature lapse rate, and extra semi-annual harmonics in order to better explain atmospheres in regions where very rainy periods or very dry periods dominate.

2.5 Model for the Determination of Tropospheric Delays

2.5.1 Zenith Hydrostatic Delay (ZHD)

Integrating the hydrostatic refractivity Nh in vertical direction yields ZHD

$$z_h = \int_{h0}^{\infty} 10^{-6} N\text{h}\,(h)dh \tag{2.25}$$

where h_0 is the station height in meters above the Mean Sea Level (MSL).

Substitution of the first term on the right side of equation (2.18) in equation (2.25) yields

$$z_h = 10^{-6} k_1 \frac{R}{M_d} \int_{h0}^{\infty} \rho_m\,(h)dh \tag{2.26}$$

The hydrostatic equation under the condition of hydrostatic equilibrium is

$$\frac{dP}{dh} = -\rho_m\,(h)g(h) \tag{2.27}$$

where $g\,(h)$ is the acceleration of gravity as a function of height above MSL. $g\,(h)$ can be replaced using a mean gravity g_m (Saastamoinen, 1972).

$$g_m = g_m^0 \,.\, f(\varphi\ h_0) \tag{2.28}$$

where φ is the geodetic latitude and $g_m^0 = 9.748\ \text{ms}^{-2}$·. According to Davis et al. (1985),

$$f(\varphi, h_0) = 1-0.0026\cos 2\varphi - 0.00000028h_0 \tag{2.29}$$

Integrating equation (2.27) yields

$$\int_{P_0}^{0} dP = -\int_{h0}^{\infty} \rho_m(h) g(h) dh = -g_m \int_{h0}^{\infty} \rho_m(h) dh = -P_0 \tag{2.30}$$

where P_0 is the surface air pressure. As such

$$\int_{h0}^{\infty} \rho_m(h) dh = \frac{P_0}{g_m} \tag{2.31}$$

Substituting equation (2.31) into equation (2.26) gives

$$z_h = 10^{-6} k_1 \frac{R}{g_m M_d} P_0 \tag{2.32}$$

Using constant g_m^0 = 9.784 m s^{-2}, given in Davis et al. (1985) and equations (2.28) – (2.29), equation (2.32) can be re-written as (in meters)

$$z_h = 0.0022768 \frac{P_0}{f(\varphi, h_0)} \tag{2.33}$$

So, for any GNSS station with known geodetic latitude and height, its corresponding ZHD can be calculated using equation (2.33) as long as the surface air pressure is given. Surface pressure can also be obtained from empirical models. A widely used pressure model (Kouba, 2009) is as follows.

$$P_0 = 1013.25\ (1 - 0.0000226 h_0)^{5.225} \tag{2.34}$$

Another widely used ZHD model is the UNB (University of New Brunswick) model. It utilizes the Saastamoinen zenith delays (as modified by Davis et al. (1985)) and a look-up table with annual mean and amplitude for temperature, pressure, and relative humidity varying with respect to latitude and propagated to station height (Leandro et al., 2008).

According to previous studies (Davis et al., 1985; Böhm and Schuh, 2013), the main errors in equation (2.33) are as follows:

1) an error of 1 hPa in surface air pressure is likely to cause an error of approximately 2.2768 mm in the resultant ZHD. So, in order to reach an accuracy of 0.1 mm in ZHD, the surface pressure needs to be as accurate as 0.05 hPa. This accuracy level is challenging for most of the empirical pressure models.
2) the coefficient 0.0022768 m hPa^{-1} is calculated using several constants. Its accuracy is 0.0005 m hPa^{-1}, and the error is mainly caused by k_1 (Davis et al., 1985).
3) equation (2.33) is based on the assumption of hydrostatic equilibrium, and the wind may cause an error of 20 mm in ZHD under severe weathers.

2.5.2 Zenith Wet Delay (ZWD)

The value of ZWD is based on wet refractivity. According to equation (2.18),

$$N_{\mathrm{w}} = \left(k'_2 \frac{e}{T} + k_3 \frac{e}{T^2}\right) Z_v^{-1} \tag{2.35}$$

Integrating equation (2.35) along the propagation path yields ZWD z_{w}

$$z_w = 10^{-6}\left[\int_{h0}^{\infty}\left(k'_2 \frac{e}{T} Z_v^{-1}\right)dh + \int_{h0}^{\infty}\left(k_3 \frac{e}{T^2} Z_v^{-1}\right)dh\right] \tag{2.36}$$

Obviously, partial pressure e of water vapor and surface temperature T as functions of height are needed to calculate ZWD. It should be noted that due to the high variability and unpredictability of water vapor, the determination of ZWD is far more challenging than that of ZHD (Böhm and Schuh, 2013). In this study, besides the *a priori* ZHD and ZWD, an additional parameter is set up to account for the residual ZWD. For the calculation of the a *priori* ZWD, Saastamoinen (1972) used an empirical model

$$z_{\mathrm{w}} = 0.0022768(1255 + 0.05T)\ \frac{e}{T} \tag{2.37}$$

585 Other empirical models can be used and found in the literatures (Hopfield, 1969; Askne and Nordius, 1987;
586 Baby et al., 1988; Mendes and Langley, 1999).

587 ZWD is derived from the GNSS processing then converted to PWV by a dimensionless constant of
588 proportionality Π:

589 $$\mathrm{PWV} = z_{\mathrm{w}}\,\Pi \tag{2.38}$$

590 ZWD can be estimated directly from GNSS data processing. It can also be derived when ZHD is subtracted from
591 ZTD.

592 According to Bevis et al. (1994) and Duan et al. (1996),

593 $$\Pi = \frac{10^6\, M_w}{\rho R\,(k_2 - k_1 \frac{M_w}{M_d} + \frac{K_3}{T_m})} \tag{2.39}$$

594 where ρ is the density of liquid water; T_m is weighted mean temperature of troposphere. Values of constants *R,*
595 *k1, k2, k3,* M_{w} M_{d} discussed in Section 2.3.2 are adopted in this study.

596 Errors in Π are mainly caused by errors in T_m and the constants in equation (2.39). Foelsche and Kirchengast
597 (2001) proved that the influence of errors in T_m is at least one order of magnitude larger than the errors introduced
598 by the constants. The accurate calculation of T_m requires the vertical profiles of water vapor and temperature
599 (Davis et al., 1985):

600 $$T_m = \frac{\int(\frac{e}{T})dz}{\int(\frac{e}{T^2})dz} = \frac{\sum_{i=1}^{N}(\frac{e_i}{T_i})_{\Delta z_i}}{\sum_{i=1}^{N}(\frac{e_i}{T_i^2})_{\Delta z_i}} \tag{2.40}$$

601 where both *e* and *T* extend from the surface to the top of the atmosphere. For this real-time retrieval of PWVs,
602 the vertical profiles of water vapor and temperature can become available only by introducing external
603 meteorological data.

604 ### 2.5.3 Zenith Total Delay (ZTD)

605 For the determination of ZTD, there are also several empirical models. Saastamoinen (1972, 1973) proposed a
606 model:

$$z_t = \frac{0.002277}{\sin E}\left[P_0 + \left(\frac{1255}{T} + 0.05\right) e - B\cot^2 E\right] + \delta R \quad (2.41)$$

where E is the elevation angle of the GNSS signal; B and δR are the tabulated functions of station height h_0 and elevation angle E ; R_h is relative humidity (in %). Some other empirical ZTD models can be found in the literature (Hopfield, 1971; Chao, 1974)

2.5.4 Tropospheric delay gradient

The most important part of this research is the tropospheric delay gradient vector ($\boldsymbol{G}$). According to Iwabuchi et al. (2003) and Miyazaki et al. (2013), the vertical components of the position anomaly and ZTD, respectively, differ between the solutions with and without estimation of such gradients. Gradient model improves accuracies in vertical coordinates as well as those in the horizontal plane. There are several tropospheric delay gradient models. Chen and Herring (1997) proposed a gradient model based on the "tilted" atmosphere assumption, which can be expressed as the first term of the gradient mapping function

$$\boldsymbol{G} = (G_N,\ G_E,) \qquad \textit{delay by gradient}\ (\varepsilon,\ \alpha) = m_g(\varepsilon)(G_N \cos\alpha + G_E \sin\alpha) \quad (2.42)$$

where $\boldsymbol{G}$ represents the gradient vector, and G_N and G_E are the north-south and east-west component of the gradient vector, respectively.

$$m_g(\varepsilon) = \frac{1}{\sin\varepsilon \tan\varepsilon + C\prime} \quad (2.43)$$

where C is a constant of 0.0032.

MacMillan (1995) proposed a gradient model similar to the previous one by replacing $m_g(\varepsilon)$ with $m(\varepsilon)$ cotε:

$$\textit{delay by gradient}\ (\varepsilon,\ \alpha) = m(\varepsilon)\ \cot\varepsilon\ (G_N \cos\alpha + G_E \sin\alpha) \quad (2.44)$$

where $m(\varepsilon)$ is the mapping function. Macmillan also indicated that no obvious changes were observed by adopting the hydrostatic or wet mapping function.

Meindl et al. (2004) proposed another gradient model using a zenith angle z between the propagating path of satellite signals and the tropospheric zenith direction (i.e., the direction in which the tropospheric delay is at its

630 minimum) to replace the angle $\check{z}$ between the propagating path of the satellite signals and the geometrical zenith
631 direction to represent the "tilted" atmosphere:

632 $$delay\ by\ gradient\ (\varepsilon,\ \alpha)\ = \frac{\delta f}{\delta z}\ (G_N \cos\alpha + G_E \sin\alpha) \tag{2.45}$$

633 where z is the tropospheric zenith angle and $\frac{\delta f}{\delta z}$ is the derivative of the arbitrary mapping function with respect to
634 the zenith angle z.

635

Chapter 3. GNSS meteorology for disastrous rainfalls in 2017-2019 summer in SW Japan: A new approach utilizing atmospheric delay gradients

The content of this chapter was published in a journal, Frontiers in Earth Science, section Atmospheric Science, a special issue on the “GNSS, and InSAR Meteorology”.

Arief and Heki (2020), GNSS meteorology for disastrous rainfalls in 2017-2019 summer in SW Japan: A new approach utilizing atmospheric delay gradients, *Front. Earth Sci*., **Received:** 26 Jan 2020; **Accepted:** 07 May 2020 | https://doi: 10.3389/feart.2020.00182; **Published:** 23 June 2020

3.1 Introduction

Disastrous heavy rains in summer 2017 - 2019 in SW Japan caused a lot of damage to property and human lives. The Japan Meteorological Agency (JMA) officially named the extreme rainfall event in 2018 July as "The Heavy Rain Event of July 2018". Precipitations records at meteorological stations show extreme rainfall from 28 June to 8 July 2018, especially in the northern part of the Kyushu District. Figure 3.1 shows the precipitation rate in the high-resolution nowcast rainfall map at 17:00 JST (08:00 UT), July 6, 2018, from JMA. This was obtained by a weather radar with a 250 m resolution every 5 minutes. Such meteorological radars have been operated by JMA at 20 stations throughout Japan. The heavy rain occurred over a patchy region elongated in NE-SW and overlap with the stationary front. Water vapor transported along the front from SW is thought to have caused the heavy rain.

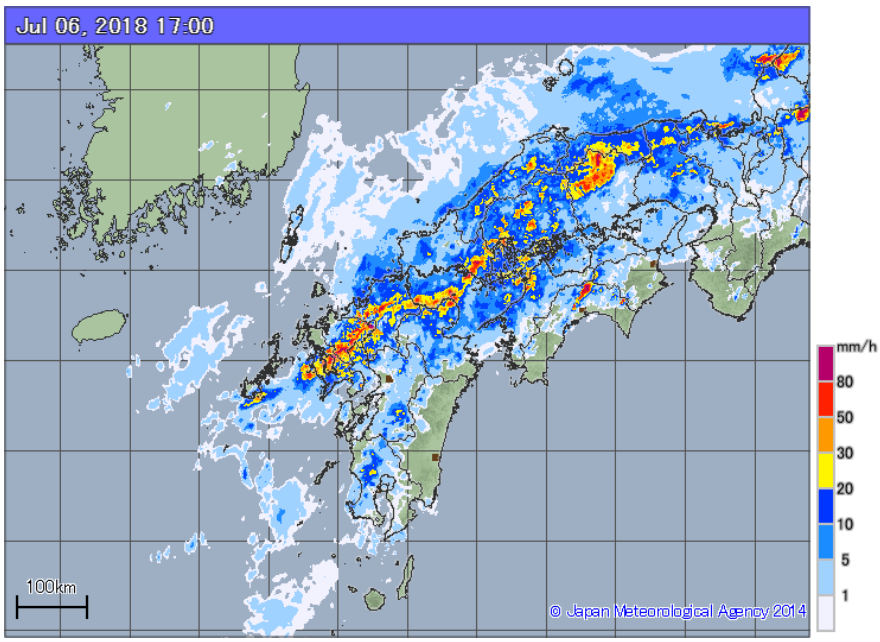

Figure 3.1. High-resolution map of the hourly rainfall at 17:00 JST (08:00 UT) July 6, 2018, from JMA (https://www.data.jma.go.jp/fcd/yoho/meshjirei/jirei01/highresorad/index.html).

The concept of ground-based GNSS meteorology was proposed initially by Bevis et al. (1992), and meteorological utilization of the Japanese GEONET (GNSS Earth Observation Network) has been sought (e.g., Tsuda et al. 1998). Nowadays, GNSS meteorology has become one of the essential means to observe precipitable water vapor (PWV), and PWV data from GEONET have been assimilated in the mesoscale model of JMA to improve weather forecast accuracy since 2009 (e.g., Shoji, 2015). In this study, I apply a new method of GNSS meteorology to utilize atmospheric delay gradients, reflecting azimuthal asymmetry of water vapor (Macmillan, 1995) for the 2017-2019 heavy rain cases in SW Japan.

Miyazaki et al. (2003) focused on such atmospheric delay gradients and showed that the temporal and spatial variations of the gradients were compatible with the humidity fields derived from ZWD and with the meteorological conditions in 1996 summer over the Japanese Islands (especially during a front passages). Shoji (2013) and Brenot et al. (2013) demonstrated the important role of the atmospheric delay gradients to detect small scale structures of the troposphere than ZWD.

Recently, Zus et al. (2019) have successfully processed the Central Europe GNSS network data to show that the interpolation of ZWD observed with a sparse network can be improved by utilizing tropospheric delay gradients. They showed significant accuracy improvement for the simulation of the numerical weather model, and for the agreement of the simulation results with real observations, relative to the cases without utilizing tropospheric delay gradients.

In this study, I propose a new method to use tropospheric delay gradients to study heavy rain phenomena in Japan using the data from the GEONET stations. At first, I analyze behaviors of water vapor on July 6, 2018, using tropospheric parameters obtained from the database published by University of Nevada, Reno (UNR) (Blewitt et al., 2018). The data set includes tropospheric delay gradient vectors (***G***), as well as zenith tropospheric delays (ZTD), estimated every 5 minutes. I interpolate ***G*** to obtain those at grid points and calculated their convergence, similar to the index proposed by Shoji (2013) as water vapor concentration (WVC). Then, taking advantage of the dense GNSS network, I try to reconstruct ZWD in inland regions (especially in high altitude regions) by spatially integrating ***G***.

The purpose of this study is to show the implication of utilizing tropospheric delay gradients, in addition to ZWD, to improve our understanding of water vapor dynamics during heavy rains. For this purpose, I reconstruct ZWD and calculate WVC, and compare them with in-situ rainfall data from AMeDAS (Automated Meteorological Data Acquisition System) stations of JMA. Then I explore behaviors of these quantities common for the three heavy rain cases in SW Japan in summer 2017-2019.

Since its start, the UNR data base published zenith total delay (ZTD) as well as the tropospheric delay gradient vector ***G*** (i.e. no ZWD/PWV). Hence, I removed zenith hydrostatic delays (ZHD) calculated assuming 1 atm atmospheric pressure at sea level and GNSS station altitudes to isolate ZWD. I did not convert ZWD to PWV because the mean atmospheric temperature T_m was unknown. Hence, I used ZWD and ***G*** for reconstructing sea-level ZWDs and water vapor convergence (WVC) indices, as described in this chapter. The paper Arief and Heki (2020) also used ZWD rather than PWV. However, in 2019 autumn, the UNR data base updated their contents and started to provide PWV and T_m in addition to ZTD and ***G***. Hence, it is now easy to replace the sea-level ZWD with the sea-level PWV and to calculate the Laplacian of PWV rather than ZWD in the discussions of this chapter. In this thesis, however, to keep consistency with the paper Arief and Heki (2020), I continue to use ZTD and ***G*** downloaded from the UNR data base.

3.2 Data and methods: Case study for the 2018 heavy rain

I use the data from the dense GNSS network GEONET for the entire country operated by the Geospatial Information Authority (GSI) of Japan (Tsuji and Hatanaka 2018). It consists of more than 1,300 continuously

observing stations deployed throughout the country with a typical separation distance of 15-30 km. Because its official solution (F3 solution) does not include tropospheric parameters in high temporal resolution (Nakagawa et al., 2009), I used tropospheric delay data from the UNR database (Blewitt et al., 2018). They estimated tropospheric parameters using the GIPSY / OASIS-II Version 6.1.1 software with the Precise Point Positioning (PPP) technique (Zumberge et al., 1997) and the products for satellite orbits and clocks from Jet Propulsion Laboratory (JPL). They employ the elevation cut-off angle of 7º and estimate ZTD and the atmospheric delay gradients every 5 min (Vaclavovic and Dousa, 2015). They follow the 2010 IERS convention (Gérard and Luzum, 2010) and used the Global Mapping Function (Böhm et al., 2006a) and troposphere gradient model of Chen and Herring (1997).

3.2.1 ZWD and tropospheric delay gradients

The equation below is formulated by MacMillan (1995) and explains that the slant path delay (SPD) at the elevation angle θ and the azimuth angle ϕ measured clockwise from north can be expressed as follows.

$$\mathrm{SPD}(\theta,\phi) = m(\theta)\cdot[\mathrm{ZTD} + \cot\theta\,(G_\mathrm{n}\cos\phi + G_\mathrm{e}\sin\phi)] + \varepsilon \qquad (3\text{-}1)$$

There, $m(\theta)$ is the isotropic mapping function that shows the ratio of SPD to ZTD, and G_n and G_e are the north and east components, respectively, of the tropospheric delay gradient vectors $\boldsymbol{G}$, and ε is the modeling error. ZTD is the refractivity of the atmosphere integrated in the vertical direction and is the sum of ZHD and ZWD. In this study, I calculated surface pressure at the GNSS stations assuming 1 atm at the sea-level. Then I calculated ZHD and subtracted it from ZTD to isolate ZWD. Considering average variability of surface pressure, errors by this approximation for summer ZWD remains within a few percent (this operation is unnecessary now because of the inclusion of PWV in the UNR new data base since 2019 autumn).

Tropospheric delay gradients are also the sum of hydrostatic and wet contributions. Because I analyze summer data, I assumed that the latter is dominant and used the gradient as those representing the water vapor. Because of the low scale height of water vapor (~2.5 km), ZWD highly depends on the station altitude. That is, small ZWD observed at highland does not always imply low humidity of the troposphere above that station. On the other hand, atmospheric delay gradients are observed by directly comparing atmospheric delays in different azimuths, and little suffer from the station altitude (Shoji, 2013). This is the reason why I use troposphere gradients to reconstruct ZWD converted to sea-level (see Section 3.2.3).

3.2.2 Water Vapor Concentration (WVC)

Shoji (2013) suggested that two new quantities, WVC and WVI (water vapor inhomogeneity) indices, provide valuable information on non-uniform distribution of atmospheric water vapor in meso-β and meso-γ scales. They complement the information from PWV representing water vapor distribution in meso-α scale. WVI is derived from the post-fit phase residuals in the processing of geodetic GNSS data analysis, but such information is not included in the UNR database. In contrast, WVC indices can be derived as the spatial derivative of ZWD. However, as explained in the previous section, low scale height of water vapor makes ZWD highly dependent on station altitudes, and it is difficult to calculate WVC from ZWD in the mountainous Japanese Islands due to large topographic slopes throughout the region. Shoji (2013) suggested that WVC can be calculated directly using the atmospheric delay gradient vector field, which is immune from the height problem and is readily available in the UNR database.

Following Shoji (2013), I study the behavior of WVC to discuss its relationship with heavy rainfalls. WVC index expresses the degree of divergence/convergence of the atmospheric delay gradient and represent the short-wavelength concentration of PWV.

$$\mathrm{WVC} = -\nabla^2 \mathrm{PWV} \tag{3-2}$$

∇PWV is the spatial gradient of PWV. I here use the observed tropospheric gradient $\boldsymbol{G}$, divided by the scale height H of water vapor.

$$\nabla \mathrm{PWV} = \Pi \times \nabla \mathrm{ZWD} = \Pi \times \boldsymbol{G}/H \tag{3-3}$$

Π is the coefficient to convert ZWD to PWV and is a function of atmospheric temperature. ∇ZWD is the spatial gradient of ZWD and can be expressed as $\boldsymbol{G}/H$ (Ruffini et al., 1999). I here assumed 2.5 km for H. In this study, I first obtained the vector $\boldsymbol{G}$ at grid points with east-west separation of 0.20^o and north-south separation of 0.15^o all over the country. Here I calculated $\boldsymbol{G}$ at grid points as the weighted mean of $\boldsymbol{G}$ at all the GEONET stations. Larger weight was given to nearer stations. The weight was taken proportional to the Gaussian function of the inter-station distance with one-sigma of 20 km.

Unlike the original definition of WVC by Shoji (2013), I did not convert the wet delay to PWV by multiplying with Π in (3-3). So, our WVC index is actually $-\nabla^2$ZWD and are calculated numerically as the convergence of $\boldsymbol{G}$, i.e.

$$-\nabla^2 \mathrm{ZWD} = -(\partial G_e/\partial x + \partial G_n/\partial y)/H \tag{3-4}$$

using $\boldsymbol{G}$ at grid values.

Figure 3.2 shows the tropospheric delay gradient vectors at the grid points and its convergence (WVC) calculated by equation (3-4). As the first case study, I investigate water vapor in the heavy rainfall episode at 08 UT (17 JST) July 6, 2018. There are strong southward gradients in southern Hokkaido and central Tohoku, suggesting southwestward increase of water vapor. In northern Kyushu, I can see large gradient vectors line up, suggesting high concentration of water vapor there.

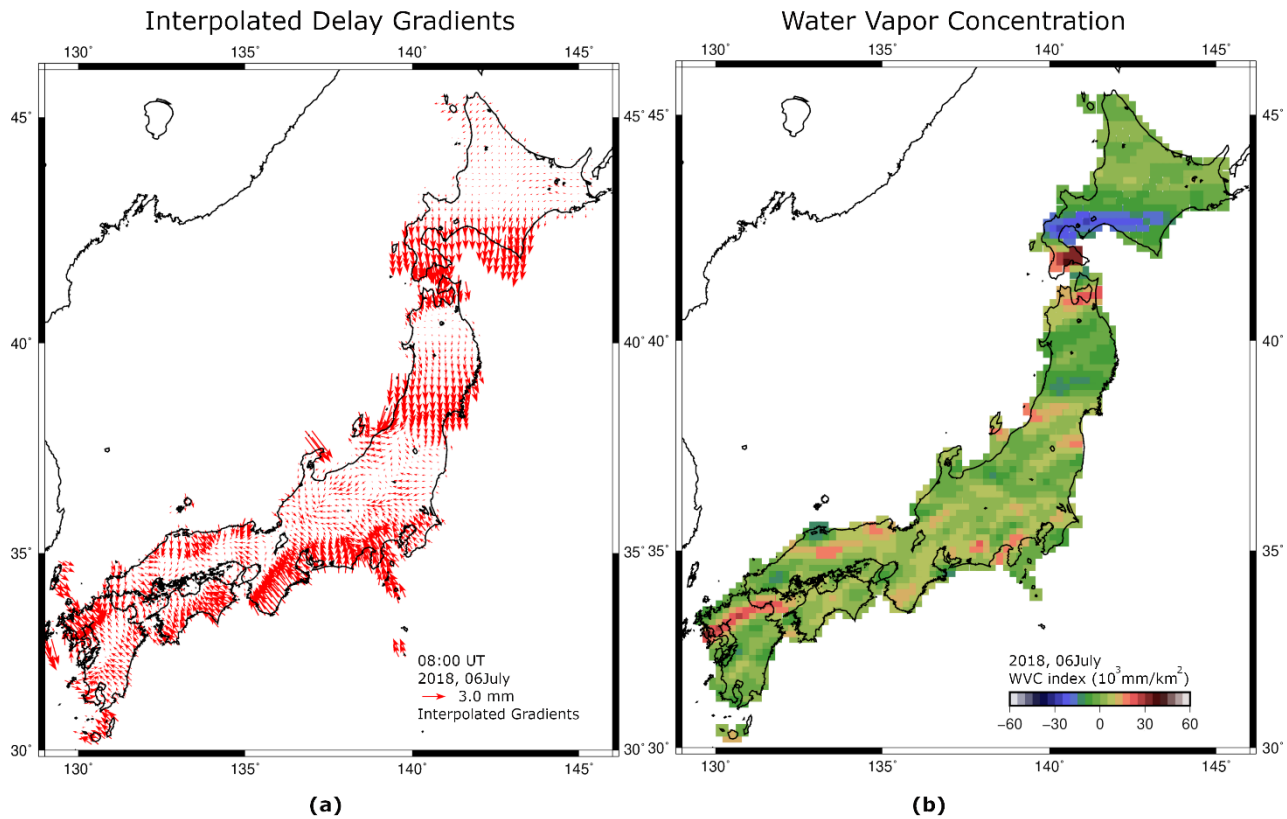

Figure 3.2. (a) Atmospheric delay gradients at grid points at17 JST (08 UT) on July 6, 2018 (raw gradient data are shown in Figure 3.4a). Using these gradient vectors at grid points, I calculated their convergence shown in (b), similar to WVC index defined by Shoji (2013).

3.2.3 Sea-level ZWD

In this study, in addition to WVC, I also reconstruct sea-level ZWD using the observed tropospheric delay gradients and ZWD at low elevation (< 100 m) stations (they are assumed to be identical to sea-level ZWD there). Although the concept of WVC, discussed in the previous section, is adopted from Shoji (2013), it is our original technique to estimate the sea-level ZWD using the gradient vector data as the input.

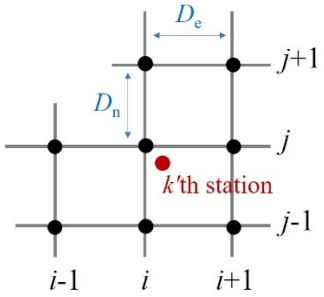

Figure 3.3. Inversion scheme of the sea-level ZWD. I estimate ZWD at grid points, with the east-west separation of D_e (0.20°) and north-south separation of D_n (0.15°), as the parameters, using $\boldsymbol{G}$ at all the stations and ZWD at stations with altitudes lower than 100 m. The observation equation of the ZWD at the central grid (i, j) is given by equation (3-5).

In the inversion, I estimate $x(i, j)$ (i=1,2,…, m_e, j=1,2…,m_n), the sea-level ZWD at the grid point with coordinates (i, j) (i=1,2… m_e, j=1,2,…, m_n). The input data are $\boldsymbol{G}$ (G_n, G_e) at all the GEONET stations. Suppose the situation in Figure 3.3, i.e., the k'th GNSS station, is located within a rectangle made of four corners $(i, j-1)$ $(i+1, j-1)$ (i, j) $(i+1, j)$. Then, the observation equation to relate $\boldsymbol{G}$ at this GNSS station $\boldsymbol{G}(k)$ to the sea-level ZWD at grid points $x(i, j)$ is

$$G_e(k) = \{x(i+1, j) - x(i, j)\} H/D_e \tag{3-5a}$$

$$G_n(k) = \{x(i, j) - x(i, j-1)\} H/D_n. \tag{3-5b}$$

To regularize the inversion, I constrain the sea-level ZWD at the grids closest to the GNSS stations with altitude less than 100 meters to the observed ZWD. They indicate that the sea-level ZWD at the grid point $x(i, j)$ is the same as the ZWD y(k) observed at the k'th GNSS station, i.e.

$$x(i, j) = y(k). \tag{3-6}$$

When I estimate the sea-level ZWD over the entire Japanese Islands, the number of parameters (number of grids) is ~1,600, and the number of observations is twice as large as the number of GNSS stations, i.e. ~2,600. Number of GNSS stations with altitudes < 100 m are ~100. Although we have enough number of data to estimate the parameters, I applied a continuity constraint, i.e. $x(i\pm1, j) = x(i, j)$ and $x(i, j\pm1) = x(i, j)$, to further stabilize the

solution. I constrained the adjacent blocks to have the same values with a tolerance of 50 mm. I also assumed the ZWD measurement errors and gradient observation errors as 10 mm. Because the inversion is not ill-posed, changing the parameters in these constraints little influenced the solution.

In Figures 3.4 and 3.5, I show inputs and outputs of the inversion, respectively. In Figure 3.5b, I confirm that the atmospheric delay gradient vectors at GNSS stations calculated using the estimated distribution of sea-level ZWD. They are similar to the input shown in Figure 3.4a, suggesting that the inversion is successful. The root-mean-square error between the observed and calculated atmospheric delay gradient is ~0.65 mm in this case.

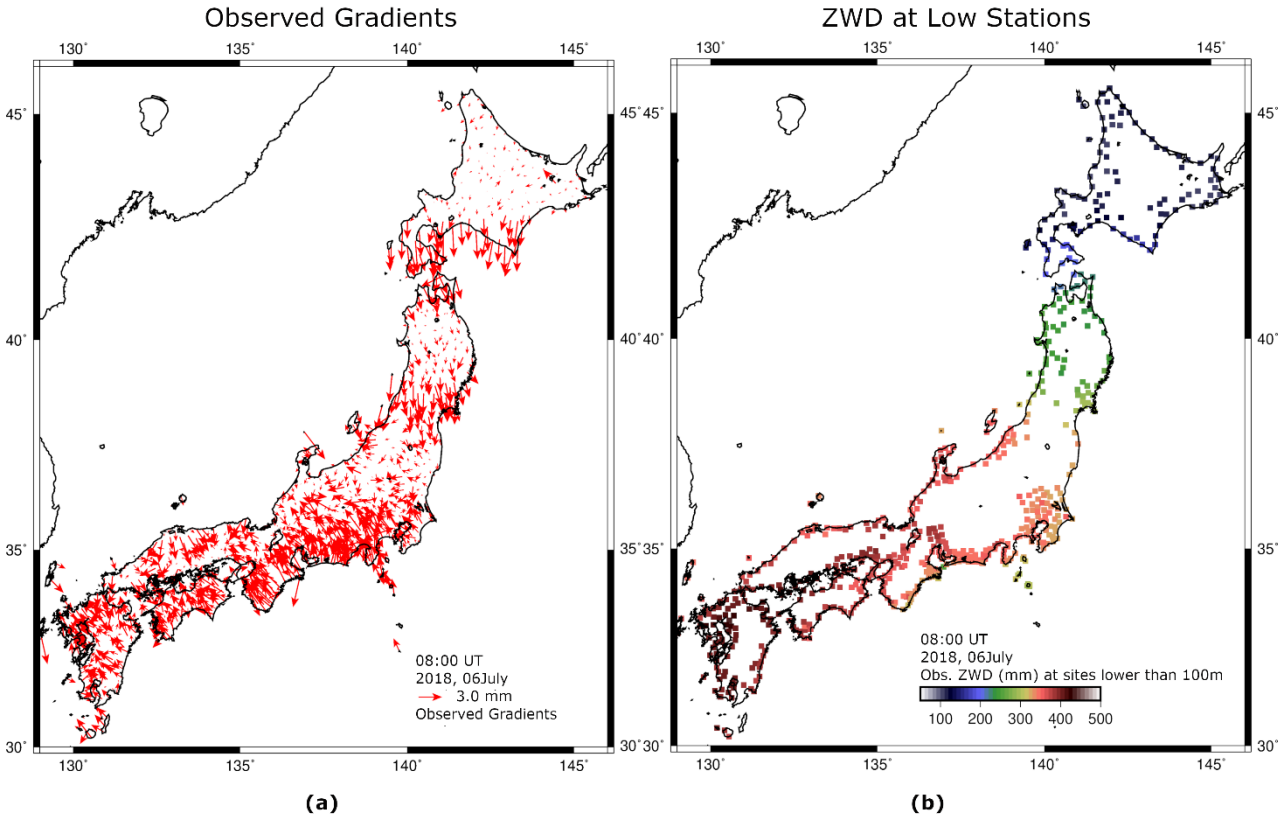

Figure 3.4. Input data for the inversion of sea-level ZWD at 17 JST (08 UT) on July 6, 2018. (a) shows the tropospheric delay gradients at all the GEONET stations, and (b) is the ZWD at stations with elevations <100 m. Using these inputs, I estimated sea-level ZWD at all the grid points shown in Figure 3.5a.

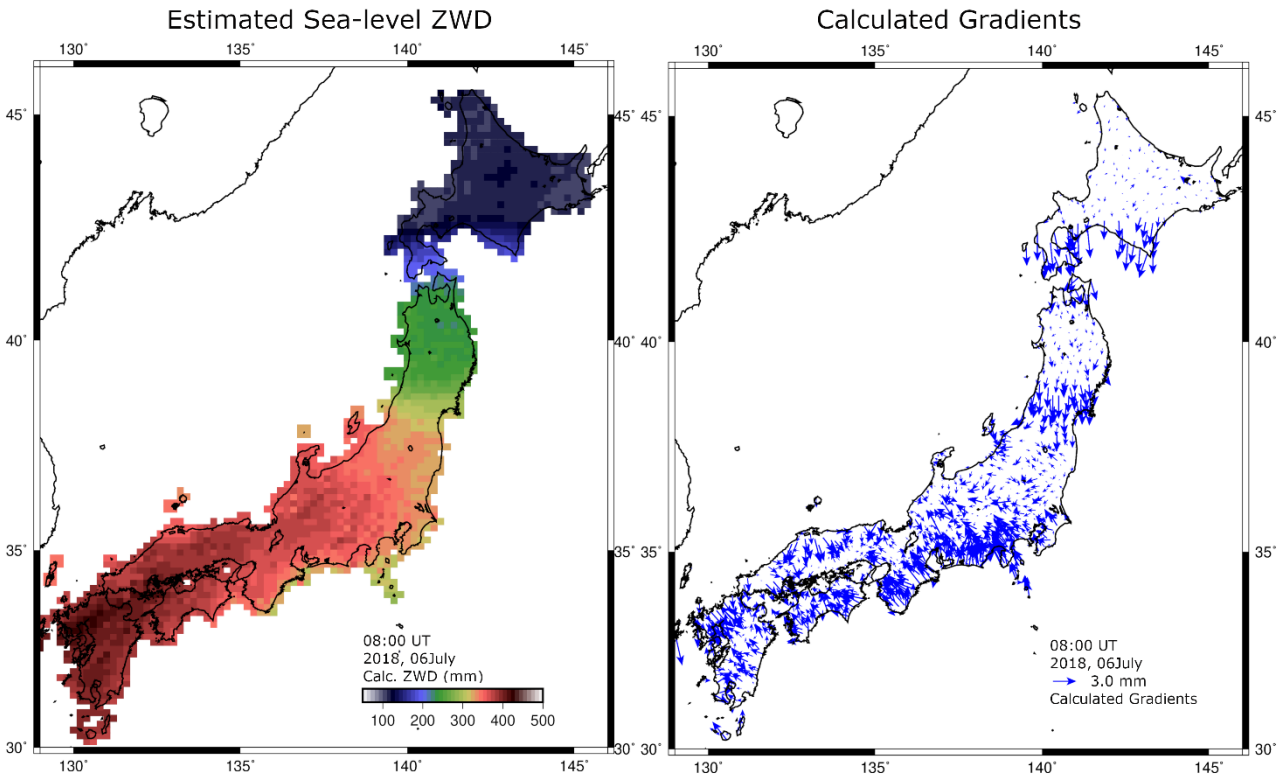

Figure 3.5. (a) Output of the inversion, i.e., sea-level ZWD at grid points at 08 UT (17 LT) on July 6, 2018. (b) shows the atmospheric gradient vectors calculated at GEONET stations using the equation (3.5) and the estimated ZWD, as shown in (a). They are consistent with the observed gradients shown in Figure 3.4a.

3.3 Results and Discussions

Figure 3.5a shows high ZWD throughout SW Japan, but such a ZWD map still lacks spatial resolution to pinpoint heavy rain, as indicated in Figure 3.1. At a glance, WVC in Figure 3.2b shows good coincidence with the heavy rain given in red and orange colors in Figure 3.1. However, there are regions where WVC is high but heavy rain does not occur. This suggests that both two quantities need to be high for the occurrence of heavy rains. In this section, I study long-term and short-term behaviors of the two quantities in several recent heavy rain episodes in SW Japan. For the former, I see hourly changes of WVC and sea-level ZWD over one-month periods, including the heavy rain episodes. For the latter, I study the change of these quantities every 5 minute over the days of heavy rain.

3.3.1 The 2017 and 2019 heavy rain cases

In Figure 3.2b and 3.5b, I show the WVC index and sea-level ZWD at 08.00 UT (17 JST) when heavy rain occurred. This can be compared with the rain images from the JMA, as shown in Figure 3.1. By comparing Figures 3.2b and 1, I can see that the WVC index successfully pinpoints the heavy rain. This is also consistent with the detailed report of this heavy rain episode compiled by JMA (2018).

Here I perform the same calculation for a heavy rain episode on July 5, 2017, at 07 UT (16 JST) and show the results in Figure 3.6. These figures also show, like in the 2018 case, that both the sea-level ZWD and WVC are high where it rains heavily, as shown in JMA (2017). Likewise, Figure 3.7 shows the sea-level ZWD and WVC for a heavy rainfall episode in August 2019. WVC index pinpoints heavy rainfall, consistent with the information released by JMA (2019).

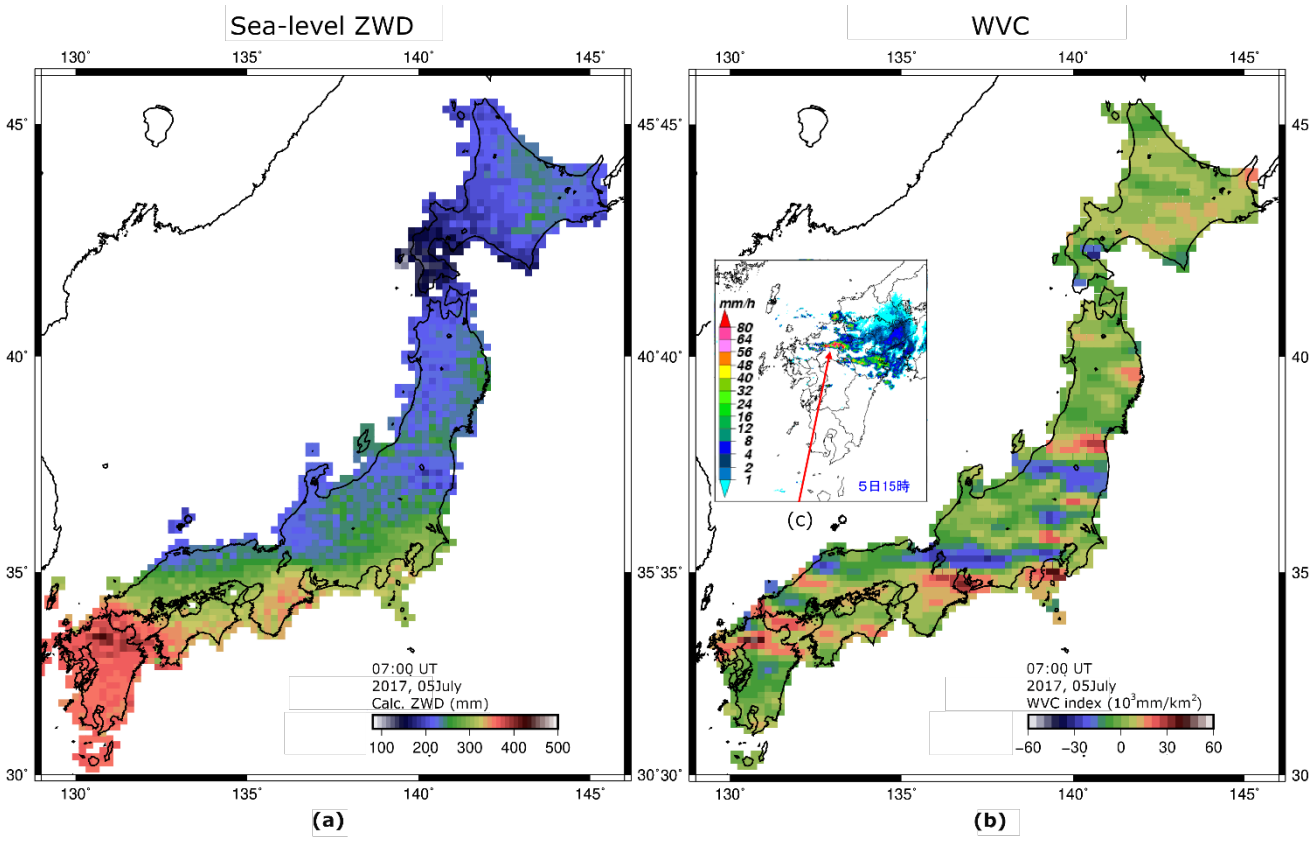

Figure 3.6. Estimated sea-level ZWD (a) and WVC (b) at 07 UT (16 JST) on July 5, 2017. (c) shows the rain rate map from JMA (2017) at the epoch one hour earlier (06 UT) than (a) and (b).

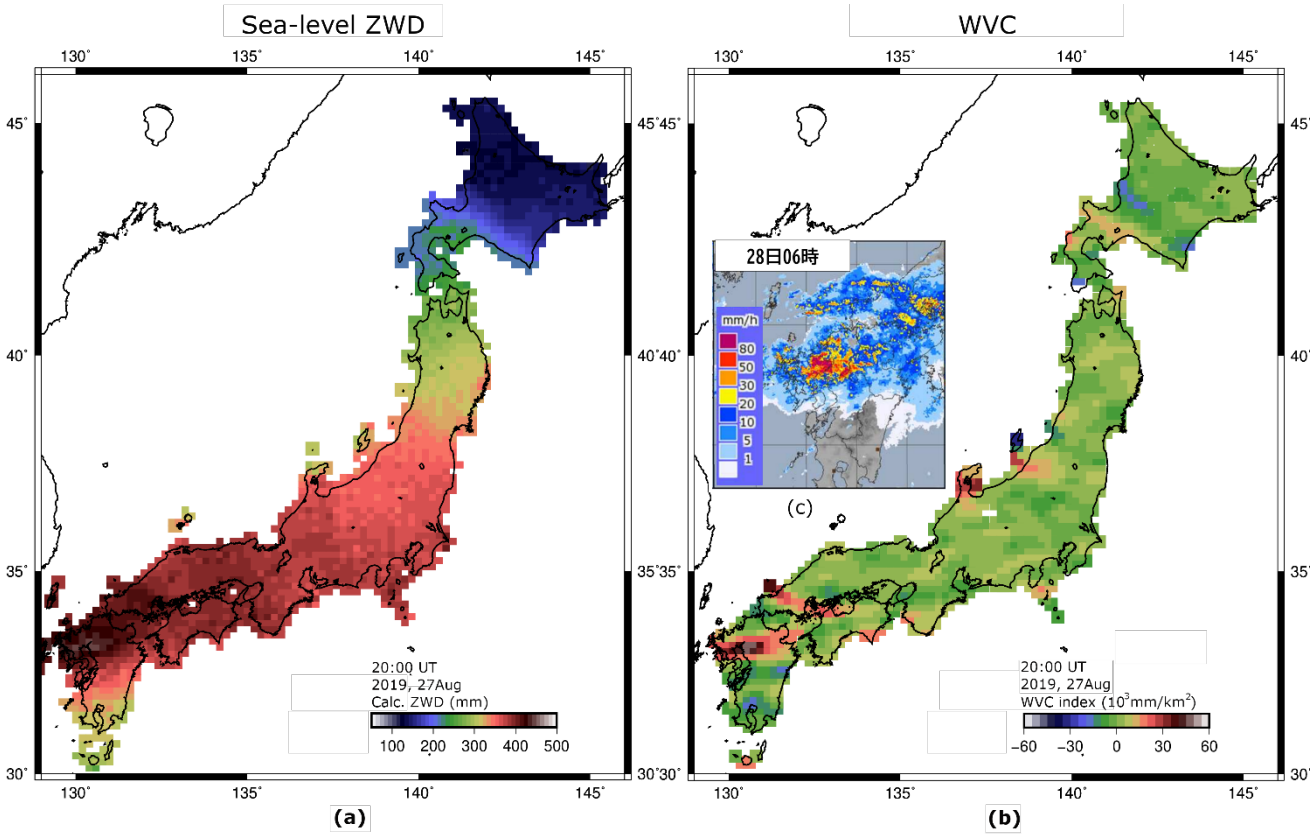

Figure 3.7. Estimated sea-level ZWD (a) and WVC index (b) at 20 UT (05 JST) on August 27 (August 28 in JST), 2019. (c) shows the rain rate map from JMA (2019) at the epoch one hour later (21UT) than (a) and (b).

From these results, I hypothesize that heavy rainfall occurs when both the ZWD and WVC are high. Next, I try to test the hypothesis by studying time series of the two quantities and rain rate.

3.3.2 Validation of the inversion results and the water vapor scale height

Here I try to validate the inversion of nationwide sea-level ZWD (PWV), I show two different kinds of diagrams for the 2017-2019 SW Japan heavy rain cases. The first is the comparison between the observed ZWD (PWV) at all the stations and those calculated with the method described in section 3.2.3. The second is the confirmation of the scale height of the water vapor assumed in the inversion. As explained at the beginning of this chapter, I assumed the water vapor scale height of ~2.5 km, and its validity could be assessed by comparing the discrepancies between the observed and the calculated ZWD (PWV) as a function of station altitudes. Figure 3.8 shows these two kinds of diagrams for the 2017 (a), 2018 (b), and 2019 (c) heavy rain episodes in SW Japan. There, the results are derived by using the new UNR data base including PWV, and the inversions were performed using PWV instead of ZWD.

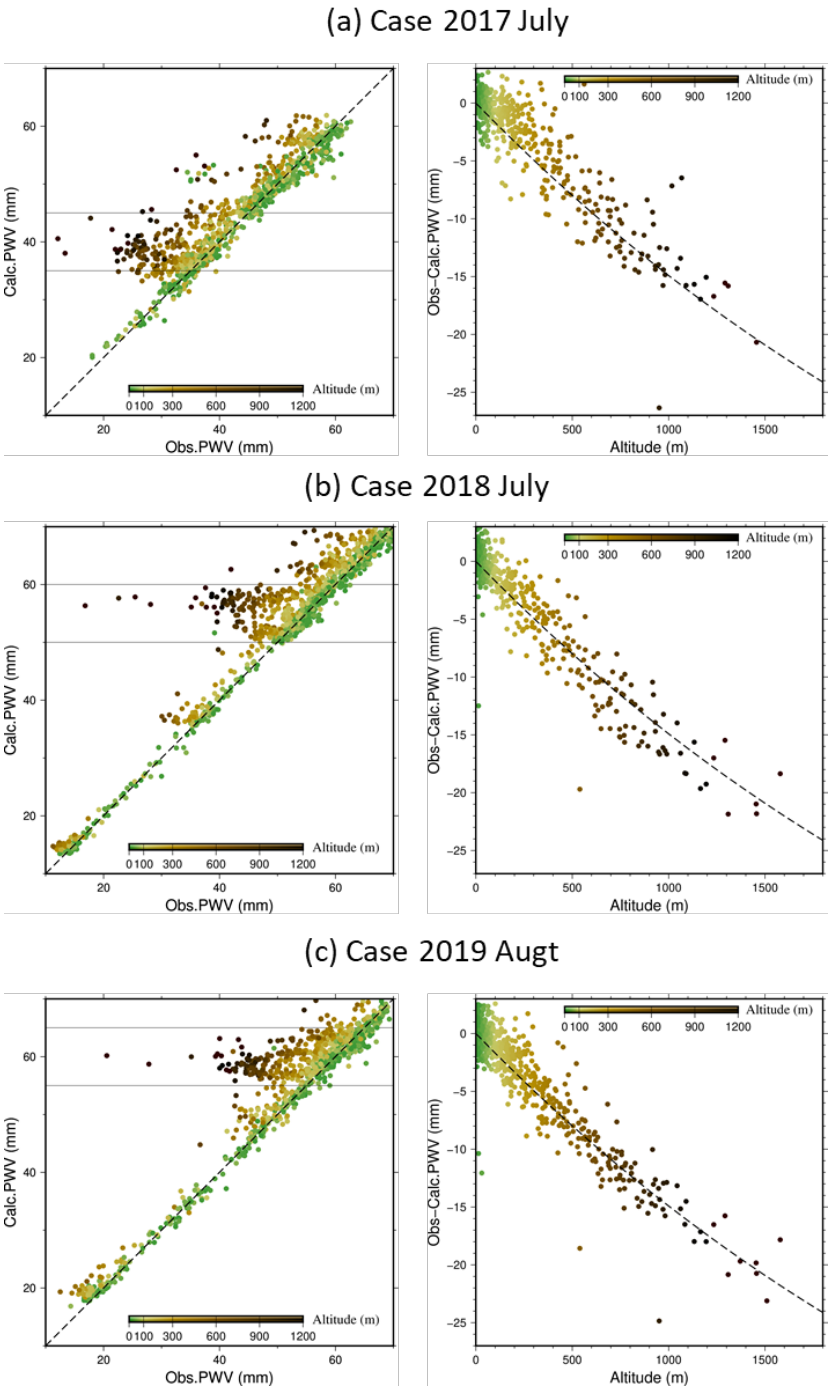

Figure 3.8. The left panels compare the PWV observed by GNSS (horizontal axis) and the PWV calculated by the inversion from the PWV at low-elevation stations and tropospheric delay gradients of all stations (vertical axis). They should coincide for the low-elevation stations if the inversion is successful. However, for high-altitude stations, the observed PWV should be much lower than the calculated zero-level PWV. In the right panels, I plotted the difference between the two (I picked up data with the calculated PWV within the range between the two horizontal lines) as a function of station altitude. The deviation is consistent with the theoretical curve assuming the water vapor scale height of 3.5 km. This is an independent justification of the scale height I assumed in the inversion program.

The Figure 3.8 assumes that the spatial variability of the water vapor scale height is small. Actually, the scale height changes from place to place. The left panels of Figure 3.8 demonstrate that observed and calculated PWV coincide with each other with typical deviation within a few mm for low-altitude stations (shown in green). At

the same time, observed PWV are much lower than the calculated PWV for high-altitude stations. The right panels of Figure 3.8 show the altitude dependences of such deviations. The deviations are seen to align on the theoretical curve $PWV_G = PWV_0 \exp(-H_G/H_{WV})$, where PWV_G and PWV_0 indicate PWV values at the GNSS station and at the sea level and H_G and H_{WV} indicate the station altitude and the water vapor scale height (3.5 km).

Figure 3.8 also means that one can interplate the PWV for any altitude using PWV_0 and PWV_G. One big problem in using the GNSS-PWV for the numerical weather forecast is the deviation of the real GNSS station altitude and the surface altitude in the topography model assumed in the numerical weather model. They assume fairly simple and smooth topography for JMA's numerical weather model (spatial resolution is 15 km and 5 km for the meso-scale and local analyses, respectively), and such models have large discrepancies from the real station altitudes in mountainous area. Currently, JMA uses PWV from GEONET stations whose altitude deviate less than 200 m from the model topography (Y. Shoji, personal communication) and they use simple conversion from PWV_G to PWV values at the modeled altitude. Now, we have two PWV for one GNSS station, i.e. PWV_0 and PWV_G, and a model connecting the two PWV. Then, we can interpolate PWV at the model topography surface altitude and make use of the whole GEONET PWV data in the numerical weather model.

Next, I study the spatial variability of water vapor scale heights by comparing the altitude dependence of the difference between the observed and the calculated PWV as shown in Figure 3.8 in different regions, such as Hokkaido and Kyushu, on the same day. I show the example for the Hokkaido region in Figure 3.9a. There I plotted the data on July 6, 2018, selecting data with sea-level PWV within 5-15 mm. In Figure 3.9b, I compare the data with the theoretical curve based on various values for the scale heights. I tried values ranging from 1 km to 8 km and found that the curve best coincides with the data with the scale height of 8 km, significantly higher than 3.5 km I assumed earlier. I think this anomalously large scale height may not represent the vertical distribution of water vapor. Because I study GNSS data in summer, I naturally assumed that the atmospheric delay gradients reflect the azimuthal asymmetry of the water vapor distribution. However, in the case like Figure 3.9, PWV is quite small and the significant part of the atmospheric delay gradients may originate from the dry air whose scale height is much higher than water vapor.

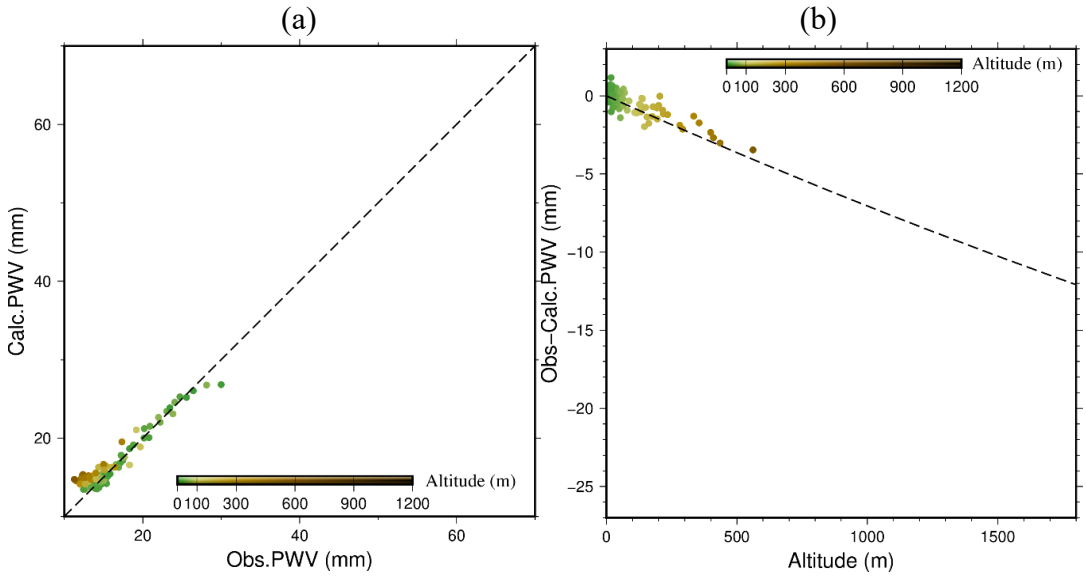

Figure 3.9. (a) compares the PWV observed by GNSS and the estimated sea-level PWV, for the stations in Hokkaido. In (b), I pick up the data with calculated sea-level PWV 5-15 mm and compare the difference between the two as a function of station height. The data best fit the dashed curve based on the scale height of 8 km.

In the Kyushu region, the results of the results are presented in Figure 3.10 (same day as Hokkaido). The sea-level PWV ranges 60-70 mm, which is quite high in comparison with to the Hokkaido region. The scale height that fits the "Obs-Calc" curve is 3.5 km (Figure 3.10b). This is not so different from the nationwide value shown earlier.

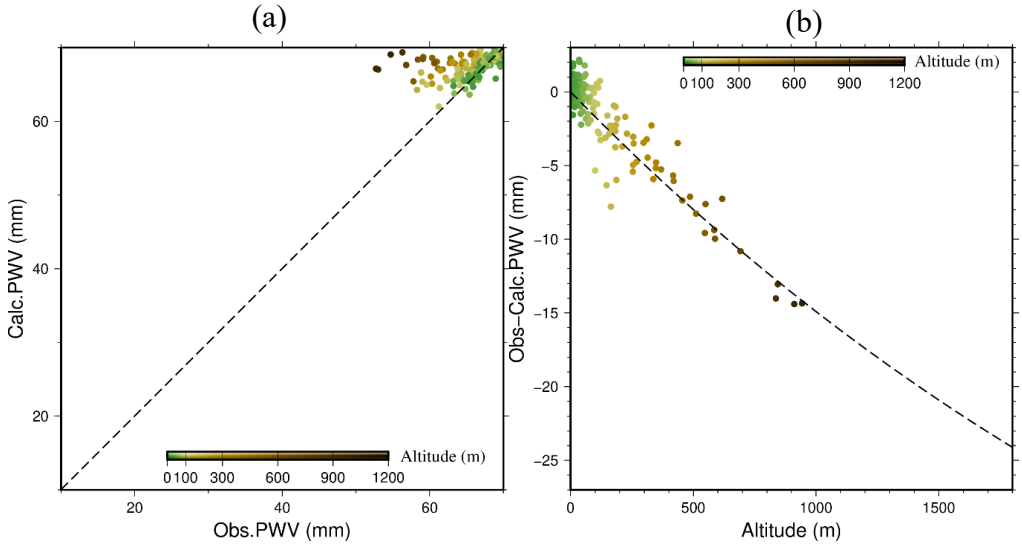

Figure 3.10. (a) compares the PWV observed by GNSS and the estimated sea-level PWV, for the stations in Kyushu. In (b), I pick up the data with calculated sea-level PWV 60-70 mm and compare the difference between the two as a function of station height. The data best fit the dashed curve based on the scale height of 3.5 km.

3.3.3 WVC, sea-level ZWD, and heavy rain

Here I try to justify our working hypothesis that heavy rains occur when the WVC index and sea-level ZWD are both high by analyzing the distribution of water vapor every hour in the three cases, July 2017, July 2018, and August 2019. I present the results in Figure 3.11, which explains the scatter plot of sea-level ZWD and WVC along with hourly rainfall data based on observations at the AMeDAS station of JMA.

I selected the AMeDAS station showing the largest rain for the three episodes, i.e., the Asakura station for 2017, the Yanase station for 2018, and the Shiroishi station for 2019. These three stations are all located in northern Kyushu and recorded heavy rains exceeding 50 mm/hour. Then I picked up the grid point closest to these AMeDAS and compare the three quantities over a month, i.e., 2017 July 2018 July and 2019 August. I can see that ZWD values are high up to 400 mm, and WVC index goes up to 40 x 10^3 mm/km^2 when heavy rain exceeding 50 mm/hour occurred on July 5, 2017, July 6, 2018, and August 27, 2019 (Figure 3.11).

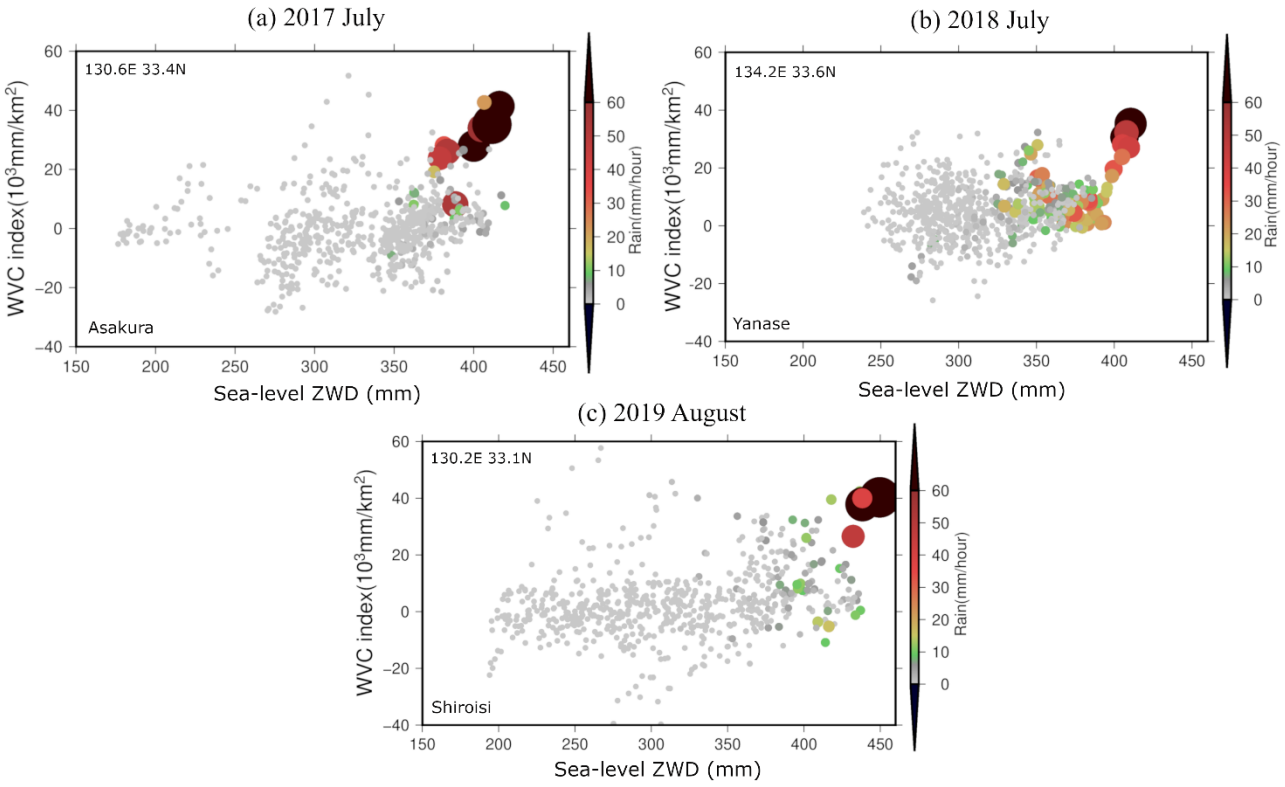

Figure 3.11. Distribution of hourly values of WVC (vertical axis), sea-level ZWD (horizontal axis), and hourly rain rate (color and circle size) for 2017 July (a), 2018 July (b), and 2019 August (c). The rain rate was measured at the Asakura, Yanase, and Shiroishi AMeDAS stations, respectively, and WVC and ZWD are the values at their nearest grid points. (coordinates given at the upper left corner)

Next, I look for data from more AMeDAS stations in Japan on the same days showing hourly rain rates exceeding 50 mm/hour and found 12 stations for the 2018 July and 5 stations for the 2019 August, the months including heavy rain episodes. The 2017 heavy rain was quite local (limited to northern Kyushu), I could not find enough number of AMeDAS stations showing rains exceeding 50 mm/hour. From Figure 3.12a, I find that the probability

of the heavy rain (> 50 mm/hour) was 14 % for the range of ZWD (400-450 mm) and WVC index (35-50 x 10^3 mm/km^2), for the month July 2018. Likewise, for the month August 2019, the heavy rain occurred 50 % for the same range of ZWD and WVC index. If I count rains exceeding 20 mm/hour, then the percentages go up to 71% for July 2018, and 78% for August 2019. These results indicate that both the WVC index and sea- level ZWD are high when heavy rains occur. The results also suggest that heavy rains may not occur even when these two quantities are high. Next, I will show time series of these quantities.

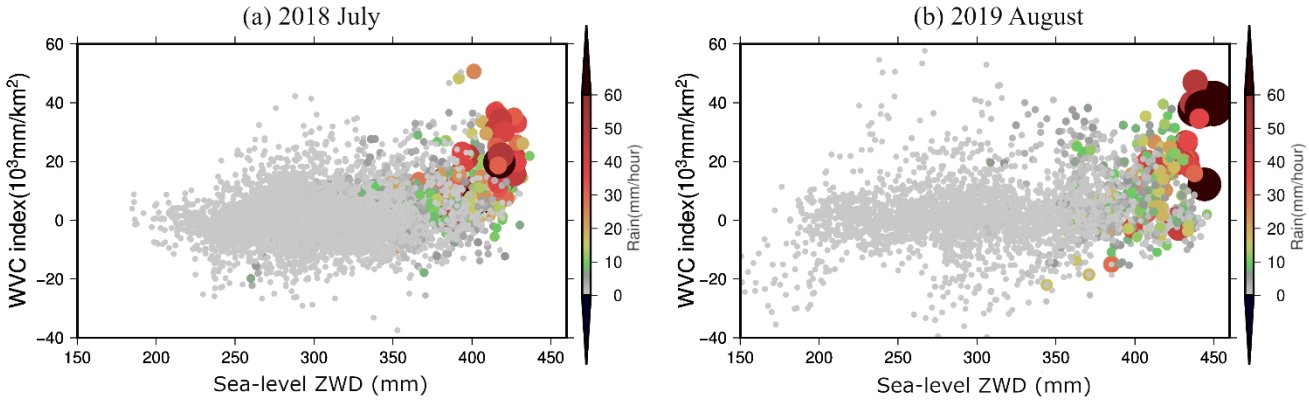

Figure 3.12. Same as Figure 3.11b, c, but I stacked data for 12 and 5 AMeDAS stations showing hourly rain rate exceeding 50 mm in 2018 July (a) and 2019 August (b), respectively. Again, I compare hourly rain rates with the WVC and ZWD, calculated at the nearest grid points of the AMeDAS stations.

3.3.4 Time series analysis

In Figure 3.13, I plot the quantities in Figure 3.11 as the function of time. The two quantities WVC and sea-level ZWD, are given at the top while the rain rate is given at the bottom. The bottom panels also include the time series labeled as “Deviation.” This quantity indicates the sum of the deviations of WVC and sea-level ZWD from their averages normalized by their standard deviations. For example, if both quantities deviate from the means by 2σ, the “Deviation” is 4.

Figure 3.13 clearly shows that the two quantities show large deviations from the average values whenever heavy rains occur. I also see sometimes that high “Deviation” does not coincide with a heavy rain, e.g., 2017 July 20 and 2018 July 23. Regarding the time sequence, the high WVC / ZWD times seem to "coincide" with heavy rains rather than "precede" them, and the usefulness of monitoring these quantities for weather forecast is not clear from this figure.

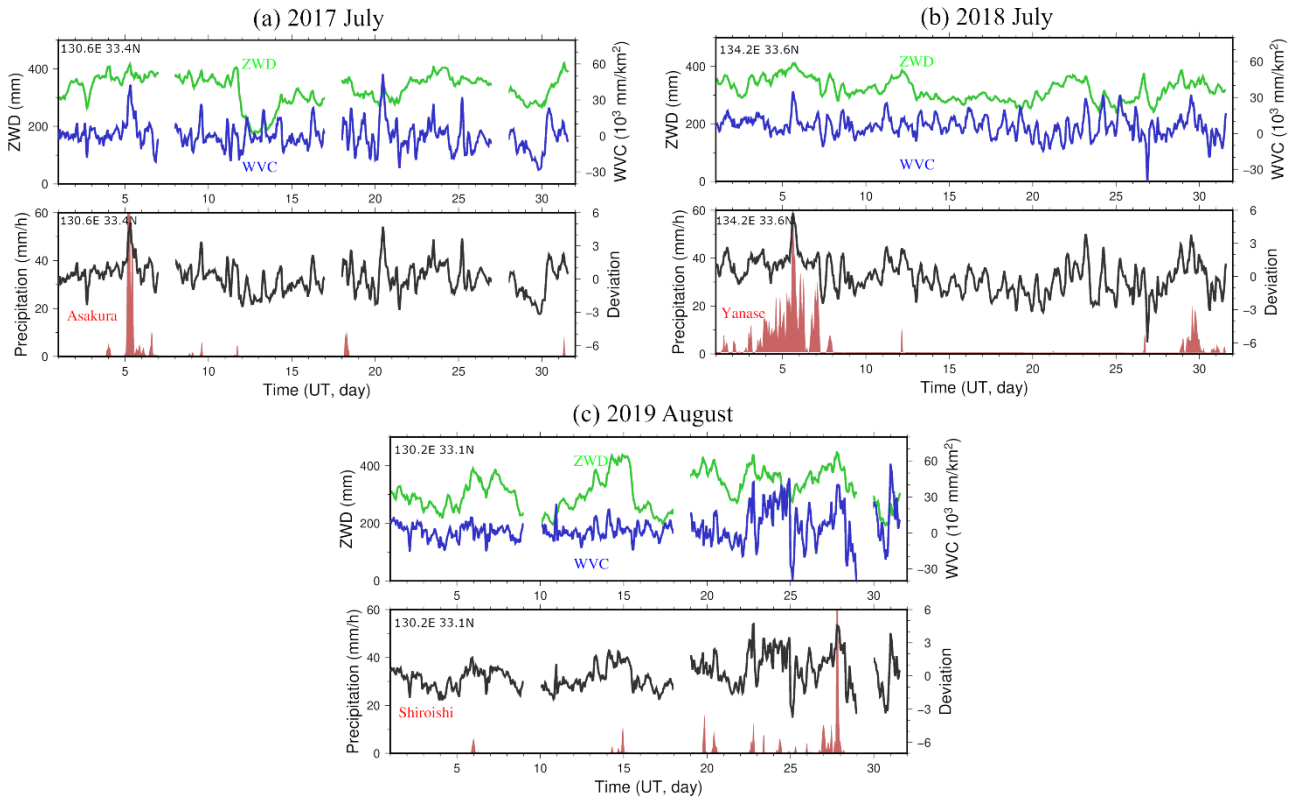

Figure 3.13. Time series of the two quantities shown in Figure 3.11, WVC and sea level ZWD (blue and green in the top panels), and rain rate at the nearest AMeDAS stations (red in the bottom panels). The bottom panels also show a new quantity (labeled as "Deviation") in black, the sum of the standard deviation of the two quantities. They are for 2017 July (a), 2018 July (b), and 2019 August (c). High hourly rain rates occur when both the WVC and ZWD record very high values.

Lastly, I analyzed high time resolution (every 5 minutes) behaviors of WVC, ZWD, and rain rate, for the three heavy rain days in 2017/7/5, 2018/7/6, and 2019/8/27, selecting two AMeDAS stations from each episode (Figure 3.14). I estimated the sea-level ZWD and WVC every 5 minutes for these three days. The results show that both WVC indices and sea-level ZWD show large values at the start of the heavy rains. However, for many cases (e.g., Fig. 3.12a, e, f), heavy rains already started before the two quantities reach their peaks, suggesting limited applicability of these quantities for weather forecast. ZWD often showed rapid declines after the starts of the heavy rainfalls, possibly because of the transformation of water vapor to liquid water.

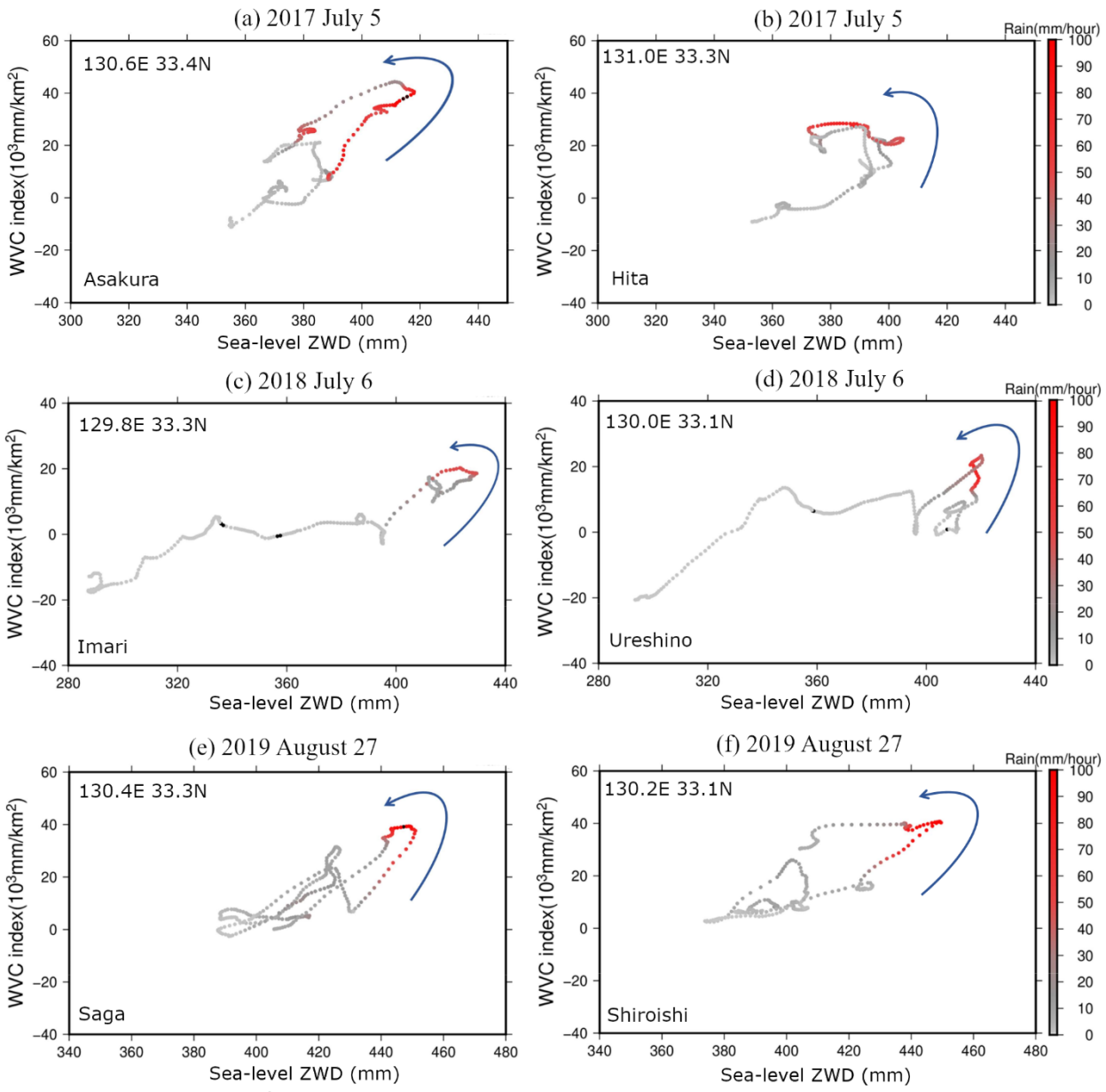

958

959 **Figure 3.14**. High time resolution (5 minutes resolution) behaviors of rain rate in the sea-level ZWD-WVC
960 space during the heavy rain days, 2017 Jul. 5 (a: Asakura, b:Hita), 2018 Jul. 6 (c: Imari, d: Ureshino), and
961 2019 Aug. 27 (e: Saga, f: Shiroishi). The color indicates hourly precipitation of AMeDAS stations
962 interpolated to match the time resolution of sea-level ZWD and WVC.

Chapter 4. Crustal subsidence by water load with a dense GNSS network: A case study of the July 2018 heavy rainfall in SW Japan

4.1 Introduction

Disastrous heavy rains in summer 2018 in SW Japan caused a lot of damage to property and human lives. The Japan Meteorological Agency (JMA) officially named the extreme rainfall event in 2018 July as "The Heavy Rain Event of July 2018". Precipitation records at meteorological stations show extreme rainfalls from 28 June to 8 July 2018, especially in the northern part of the Kyushu District. The heavy rain occurred over a patchy region elongated in NE-SW and overlap with the stationary front. Water vapor transported along the front from southwest is thought to have caused the heavy rain. Figure 4.1 shows the report by JMA of the distribution of cumulative rainfall from 28 June to 8 July 2018.

GNSS is a system that is operated to study deformation of the earth's crust. In Japan, continuous observation stations are installed at more than 1,300 points all over the country and operated by Geospatial Information Authority of Japan (GSI) as GNSS Earth Observation Network (GEONET). So far, application of GNSS for meteorological purposes has been limited to the measurement of water vapor or GNSS meteorology. The concept of ground based GNSS meteorology was proposed initially by Bevis et al. (1992), and meteorological utilization of the Japanese GEONET has been sought (e.g., Tsuda et al., 1998). Nowadays, GNSS meteorology has become one of the essential means to observe precipitable water vapor (PWV), and PWV data from GEONET have been assimilated in the mesoscale model of JMA to improve weather forecast accuracy since 2009 (e.g., Shoji, 2015). Arief and Heki (2020) applied a new method of GNSS meteorology to utilize atmospheric delay gradients, reflecting azimuthal asymmetry of water vapor (Macmillan, 1995), for the 2017-2019 heavy rain cases in SW Japan. These topics have been explained in detail in the previous chapter of the thesis.

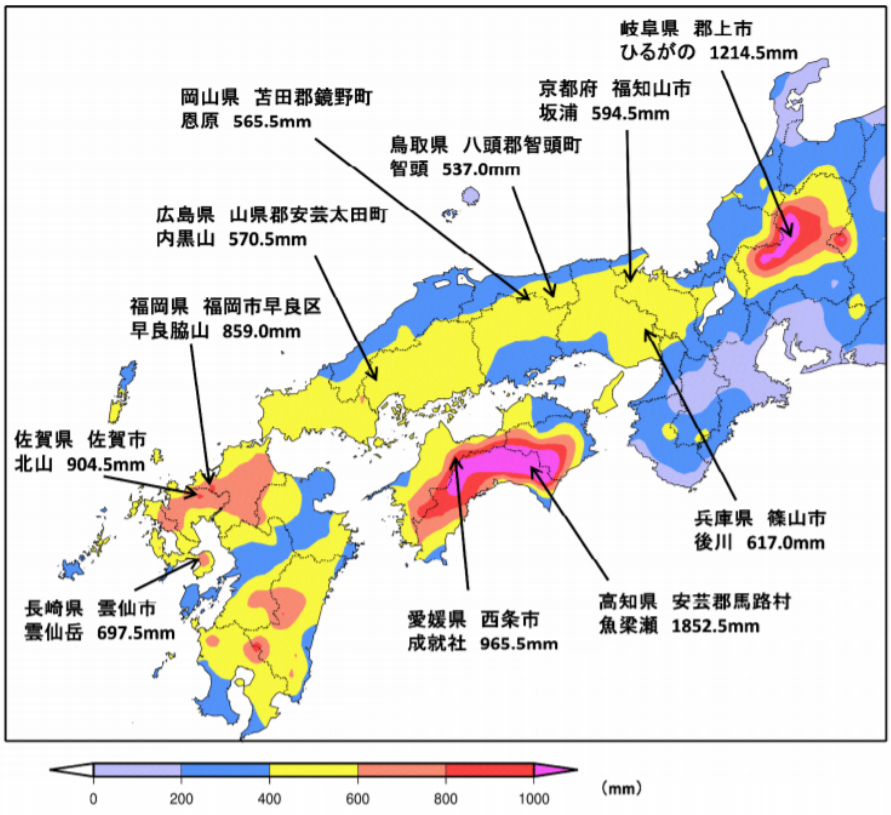

Figure 4.1. Distribution of areas that suffered from disastrous heavy rains from 28 June to 8 July 2018, along with the value of cumulative rainfall, based on reports from JMA (http://www.data.jma.go.jp/obd/stats/data/bosai/report/2018/20180713/jyun_sokuji20180628-0708.pdf: page 17)

Here I focus on another way of using dense GNSS receivers to study meteorological events, i.e., crustal deformation caused by water load. Researches on the changes of hydrological loads such as snowpack and glaciers have been carried out using time-variable gravity observations with GRACE (Gravity Recovery and Climate Experiment) satellite systems. GNSS can also be used to study such loads. For example, in Japan, a maximum subsidence of 1 to 2 cm can occur in winter, especially on the Sea of Japan side due to increased loads such as snow (Heki, 2001). In Japan, other loads such as atmosphere, non-tidal ocean load, reservoirs are considered to contribute to the seasonal crustal movement of GNSS stations (Heki, 2004). However, crustal movements to transient meteorological phenomena such as heavy rains have never studied before.

Heavy rain, which causes flooding acts as a surface load and presses the crust to the detected level. In North America, Milliner et al. (2018) conducted research on vertical crustal deformation due to rainfall due to a tropical cyclone (hurricane Hurvey) that made landfall on United States using GNSS receivers around the coast of the Gulf of Mexico. Here I try to analyze the link between crustal movements and a heavy rain episode as a carrier of water from ocean to land in the early July 2018 disastrous heavy rains occurred in SW Japan.

4.2 Data and Methods

I use the F3 solution (Nakagawa et al., 2009), which is the official solution from the Geospatial Information Authority of Japan (GSI). This solution is derived using the Bernese software and ITRF (International Terrestrial Reference Frame) 2005. This solution is used for analysis of crust deformation in Japan. Analysis of the F3 solution is carried out in two stages: estimation of the reference station, Tsukuba, in ITRF, and the static positioning of other stations relative to Tsukuba. In the first stage, the coordinates of the Tsukuba station are determined in the ITRF 2005 with respect to several stations in the Asia-Pacific region around the Japanese islands. Then, they estimate the position of other GEONET stations relative to the Tsukuba reference station. They estimate atmospheric zenith delays every three hours but estimate only one atmospheric delay gradient vector per day. In this chapter, I do not use the UNR solution.

Generally speaking, deformation due to the surface load makes about three times as large displacements in the vertical component than in horizontal components. At the same time, the vertical component suffers from a larger positioning errors than the horizontal components. This time, I used the vertical components to capture crustal signatures of surface loads. Another benefit of the vertical is that the azimuth of the horizontal displacement strongly depends on the distribution of the load, while vertical displacement is less sensitive to such distribution.

In the next section, I explain the way to reduce systematic noises in the displacement signals by removing common mode errors in the daily F3 GNSS solution data. I followed the method of Heki (2020), i.e., I removed common mode errors by performing the Helmert transformation for the station coordinates so that positions of the selected ~100 stations coincide with their median positions over periods ranging ± 15 days around the heavy rainy days.

4.2.1 Correction of common mode errors

The raw time series of the F3 solution often show outliers which deviate largely from the rest of the coordinate time series. Such deviations often occur uniformly all over the country, suggesting the error in the fixed reference point (the Tsukuba station). In the analysis of crustal subsidence using the F3 solution, I made such correction to remove the common mode errors from the F3 solution.

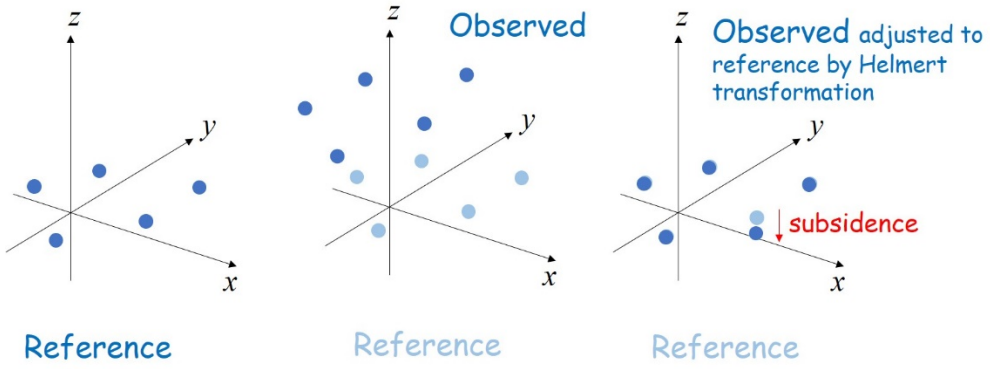

Figure 4.2. Concept of the Helmert transformation of a certain set of stations to the reference positions. I performed this adjustment of daily GEONET coordinates to the reference position defined as the median of a certain period of time.

I used the Helmert transformation to remove such common errors. The Helmert transformation consists of 7 parameters, translation (3 components), rotation (3 components), and scale change (Figure 4.2). This time, I first selected ~100 stations from the GEONET stations constructed in 1994 because they are uniformly distributed in the country (station 940001 to 940099, except a few obsolete stations). I then calculated the median of the coordinate values for these stations over a time period of about a month centered on the heavy rainfall day. There I assumed that there are no crustal movement of tectonic origin during that period. Then the seven transformation parameters were estimated for each of the days by the least-squares method so that the individual daily coordinates would match the median positions as much as possible. All daily GEONET data were transformed using these seven parameters.

4.2.2 Analysis of station position change for one month

In Figure 4.3, I illustrate the basic concept of vertical crustal movement due to heavy rainfall. Immediately after the heavy rain, water will remain on the surface and would exert downward force. It will cause crustal subsidence, as shown in Figure 4.3b. For this process, I can use the Green's function to calculate crustal movements due to known surface loads. After rain, surface water would move downward to recharge groundwater. This process may cause uplift of the surface (Figure 4.3c), but it is not straightforward to calculate the displacement because it is difficult to know the amount of groundwater and physical process of crustal inflation due to water.

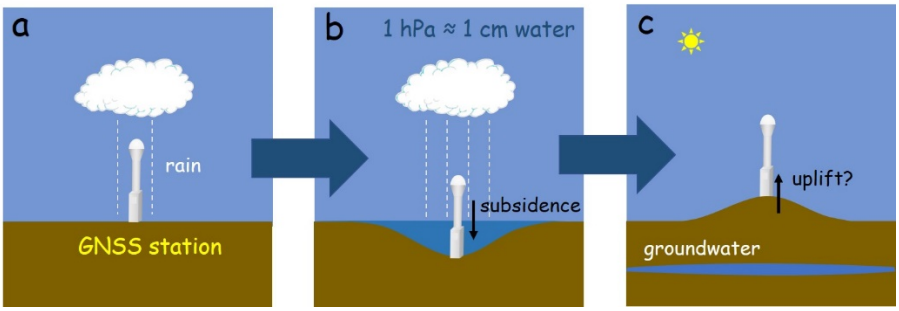

Figure 4.3. Subsidence of GNSS stations due to the surface load caused by rainwater (a). Surface water with 1 cm thickness exerts about 1 hPa downward pressure and depresses the ground (b). Uplift may occur when surface water goes down to become groundwater (c).

Figure 4.4 shows the vertical coordinate time series of six GNSS stations in northern Kyushu over a month, including the heavy rain episode in 2018 July after common-mode error removals. I expect that the GNSS stations subsided due to water load in the area of the heavy rain. As seen in Figure 4.4, on heavy rainy day (July 5), the stations in Kyushu show subsidence of 1-2 cm.

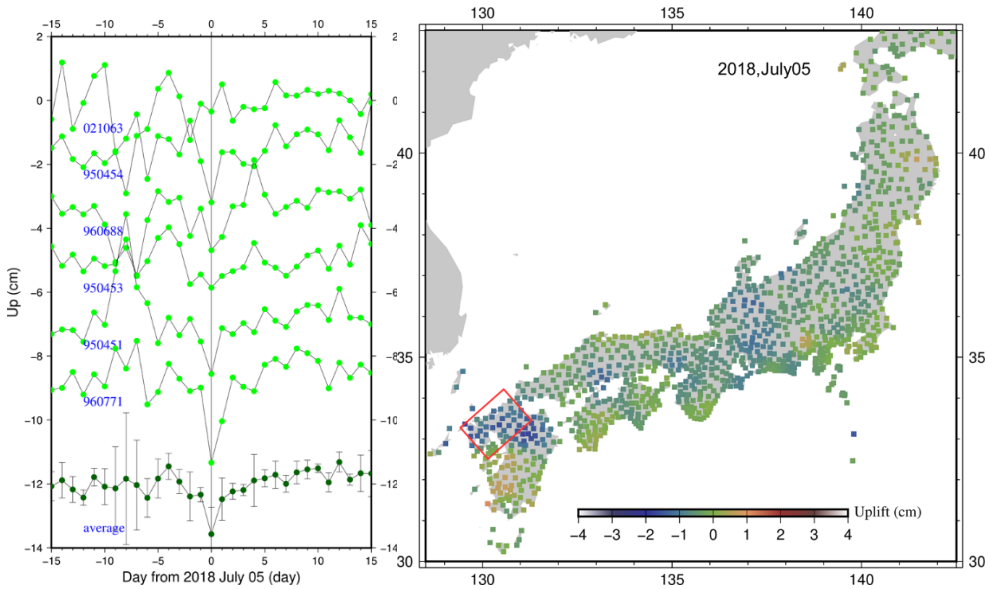

Figure 4.4. (a) Time series of vertical positions of six stations in northern Kyushu before and after the 2018 July heavy rain. They are relative to the median position during this period. The bottom time series are derived as the average of these six stations. These stations show subsidence on the day of the heavy rain, July 6, 2018. (b) Map of vertical displacements relative to the 1-month median positions of all GEONET stations on July 6, 2018. Stations in (a) are taken from the region within the red rectangle and spatially smoothed with averaging radius of 20 km.

The vertical component suffers from larger noise than the horizontal components. In Figure 4.4b, I applied spatial averaging to reduce noise. There, the smoothing is done by calculating weighted averages of all the data, and the weights were determined by putting the distances from the point into the Gaussian function. The standard deviation σ is a measure indicating the averaging radius used for the spatial smoothing, and I set its value as 20 km in this study.

Based on the flood map from JMA (Japan Meteorological Agency) shown in Figure 4.1, I selected 7 regions affected by floods, the prefectures Saga, Fukuoka, Oita, Hiroshima, Hyogo, Toyama, and Gifu, from west to east, and I plot average time series of vertical positions of 5 stations selected from each region in Figure 4.5.

In addition to the amount of maximum subsidence, I can see phase lags of the subsidence coming from the time lag of strong precipitation, i.e., the largest subsidence occurs later in more easterly regions For example, in the Hyogo area, the red circle in Figure 4.5a shows the lowest subsidence value occurred on July 6, 2018, the next day of the precipitation maximum in Kyushu. In the Oita and Toyama areas, the blue circle in Figure 5a, large subsidence seems to occur over multiple days.

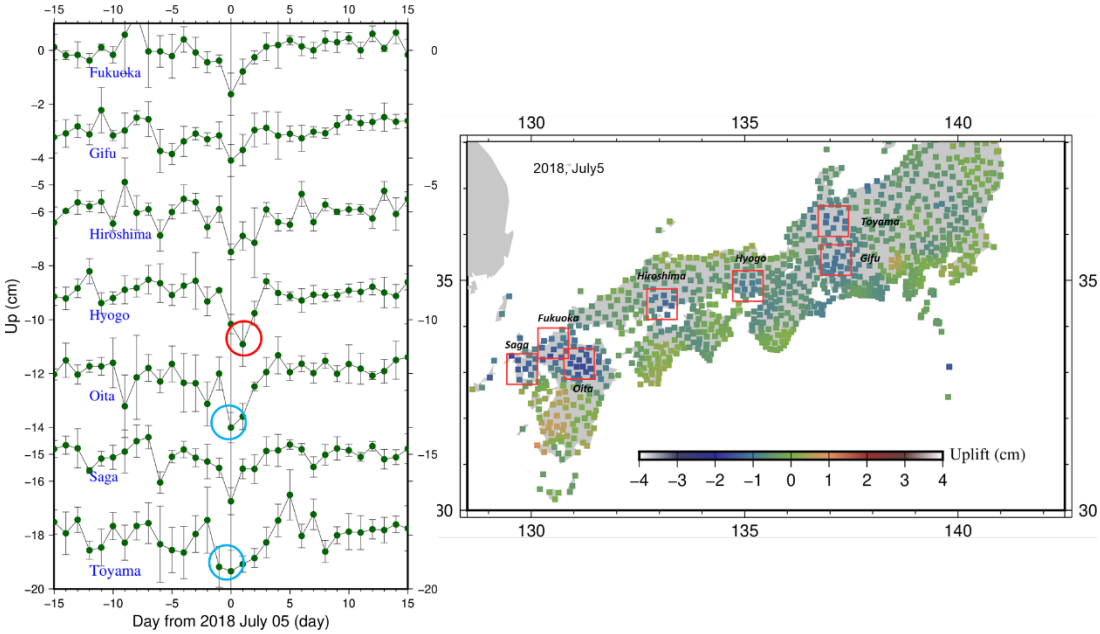

Figure 4.5. Average time series of vertical coordinates of five stations (a) taken from 7 regions indicated as red squares in (b). Origin of the horizontal axis is taken on July 5, 2018. The largest subsidence in Hyogo occurred one day later, i.e., on July 6, 2018 (red circle in a), while they occur on July 5 in other regions. In Oita and Toyama, large subsidence continues for two consecutive days (blue circles in a).

4.2.3 Crustal subsidence in the 2017 and 2019 heavy rain episodes in Kyushu

In addition to the 2018 heavy rain episode, similar disastrous heavy rain occurred in July 2017 and August 2019 in northern Kyushu. Here I obtained the time series of multiple GNSS stations and their averages from the heavy rain area and show them together with the distribution of vertical displacement on the days, 2017 July 05 and

2019 August 28, in Figures 4.6 and 4.7, respectively. The displacement map data are spatially averaged in the same way as the 2018 case.

In the 2017 episode, the heavy rain was quite local and occurred only in northern Kyushu. Accordingly, as shown in Figure 4.6, area of large subsidence is limited to northern Kyushu. This situation is very different from the 2018 case, where wide-spread heavy rain caused floods and consequent crustal subsidence throughout SW Japan (Figure 4.5).

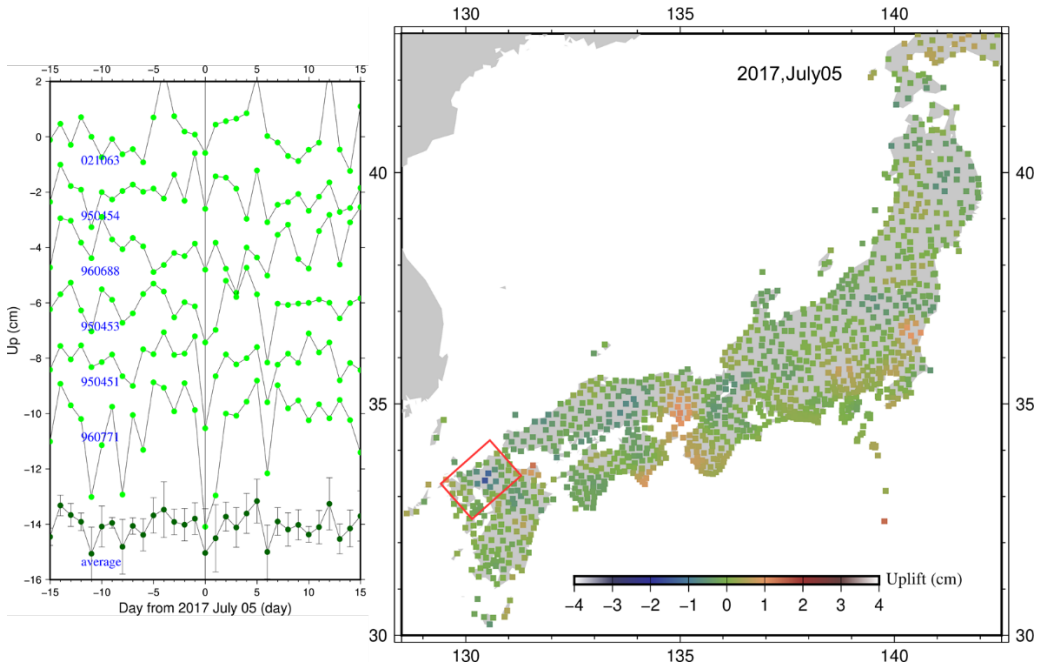

Figure 4.6. (a) Time series of vertical position of six stations in northern Kyushu before and after the 2017 July heavy rain. They are relative to the median position during this period. The bottom time series are derived as the average of these six stations. These stations show subsidence on the day of the heavy rain, July 5, 2017. (b) Map of vertical displacements relative to the 1-month median positions of all GEONET stations on July 5, 2017. Stations in (a) are taken from the region within the red rectangle and spatially smoothed with averaging radius of 20 km.

For the case of August 28, 2019, I picked up the same region and the same 6 stations and plotted the results in Figure 4.7. There, the average land subsidence reached ~1.5 cm. The area of subsidence is larger than in the 2017 event (Figure 4.6) but is less than in the 2018 event (Figure 4.5).

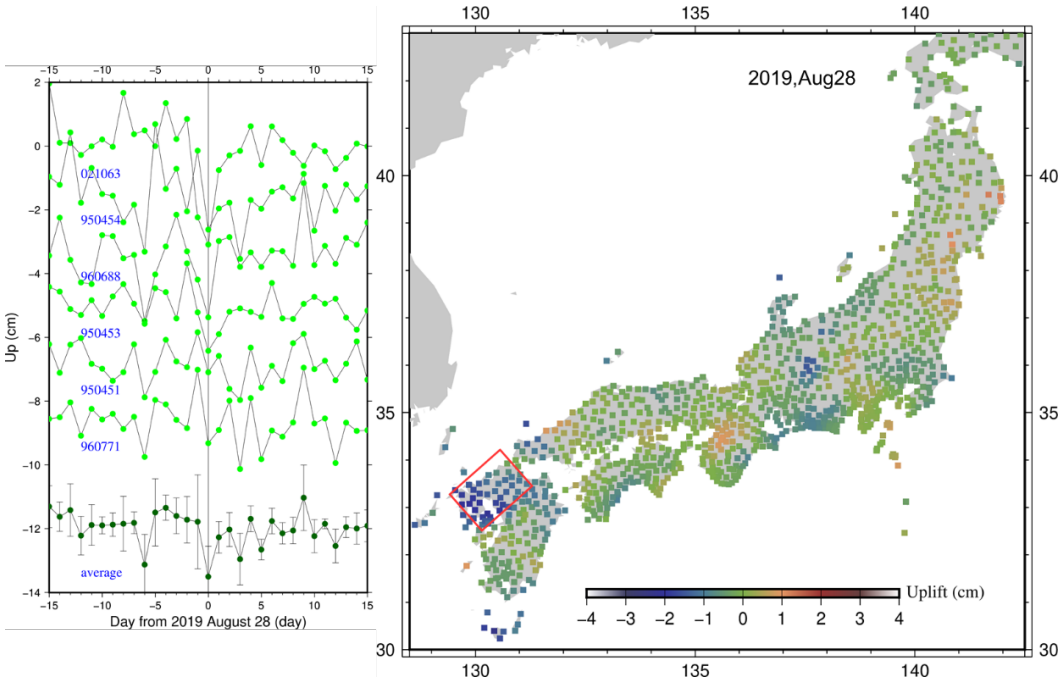

Figure 4.7. (a) Time series of vertical position of six stations in northern Kyushu before and after the 2019 August heavy rain. They are relative to the median position during this period. The bottom time series are derived as the average of these six stations. These stations show subsidence on the day of the heavy rain, August 28, 2019. (b) Map of vertical displacements relative to the 1-month median positions of all GEONET stations on August 28, 2019. Stations in (a) are taken from the region within the red rectangle and spatially smoothed with averaging radius of 20 km.

4.2.4 Day-to-day variability of crustal subsidence: The 5-8 July 2018 case

Here I focus on the days following the peak heavy rain in 2018 July 5. I study crustal subsidence during the days after the peak heavy rain, i.e., 6-8 July 2018. I found the migration of the peak subsidence area and changing amplitude of the subsidence. On the July 6, 2018, I identified 5 subsidence areas, namely Nagasaki, Oita, Ehime, Hyogo, and Toyama Prefectures (Figure 4.8b). On average, I collected the average subsidence using 5 GNSS stations representing each of the five areas. On July 7, large subsidence appeared in areas Nagasaki, Shimane, Okayama, Tokushima, Hyogo, and Shiga Prefectures (Figure 4.8c). However, on the last day of July 8, such subsidence disappeared except in the Gunma Prefecture (Figure 4.8d). This is in accordance with the conditions of heavy rain had begun to decrease on July 8. During the period 5-8 July 2018, I identified 14 areas and days where significant land subsidence occurred, as summarized in Table4.1. The pattern of land subsidence from 5 to 8 July 2018 is characterized as the movement from southwest to central Japan.

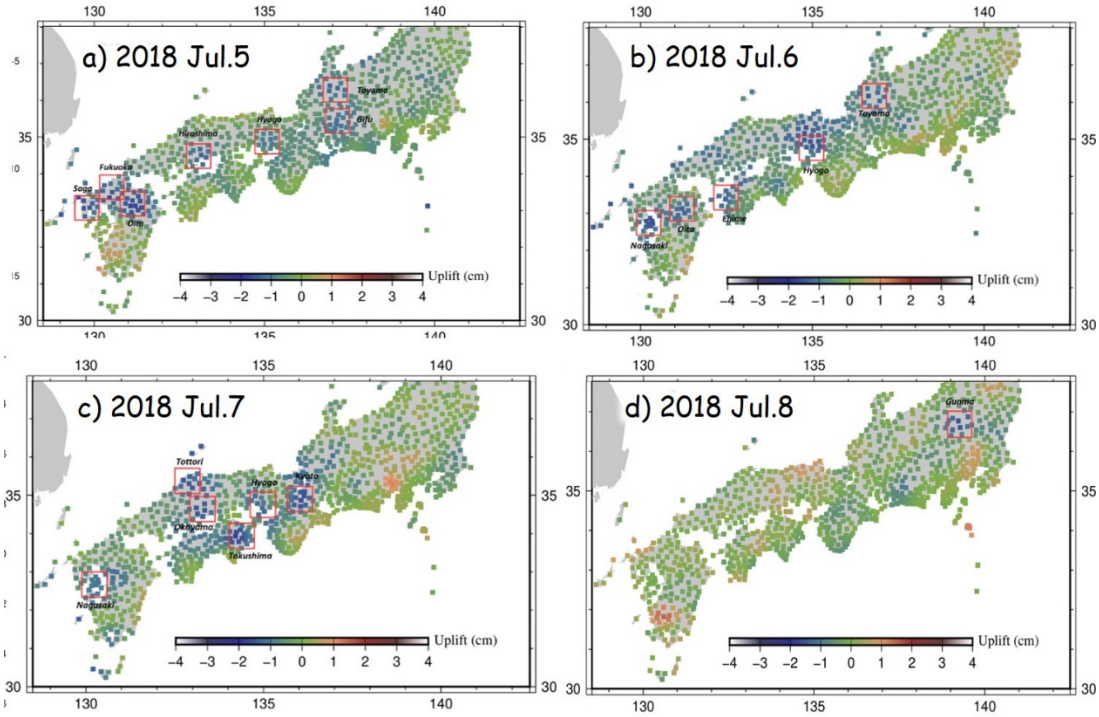

Figure 4.8. Smoothed map of subsidence during a 4 days period following the heavy rain day July 5 (a), 6 (b), 7 (c), and 8 (d) July 2018. Red rectangles show areas of significant subsidence on the special days.

Table4.1. Crustal subsidence calculation results on 5-8 July 2018, in 14 regions, (unit = cm)

No.	Region	5-Jul-18	6-Jul-18	7-Jul-18	8-Jul-18
1	Fukuoka	-1.632			
2	Gifu	-1.091			
3	Hiroshima	-1.488			
4	Hyogo	-1.164	-1.911	-0.758	
5	Oita		-1.641		
6	Saga	-1.743			
7	Toyama		-1.055		
8	Ehime		-1.105		
9	Nagasaki		-1.848	-1.114	
10	Okayama			-0.768	
11	Totto			-1.023	
12	Kyoto			-1.52	
13	Tokushima			-1.401	
14	Gunma				-1.537

4.3 Result and discussions

4.3.1 Estimation of water load from crustal subsidence

Next, I estimate surface water load responsible for crustal subsidence, and I follow the way Milliner et al. (2018) did to infer the dynamics of stormwater from the Hurricane Harvey in southern United States. I use the vertical

displacement field from GNSS station position data over a four-days period, from 5 to 8, July 2018, i.e., those shown in Figure 4.8. Only vertical displacements are used.

The vertical station movements observed during this period is considered to be the deformation by the accumulation of water on the surface (including those in the soil or aquifer). The treatment of water within soil and aquifer is not straightforward. Such water may depress the ground as load, just like surface water. At the same time, it may cause uplift by inflating the soil or aquifer, as shown in Figure 4.3c. In this study, I only consider loads, i.e., depression of ground by surface mass, and it is beyond the scope of the thesis to discuss their status, surface water, soil moisture, or groundwater.

First, I set up blocks with dimension 1/4 degrees in latitude 1/6 degrees in longitude and assume that the water depth is uniform within individual blocks. Subsidence S by surface load when the earth is treated as an elastic substance is obtained as follows by using the Green's function (Farrell, 1972).

$$S(\theta, \lambda) = \rho_w \int\int H(\theta', \lambda') \, Gr(\phi) \, d\theta' d\lambda' \tag{4.1}$$

θ, λ : Latitude and longitude in the observing point, θ', λ' : Latitude and longitude of load

ρ_w : water density, H : water depth, ϕ : distance between load (θ', λ') and observing point (θ, λ)

Gr : Green's function, S: Crustal subsidence

Actually, the areal integration is replaced by the addition of subsidence caused by discrete number of blocks whose area is A. Subsidence of the j'th GNSS station at (θ_j, λ_j) can be expressed as the sum of the contributions from M loads. Let ϕ_{ij} be the distance between the i'th load and the j'th GNSS station, then (4.1) becomes

$$S(\theta_j, \lambda_j) = \rho_w A \, \Sigma^{M}_{i=1} H(\theta_i, \lambda_i) \, Gr(\phi_{ij}). \tag{4.2}$$

In the forward approach, I could tune the load distribution so that the calculated subsidence at the GNSS stations coincides with the observed values. Here I performed least-squares inversion to estimate $H(\theta_i, \lambda_i)$ (i=1… M) as the parameters and using S (θ_j, λ_j) (j=1,…, N) as the input data. In this case, M is 1323, i.e., I set up 1323 blocks with the dimension of 1/4 degrees in latitude and 1/6 degrees in longitude covering the land area of SW Japan.

N is the number of GNSS stations, and it is only about a half of the number of load blocks (number of GNSS stations in SW Japan is about 1/2 of the total GEONET station number). To regularize the inversion, I introduced

the continuity constraint, i.e., I assumed the neighboring blocks have same load values *H* with a specific allowance. I gave the allowance of 100 cm, i.e., the standard deviation of the difference between adjacent blocks is ~100 cm. I also assumed the observing error of the vertical position as 5 cm. In addition to the continuity constraint, I constrained the water load around zero for coastal blocks (blocks with one of the four sides is not connected to another block) with allowance equal to the continuity constraint. This is equivalent to the assumption to assume zero load for the ocean (precipitation on ocean flows out and does not stay there).

4.3.2 Estimated surface water load

Next, I analyze the terrestrial water load estimated from crustal subsidence. Figure 4.9 compares the observed and calculated subsidence and the distribution of the estimated load.

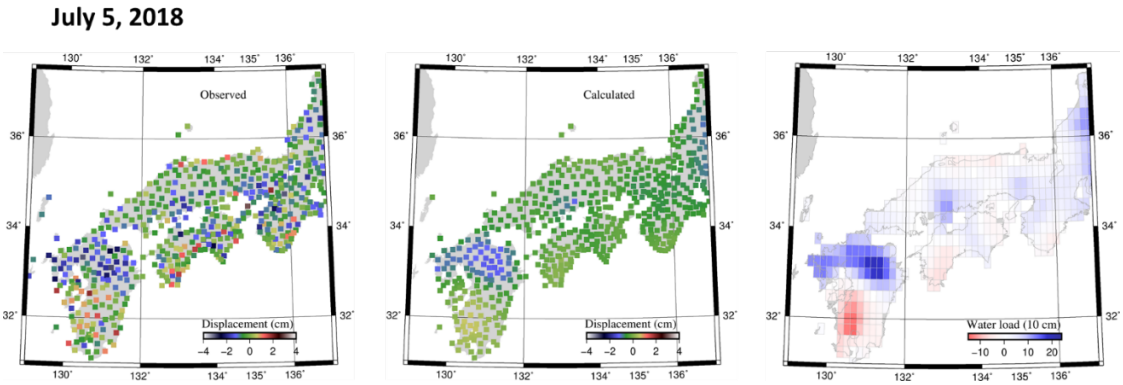

Figure 4.9. The observed (left) and calculated (middle) subsidence of GNSS stations on July 5, 2018. The estimated distribution of surface water load (right) shows the total volume of surface water as 68.2 km^3 (68.2 Gt as the mass). The number of stations used in the calculation is 613, and the post-fit residual RMS is 2.18 cm. The unit of the water load is 10 cm, and so "10" means 100 cm.

Next, I repeated the same calculation for three more days, 6-8 July 2018. They are shown together with the July 5 results in Figure 4.10. The recovered total amount of surface water over the period July 5 -8, 2018, is 68.2 km^3, 72.3 km^3, 67.6 km^3, and 19.3 km^3 (Figure 4.10). I also can see the eastward migration of the load, i.e., they appeared first in northern Kyushu, and the center of load moved to the Chugoku District and then to the Kansai District. Water mostly disappeared on July 8, 2018.

These results are consistent with the report from Japan Meteorological Agency (JMA) (http://www.data.jma.go.jp/obd/stats/data/bosai/report/2018/20180713/jyun_sokuji20180628-0708.pdf : page 21-23), i.e., the warning issued first at 08 UT on July 06 in Kyushu, then in Chugoku at 11 UT on the same day, and finally in the Kinki District at 14 UT. On July 8, 2018, Figure 4.10 shows some amount of uplift, and this may come from the aquifer inflation after the stormwater became groundwater, as shown in Figure 4.3c.

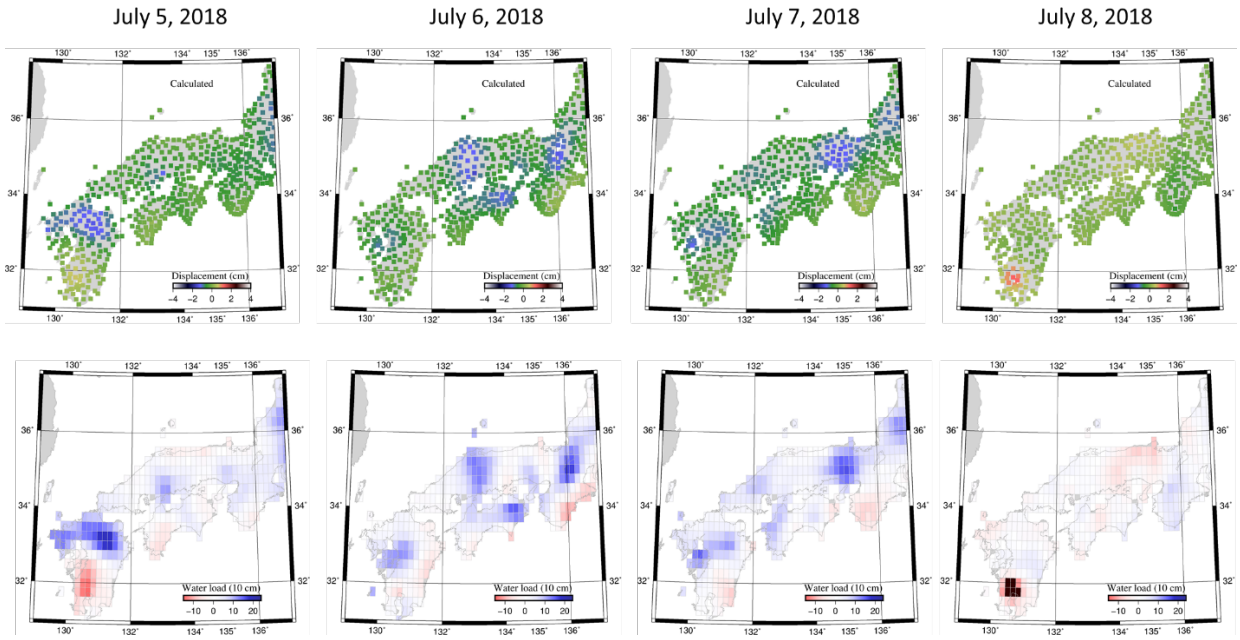

Figure 4.10. The calculated vertical movements (top) and load distribution (bottom) for the 4 days period July 5-8, 2018. The recovered total amount of surface water over the period July 5-8, 2018, is 68.2 km^3, 72.3 km^3, 67.6 km^3, and 19.3 km^3, respectively.

Next, I count the cumulative rainfall that occurred over this period. The data come from AMeDAS rain gauges run by JMA. This shows how much water is recorded at the AMeDAS ground stations. I calculate the daily values of cumulative rains for 4-7 July, 2018, and the results are given in Figure 4.11.

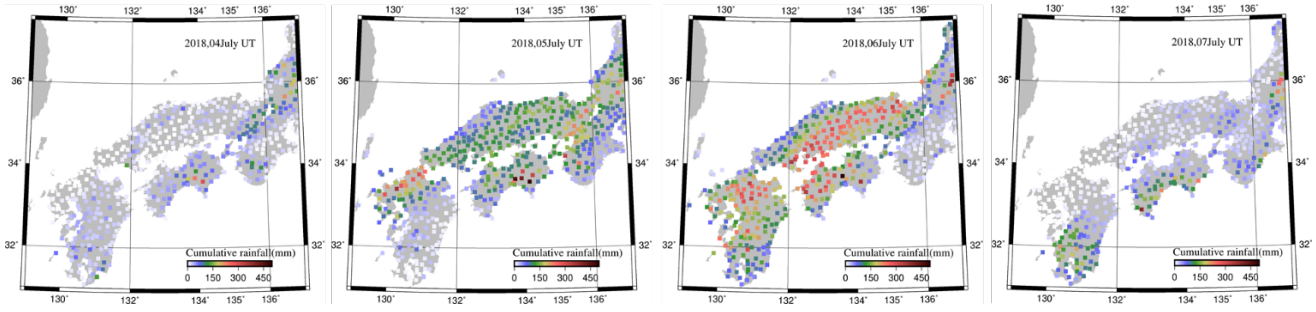

Figure 4.11. The cumulative rainfall calculated from rain gauge data at all AMeDAS-JMA stations. These values are expected to be correlated with the amount of water load in Figure 4.10 (bottom). For the period 4-7 July 2018, the daily cumulative precipitation at the AMeDAS stations are 5.2 km^3, 16.8 km^3, 21.7 km3, and 7.5 km^3, respectively.

The results show that the amount of water inferred from crustal subsidence is significantly higher than the AMeDAS rain gauge results. This might be explained by the three factors, (1) The AMeDAS rain is underestimated. In general, there is more water in high mountains, but AMeDAS stations tend to be built in valleys. Hence, the real amount of the rainfall will be more than AMeDAS rain gauge data show. (2) AMeDAS data are cumulative amount of rain over one day, but surface water may reflect rain over the past few days. (3) GNSS stations tend to be installed the valley where rain concentrate (discussed later with Figure 4.13).

To address problem (1), I compare the AMeDAS rain gauge data with the radar rain-gauge analyzed precipitation (RRAP) data, obtained by calibrating the rain radar data with the AMeDAS rain gauge data. They cover the land continuously with spatial resolution of ~1 km, and do not suffer significantly from non-uniform distribution of the AMeDAS stations.

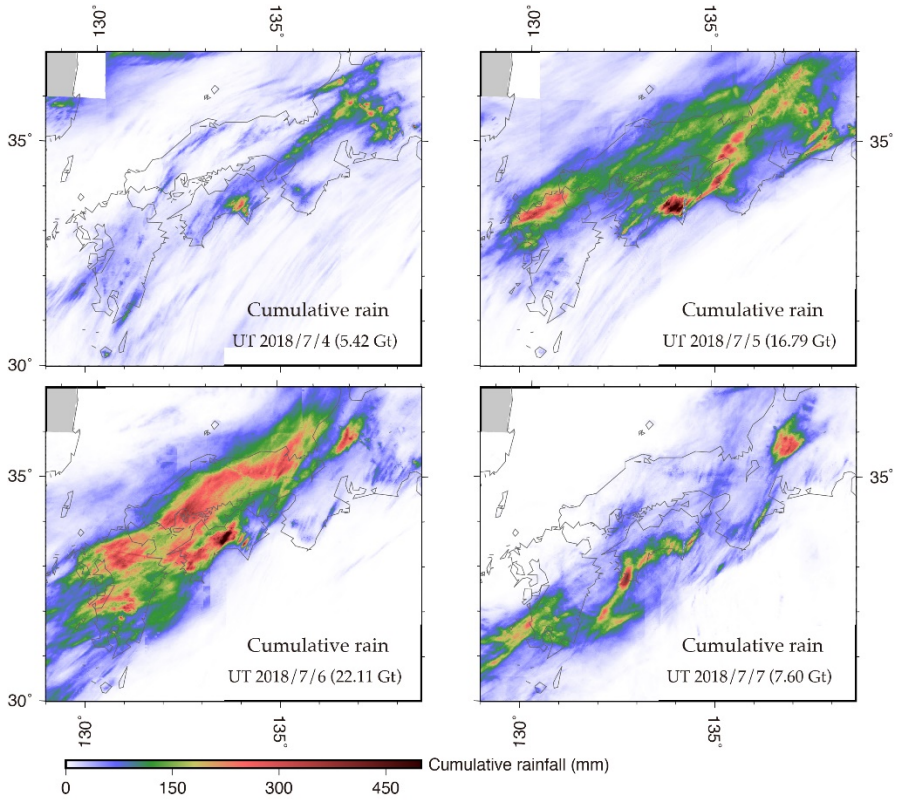

Figure 4.12. The high-resolution cumulative rainfall calculated using the radar data calibrated with conventional rain gauge data (officially called the "Radar Raingauge Analyzed Precipitation"). For the period 4-7 July 2018, the daily volume of water from this data set is 5.42 km3, 16.79 km3, 22.11 km3, and 7.60 km^3, respectively. These cumulative rainfall values are only slightly lager than the AMeDAS rain gauge data shown in Figure 4.11.

I also discuss the problem (2), I tried to add up the amount of AMeDAS rainfall water from 4 to 7 July 2018 and found the sum around 51.2 km^3. This amount is close to the amount of the water load estimated from the crustal movement on July 7, 2018 (67.6 km^3), However, the crustal movement time series (Figures 4.5, 4.6, 4.7) suggest rapid drain of rainwater to the sea (with timescales of 1-2 days), and it is difficult to consider the water stay on surface for 4 days or more.

To assess problem (3), I compare GNSS station altitudes with the average altitudes of the surrounding terrain. In Figure 4.13, we can see that altitudes of the GNSS stations are significantly lower than the surrouding region (e.g. stations are built along valleys surrounded by highland). This would let rainwater concentrate around GNSS stations, causing extra subsidence of GNSS antenna relative to the average subsidence of the region. By

using such biased subsidence data, one would naturally overestimate the amount of water on the surface. It is likely that this problem (3) is largely responsible for the discrepancy between the estimated water load and precipitation. Additionally, thick sedimentary layers beneath the GEONET stations may also locally reduce the crustal rigidity. After all, it is not a simple matter to evaluate such a "topography factor" quantitatively.

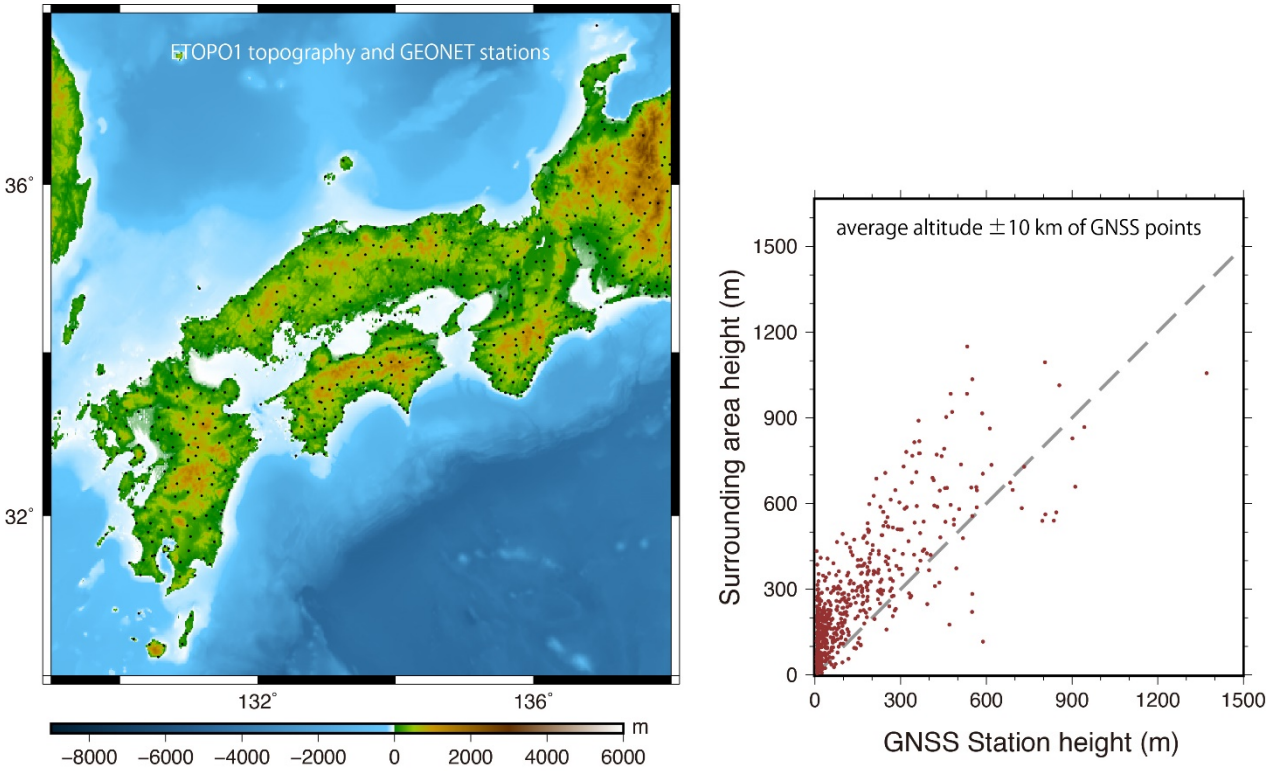

Figure 4.13. GEONET stations (black dots) drawn in the ETOPO1 topographic map (left), and comparison of GEONET station altitude with the average altitude of a square (20 km x 20 km, with the GNSS station at the center). If they coincide, the data would distribute around the dashed line.

4.3.3 Amount water vapor in the sky

As shown in Chapter 3 and in Arief and Heki (2020), I estimated sea-level ZWD at grid points all over Japan, for the heavy rain episodes in 2017, 2018 and 2019. We could convert the estimated sea-level ZWD into the amount of atmospheric water vapor with the conversion factor $\prod$, which is approximately 0.15 (this value actually depends on T_m). As described in detail in Section 3.1, UNR data base now provides PWV in addition to ZTD and tropospheric delay gradients. Here I directly used such sea-level PWV data estimated in the same way as the sea-level ZWD. Total amount of PWV tells how much water exists in the sky in the form of water vapor. Then, I integrated the PWV over Japan by spatially integrating them. I give an example for the 2018 July heavy rain episode in Figure 4.14.

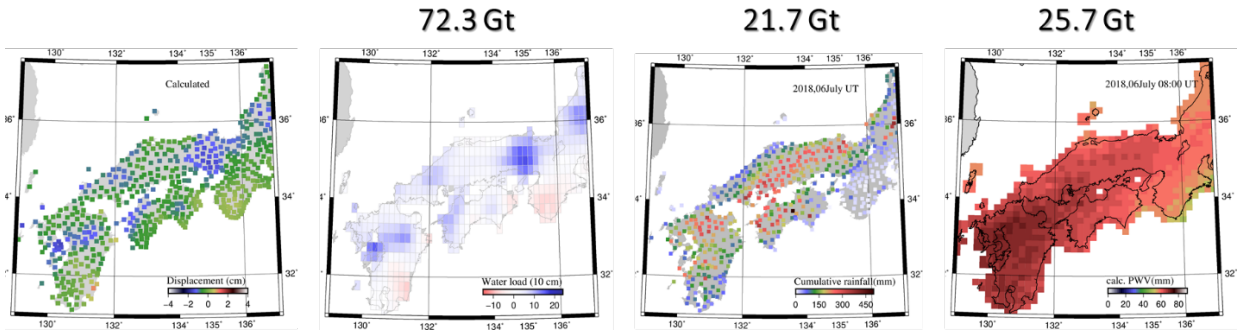

Figure 4.14. Comparison of the total amount of water above SW Japan during the 2018 heavy rain episode, inferred in three different ways. The second panel from the left shows the water estimated from the crustal subsidence (left panel). The second panel from the right shows the precipitation at the AMeDAS stations from rain gauges. The right panel shows the precipitation water vapor (PWV). The volume of water estimated from the crustal subsidence, AMeDAS rain gauge, and PWV are, are 72.3 km^3, 21.7 km^3, and 25.7 km^3, respectively.

Figure 4.14 compares the total amount of water above SW Japan during the 2018 heavy rain episode, inferred in three different ways. They include the amount of water estimated from crustal subsidence, precipitation from AMeDAS rain gauges, and sea-level PWV reconstructed from PWVs in low-altitude stations by GNSS-MET approach. In Figure 4.15, I compare these three quantities for the 2017 and 2019 heavy rain episodes.

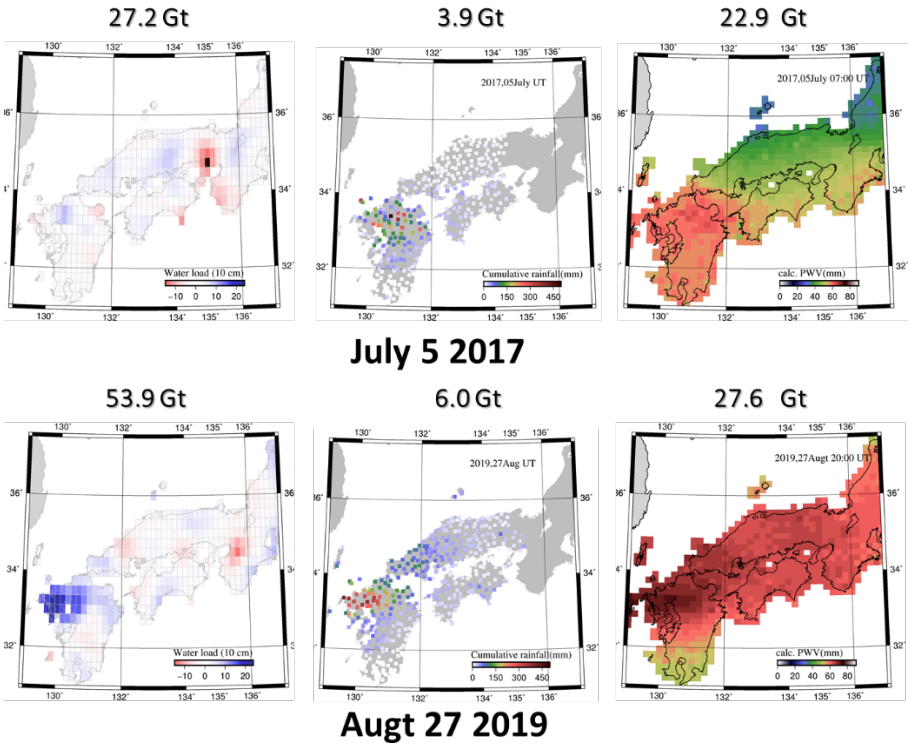

Figure 4.15. Comparison of the amount of water from three approaches for the 2017 and 2019 heavy rain episodes in SW Japan. See the caption of Figure 4.14 for detail.

As seen from Figures 4.12 and 4.13, the amount of surface water estimated from crustal subsidence exceeds the precipitation. This is physically strange, because only a part of the precipitation would stay on the ground and

other parts would run-off to the sea. This paradox stays unsolved in this thesis, and future studies would clarify the origin of the discrepancy.

Chapter 5. Analysis of the Tropospheric Delays in Indonesia Estimated using the goGPS software

5.1 Introduction

In the GNSS data analysis to obtain tropospheric parameters (Chapter 3) and station positions (Chapter 4), I did not estimate them myself but downloaded them from appropriate data sets available from various research centers, such as UNR and GSI. These studies are performed for heavy rain episodes in the Japan area where large number of GNSS stations are available. In this chapter, I try to analyze the GNSS data taken in Indonesia. Here, I estimate tropospheric parameters as well as station positions using an alternative way, i.e. data analysis made by myself using an appropriate GNSS software package.

UNAVCO (https://www.unavco.org/software/data-processing/postprocessing/postprocessing.html) says that there are 3 distributions of GNSS software based on their use: "Research-Level", "Open-Source" and "Commercial". I think the use of Open-Source software in Indonesia is quite promising and will develop rapidly considering that it is easy to obtain and simple to operate to get results.

The goal of this chapter is simply to show that GNSS meteorology can be applied in Indonesia as well as in Japan, by estimating zenith tropospheric delays (ZTD) from continuous GNSS stations in Indonesia, using one such software package "goGPS". At first, as the evaluation of the goGPS performance, I compared the estimated tropospheric delay gradients and ZTD from goGPS with other products from IGS and UNR. Then I compare the ZTD values from goGPS during the dry and rainy seasons. Finally, I compare the PWV time series with the daily rain data, during the dry season and the rainy season 2015-2016.

5.2 Data and Methods

5.2.1 Data set

The primary format of the GNSS data that I use in this study is the Receiver Independent Exchange (RINEX) format. As the first station, I use the BAKO station with coordinates 106.5E -6.3N managed by BIG / BAKOSURTANAL, and I use, as the second station, the JOG2 station with coordinates 110.2E -7.4N, which is

managed by GFZ (Geoforschungs Zentrum), the German Geo-research Center. As the period of this study, I use days of the year (DOY) 022-025, 22-25 January, and DOY 230-233, August 17-20, 2018. The former represents the rainy season, and the latte represents the dry season. Next, I process RINEX files to estimate tropospheric parameters using sophisticated open-source GNSS software, called goGPS, version 1.0 Beta, from Geomatics Research and Development s.r.l. - Lomazzo, Italy (Realini, 2009).

5.2.2 Software goGPS

The leading software for processing RINEX data, goGPS. (Realini, 2009), is an open-source software initially developed by Dr. E. Realini (with contributions from the various thesis works by master students) since 2007 at the Geomatics Laboratory of Politecnico in Milano, Como Campus. It is specifically designed to improve the positioning accuracy of low-cost GNSS devices by relative positioning and the Kalman filtering technique. goGPS code was published online as free and open-source software in 2009. The project is open to collaborations since its publication, and it has received supports and code contributions by users working in both academy and business companies in different countries (including Italy, Japan, Switzerland, Spain, and Germany). Strategies for processing RINEX data with goGPS are as shown below,

goGPS 1.0 Beta	
Strategy	Constellation: multi GNSS Processing technique: precise point positioning (PPP) Elevation cut-off angle: 7° Data processed in a two 24 h sessions (from 00:00 to24:00 UTC and from 12:00 UTC on day *D* to 12:00 UTC on day *D*+1) Frequency: L1, L2
Orbits and clocks	Fixed to JPL final orbits and clocks
Observation rate	30s sampling rate
Observation weighting	Uniform - all observations equally weighted
Tropospheric modeling	Niel Mapping Function Macmillan Mapping function for gradients A-priori zenith delay - VMF gridded zenith delays Meteorological data - Standard Atmosphere
Tropospheric estimates	One ZWD per 30 seconds, One tropospheric gradient per 30 seconds

5.2.3 Precision Point Positioning (PPP)

The precise point positioning is used as a post-processing method for determining the absolute position using stand-alone (thus un-differenced) GNSS receivers. GNSS PPP processing uses the ionosphere-free combinations of dual-frequency pseudoranges and carrier-phase observations. The preference for PPP instead of double-

difference (DD) processing arises from the benefit that (1) each GNSS station can be processed independently, and that (2) simultaneous observation of the same satellite of the two stations are not needed (Yuan et al. 2014). To compare and validate the ZTD values I estimated with goGPS, I used two international tropospheric products from International GNSS Services (IGS) with commercial software version 5 of the Bernese software, and the other products from University of Nevada Reno (UNR) obtained using the GIPSY / OASIS II software from NASA Jet Propulsion Laboratory (JPL) (Blewitt et al., 2018).

5.3 Result and discussions

5.3.1 Comparison of the estimated tropospheric delay gradients with other products

Here I compare estimated atmospheric delay gradient vectors using the data from the JOG2 station on August 20, 2018 with those from other products, namely those from IGS and UNR. The correlation of the goGPS and IGS delay gradient values for the north is 0.47 and 0.41 for the east, while the correlation between the goGPS and UNR delay gradient values is 0.71 for the north and 0.75 for the east. I plot them in Figure 5.1 and Figure 5.2

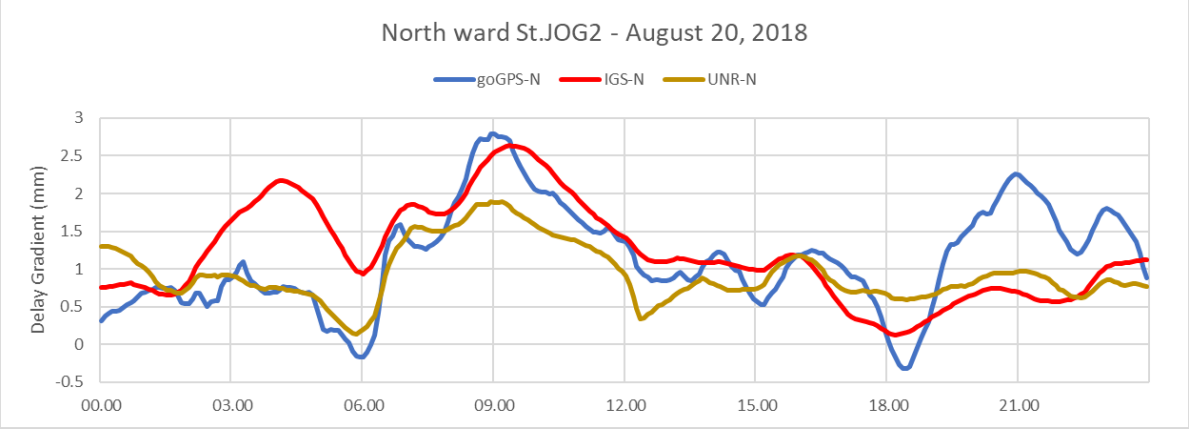

Figure 5.1. Comparison of north component of the atmospheric delay gradient, between goGPS, IGS and UNR. Correlation of goGPS results with those from IGS and UNR is quite high.

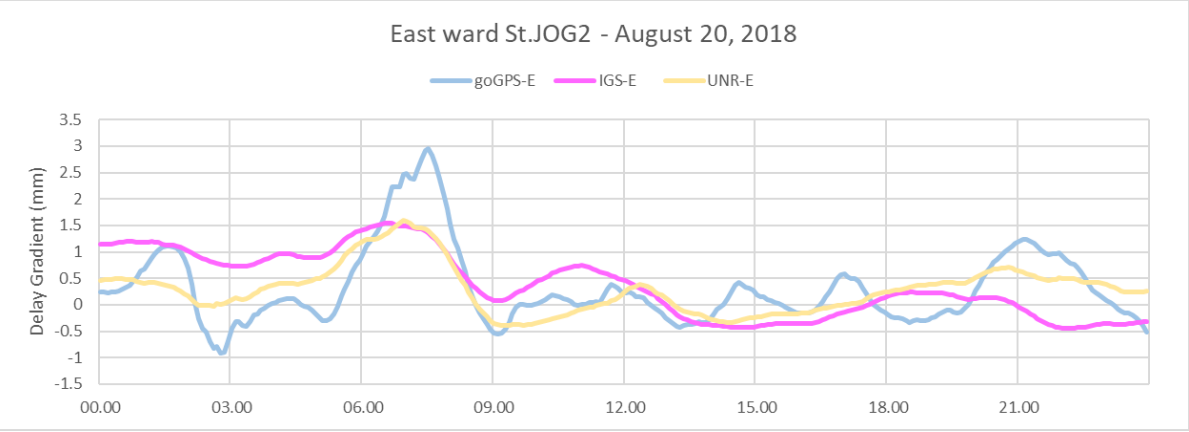

Figure 5.2. Comparison of the east component of the atmospheric delay gradient, between goGPS, IGS and UNR. Correlation of goGPS results with those from IGS and UNR is quite high.

From the correlation value the goGPS delay gradients and the IGS and UNR products show good consistency, although the goGPS solution shows more short-period changes. As a whole, the data processing with goGPS is good enough to get accurate values of not only the ZTD (to be discussed in 5.3.3) but also the delay gradients. Therefore, in this research, I estimate ZTD using goGPS software together with the tropospheric delay gradients.

5.3.2 Comparison of the ZTD values of goGPS, IGS and UNR

Next, I compare the ZTD values for the three solutions, namely goGPS, IGS and UNR, using the BAKO and JOG2 stations, on January 24, 2018 and August 20, 2018. This is as part of the validation process of determining ZTD values with goGPS.

The results show a small RMS value <2 mm. The RMS value is relatively small, meaning that the tropospheric parameters estimated with goGPS show good agreement with the products from UNR and IGS.

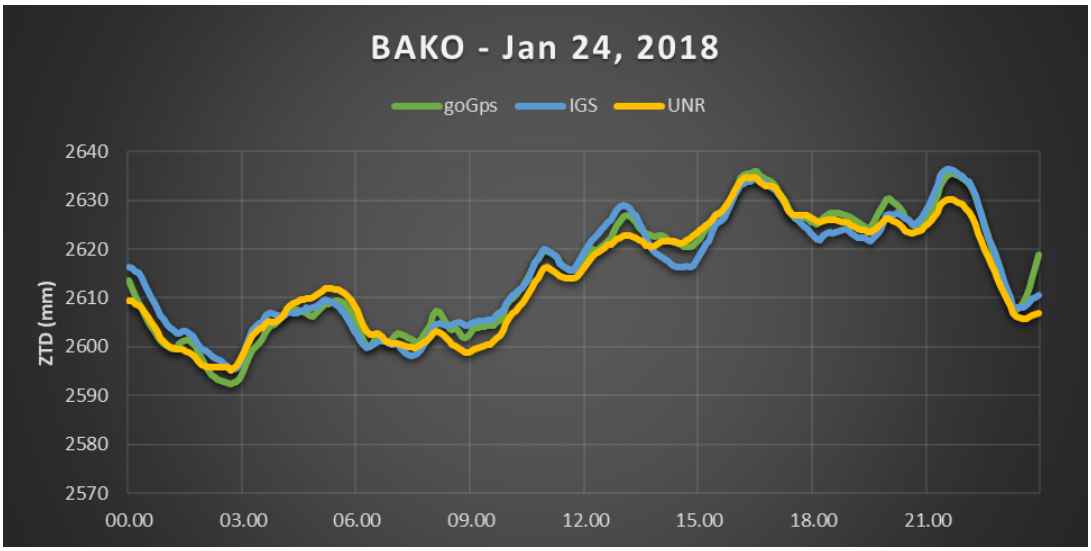

Figure 5.3. ZTD time series from goGPS, IGS, and UNR, during 24, Jan. 2018, at the BAKO station. The standard deviation and RMS of the difference between goGPS and IGS are 12.03, 0.81, respectively (in mm). Those for the goGPS-UNR pair are 11.22, 0.66

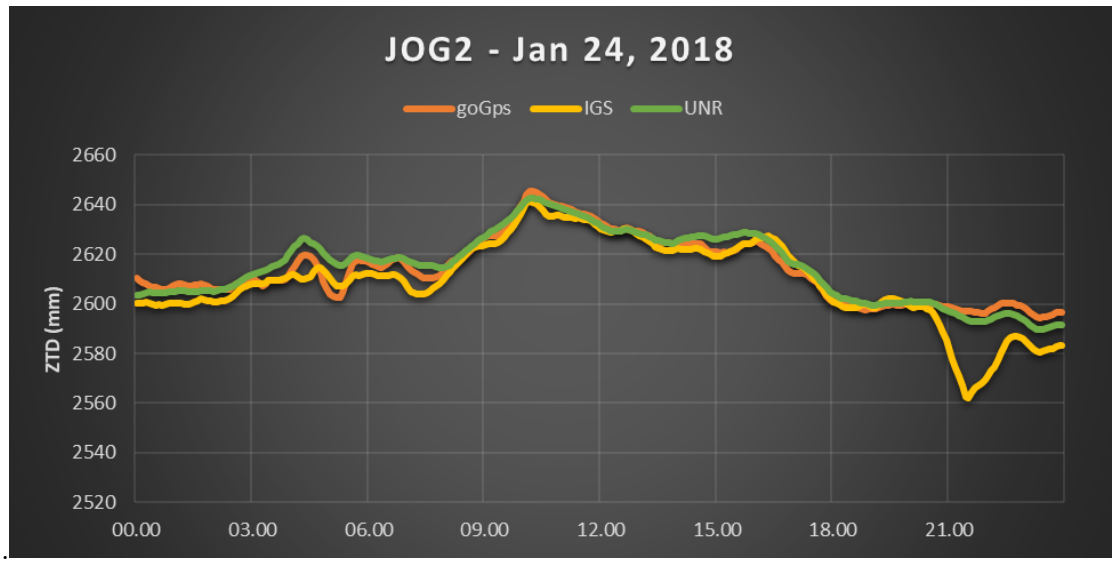

Figure 5.4. Same as in Figure 5.3, but the BAKO station is replaced by the JOG2 station. The standard deviation and RMS of difference between goGPS and IGS are 16.11 and 1.11, respectively (in mm). Those for the goGPS-UNR pair are 15.00, 1.63.

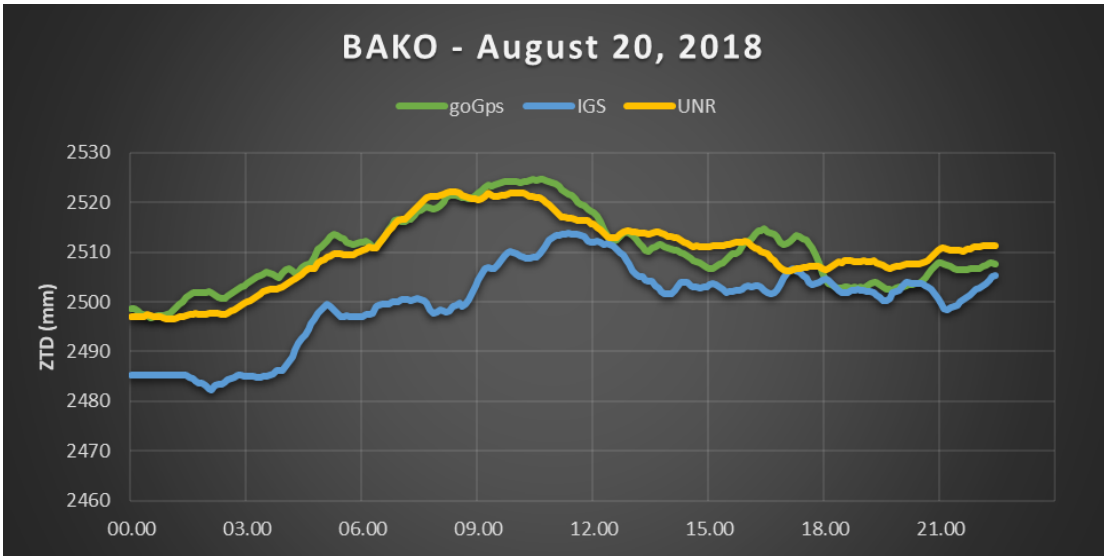

Figure 5.5. Same as Figure 5.3, but the date is 20 Augt 2018. The standard deviation and RMS of the difference between goGPS and IGS are 7.44 and -0.66, respectively (in mm). Those for the goGPS-UNR pair are 8.09 and 0.26.

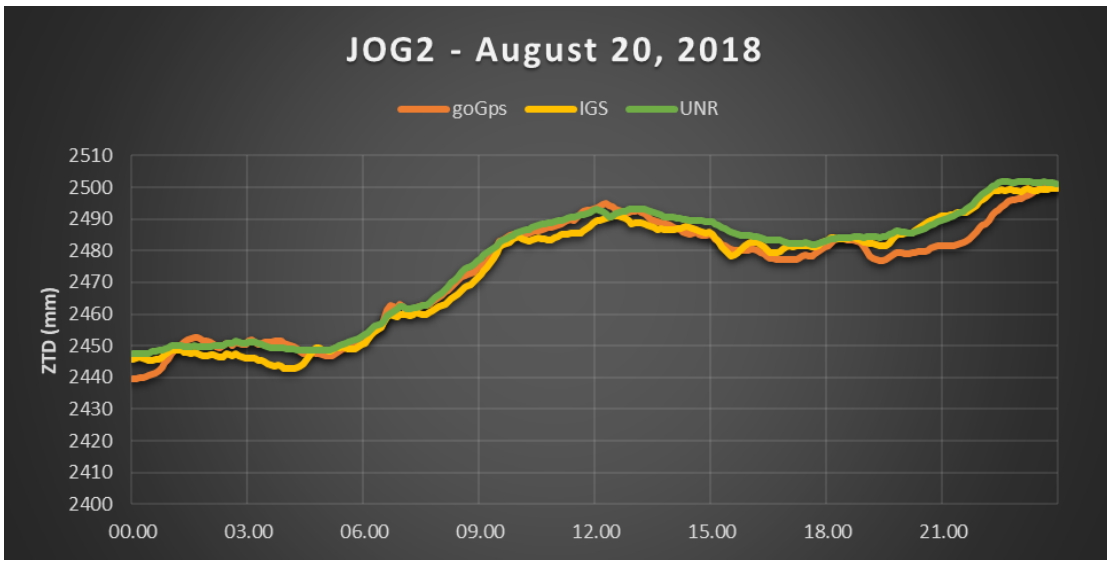

Figure 5.6. Same as in Figure 5.5, but the BAKO station is replaced by JOG2 station. The standard deviation and RMS of difference between goGPS and IGS are 16.99 and -1.32, respectively (in mm). Those for the goGPS-UNR pair are 18.33 and -1.08.

The results of the ZTD values that I obtained using goGPS, both in January 24 and August 20 and the BAKO and JOG2 stations, are shown in Figures 5.3 - 5.6. The whole pictures show the consistency of the ZTD value from goGPS with other solutions. The goGPS software package works quite well at different times and stations. This means that it can be an alternative to commercial software systems for the ZTD estimation.

5.3.3 ZTD range value from goGPS

Next, I tried to make a range of ZTD values to see the difference between the existing seasons in Indonesia, namely the rainy season and the dry season. First, I process data from the BAKO and JOG2 stations from 22 to 25 January 2018. The rate of atmospheric parameter estimation is every 5 minutes, and so we get 288 values data for one day (24 hours). From these 288 data, I get the smallest, the most significant, and the average values, as presented in Figure 5.7.

Next, I carried out the same process from 18 to 21 August 2018. I present the results in Figure 5.8. ZTD values from 22 to 25 January 2018 (rainy season) in the BAKO station tend to be higher than those from 18 to 21 August (dry season) 2018. Likewise, at the JOG2 station, ZTD in January 2018 is higher than those in August

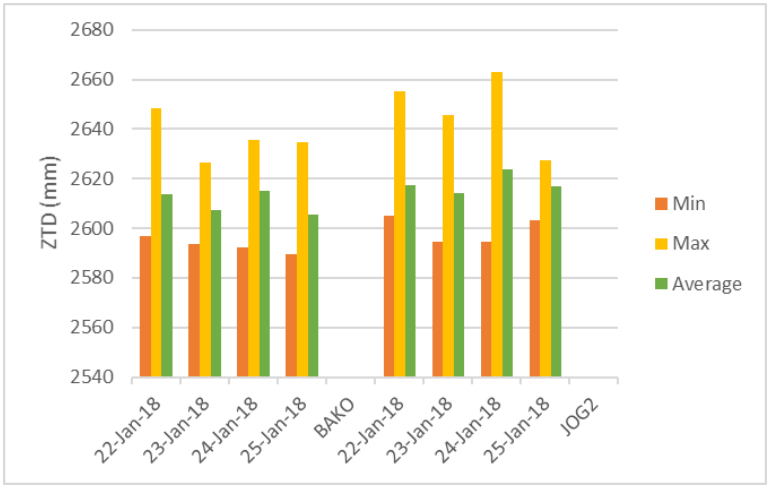

Figure 5.7. Minimum, maximum, and the average ZTD values for 22-25 Jan 2018 at BAKO and JOG2 stations

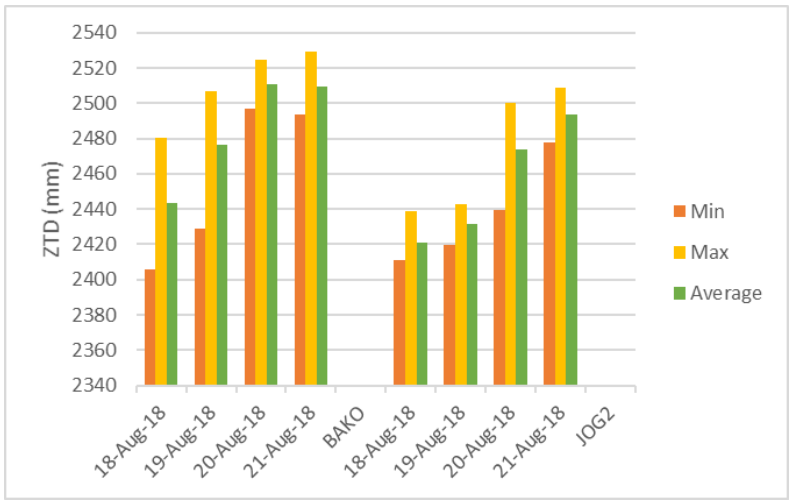

Figure 5.8. Minimum, maximum and the average ZTD values for 18-21 Aug. 2018 at the BAKO and JOG2 stations. The difference of about -100 mm from those shown in Figure 5.7 reflects the smaller amount of water vapor during the dry season.

Figure 5.7 and Figure 5.8 show that there are large seasonal differences in the ZTD value, and this difference reflects the seasons in Indonesia. The ZTD values obtained by the goGPS software clearly showed the difference between the rainy season (January) and the dry season (August). In subsection 5.3.4, I will try to compare ZTD values with daily rainfall conditions and radiosonde data.

5.3.4 Comparison of PWV and rainfall

The software package goGPS can estimate not only ZTD but can also isolate ZWD and convert it to PWV. Here I try to compare the PWV values from GPS receivers at the CMAK station in Makassar, South Sulawesi, with the PWV value observed at the WAAA radiosonde station in Makassar City. The altitudes of the CMAK stations and the WAAA stations are 77,595 m and 13 m, respectively, while the distance between CMAK and WAAA stations

is about 18 km. I perform the comparison in the dry season, April - September 2015, and in the rainy season, October 2015 - March 2016. The results are given in Figures 5.8 and 5.9.

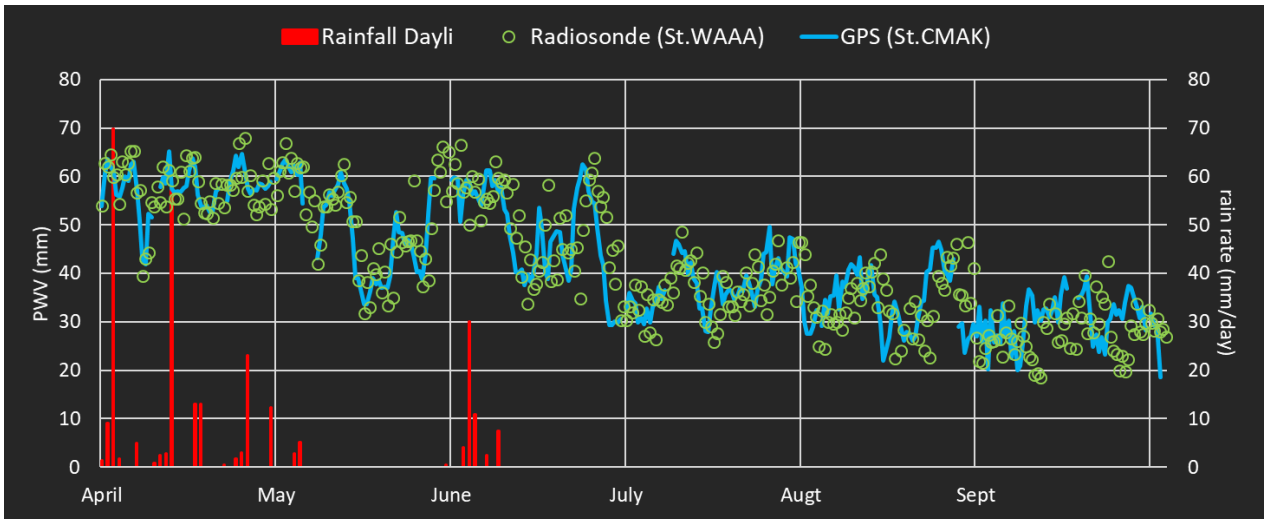

Figure 5.9. Comparison of PWV values from goGPS and radiosonde, together with the daily rainfall data in the city of Makassar during the dry season in 2015.

The correlation of PWV values from GPS and radiosonde for the dry season (Figure 5.9) and in the rainy season (Figure 5.10) are 0.84 and 0.73, respectively.

Figure 5.9 shows that the PWV value during this dry period has a negative trend. On the other hand, Figure 5.10 shows the positive trend of PWV during this period of the rainy season. The RMS values of the differences between the goGPS PWV and radiosonde are 0.91mm in the dry season of and 1.31mm in the rainy season. Thus, the PWV values from goGPS and radiosonde are mostly consistent with each other.

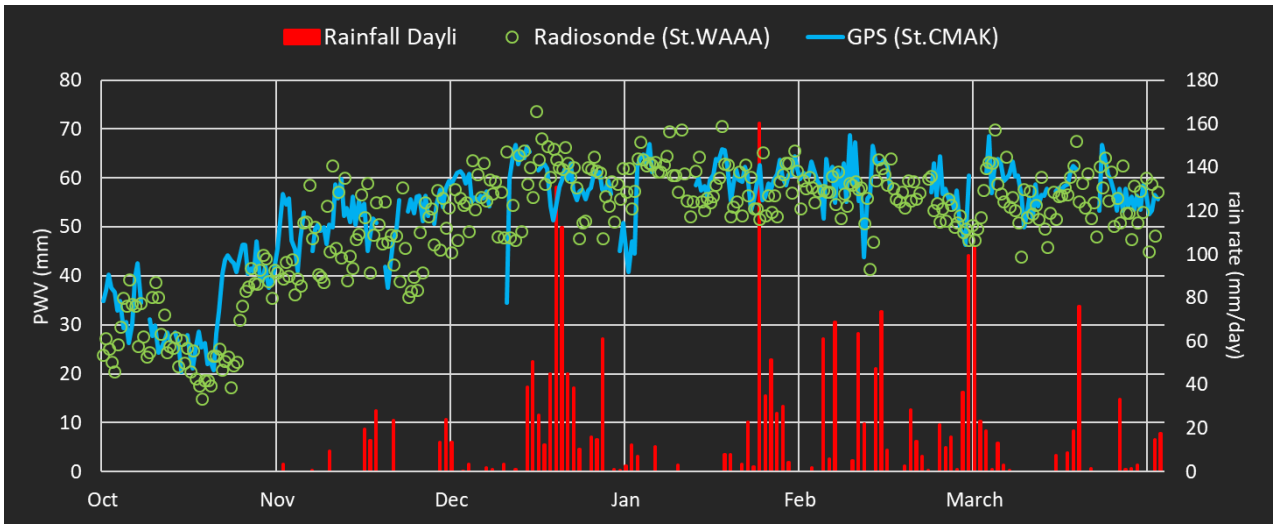

Figure 5.10. Comparison of PWV values estimated by the goGPS software and those measured by radiosonde, together with the daily rainfall data in the city of Makassar. The period corresponds to the rainy season from 2015 to 2016.

Figures 5.9 and 5.10 illustrate the contrast between seasons in Indonesia, the dry season of April-September 2015 and the rainy season of October 2015-March 2016 using the daily rainfall and the PWV values, from the goGPS GNSS data processing and the conventional radiosonde data.

Chapter 6. Correlation between land subsidence and heavy rainfall in Jakarta on January 1, 2020

6.1 Introduction Jakarta flood on January 1, 2020

In this chapter, I try to apply the GNSS meteorology to the heavy rain events in early 2020 in Jakarta, and to study the correlation between rainfall and the land subsidence in the heavy rainfall area. Jakarta suffered from a flood on January 1, 2020. According to a report from the Indonesian Meteorology and Climatology Geophysics Agency (BMKG), the main cause was the heavy rainfall. The rain gauge at the Halim Perdanakusuma station showed the rainfall of 377 mm on that day. The rain gauge at the station Taman Mini and Jatiasih recorded rain amounting to 335 mm/day and 260 mm/day, respectively. This rainfall distribution covers a large area and is quite high in value as in Figure 6.1

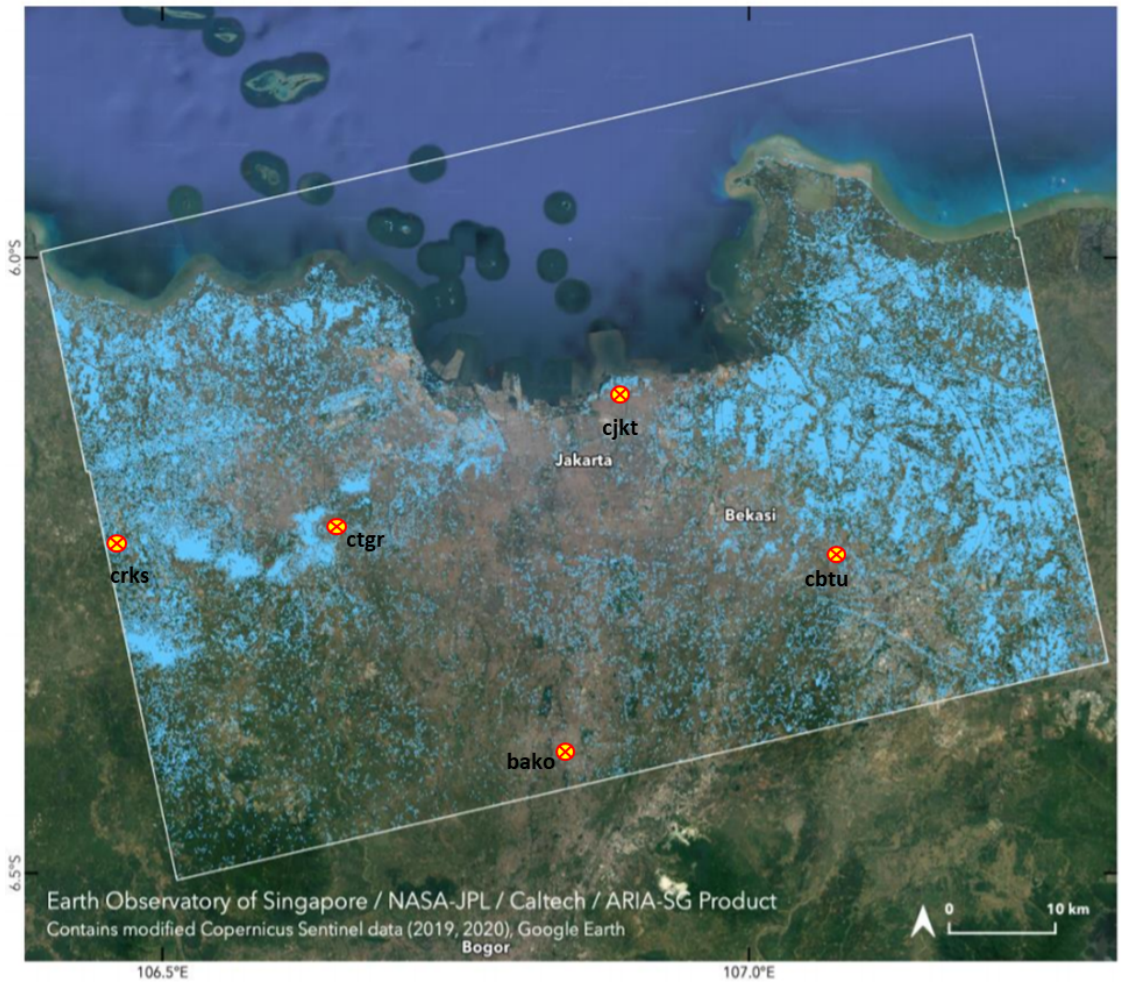

Figure 6.1, Map of the areas in Greater Jakarta showing the likely flooded areas (light blue pixels), based on synthetic aperture radar satellite data before (21 December 2019) and during (02 January 2020) the flood event. Based on the web page https://earthobservatory.nasa.gov/images/146113/torrential-rains-flood-indonesia, I identified at least 5 GNSS stations with separations of ~30 km from each other.

The largest rainfall of 377 mm/day is recorded in BMKG, and this is the highest value in the history of rain records in Jakarta. Jakarta, as the capital city of Indonesia, is an important area that should get attention related to the occurrence of floods due to heavy rains. Today, GNNS has been widely used for meteorological purposes, as explained in the previous chapter, in addition to the primary function for measuring crustal movement and for mapping surveys. Here, I tried to analyze the link of heavy rainfall to the temporary land subsidence using the GNSS data. The data were provided from the INACORS network of the Indonesian Geospatial Information Agency (BIG).

6.2 Data and Methods

6.2.1 GNNS data set

In the flood area, I identified at least 5 GNSS stations managed by BIG in the INACORS network. The 5 stations include CJKT in Jakarta, BAKO in Bogor, CBTU in Cibitung, CRKS in Cirakas, and CTGR in Tangerang. I obtained the GNSS data on the INACORS network in the RINEX format. I used the data over 7 days, from29th December 2019 to 4th January 2020 in order to see the phenomenon including the changes several days before and after the flood and heavy rain.

As described in Chapter 5, I used RINEX data to get tropospheric parameters using the goGPS open-source software, version 1.0 Beta from Geomatics Research and Development s.r.l. - Lomazzo, Italy, (Realini, 2009). The wet tropospheric delays are converted to PWV (Precipitable Water Vapor) every 30 seconds. Large PWV brings intensive rainfall, and the record-making rainfall data from BMKG on 1 January 2020 would have been associated with high PWV values. I also analyze the vertical crustal movements using coordinates obtained by analyzing the RINEX data using the goGPS software.

6.2.2 Land Subsidence in Jakarta

Secular land subsidence in Jakarta, due to urbanization, has been studied over a long time. For example, Andreas et al. (2019) showed that Jakarta, compared with major cities on the coast of other countries, occupies the first position in terms of land subsidence since 1920 until now (Figure 6.1). Jakarta is vulnerable to further land subsidence, especially when heavy rain occurs and rainwater pools to cause a flood.

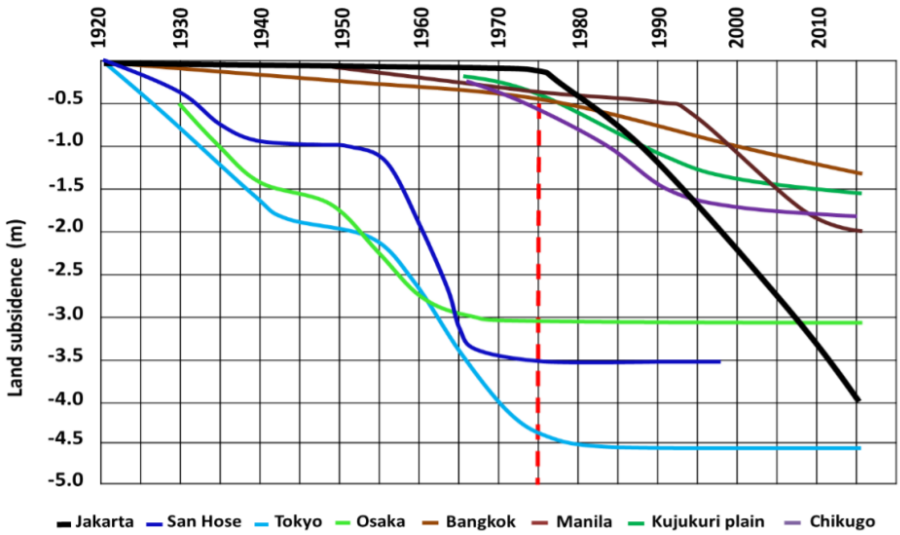

Figure 6.2, Land subsidence in several coastal city in different countries including Jakarta, Indonesia, from 1920 until recent years (Andreas et al., 2019).

In this study, I discuss the temporary land subsidence related to the occurrence of heavy rain on January 1, 2020, using the GNSS data analyzed with the open source software goGPS. When the heavy rain occurs, the water will gather at the surface of the land. This makes water loads to depress the ground surface and make it subside.

6.3 Result and discussions

6.3.1 Determination of PWV values at 5 INACORS stations.

As I did in Chapter 5 for the GNSS-meteorological studies, Here I try to study the crustal movements for the recent of heavy rainfall event in Indonesia on January 1, 2020. This rain caused severe flooding around the Jakarta area, and would be an appropriate case to study crustal deformation by surface rainwater load.

I analyzed the RINEX data obtained from INACORS-BIG network, using the goGPS open-source software package, as explained in Chapter 5. Before studying crustal deformation, I estimated the ZTD value, and then isolated the ZWD value, and converted the ZWD value into the PWV. In Figure 6.2, I show the result of the PWV time series at five INACORS stations evenly distributed within the flooded area on January 1, 2020.

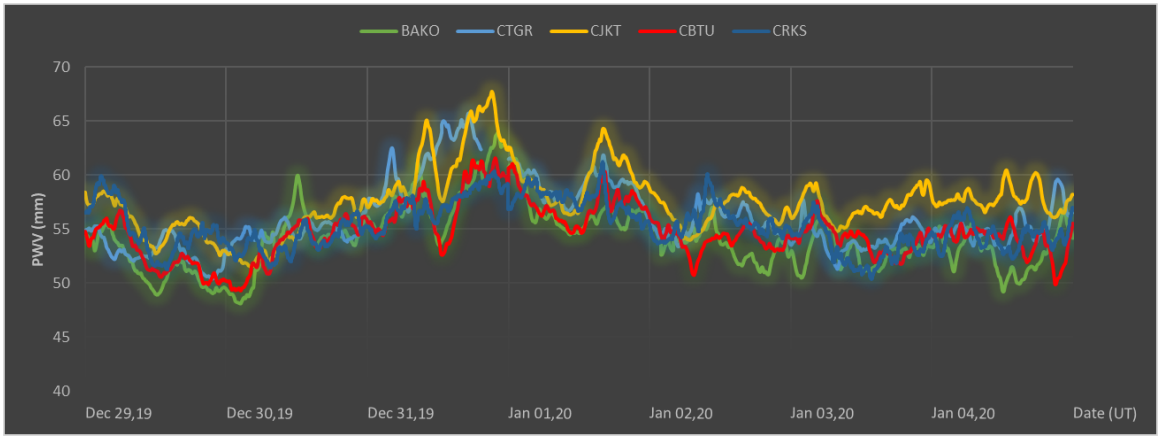

Figure 6.2. Time series of PWV values at 5 INACORS GNSS stations in the Jakarta flood area. The time spans from 29 December 2019 to 4 January 2020 (UT), and the highest PWV value occurred on December 31, 2019.

As seen in Figure. 6.2, the PWV values at the five GNSS stations show similar patterns even in spite of the average inter-station of ~30km. PWV values appear to increase in the middle of the day of 30 December 2019, and the peak occurred at the end of the day of 31 December 2019. This condition is consistent with the date of heavy rain as discussed in Section 6.2.

The PWV value showed a sudden drop in the middle of the day 1 January 2020. At the end of the day, PWV increased again, but not as high as the first peak. From January 2, 2020, PWV decreased and kept nearly constant until January 4. In this time range, there were two peak PWV occurrences. The first peak PWV of ~70 mm and the second peak of ~65 mm, and the largest PWV was recorded at the CJKT station.

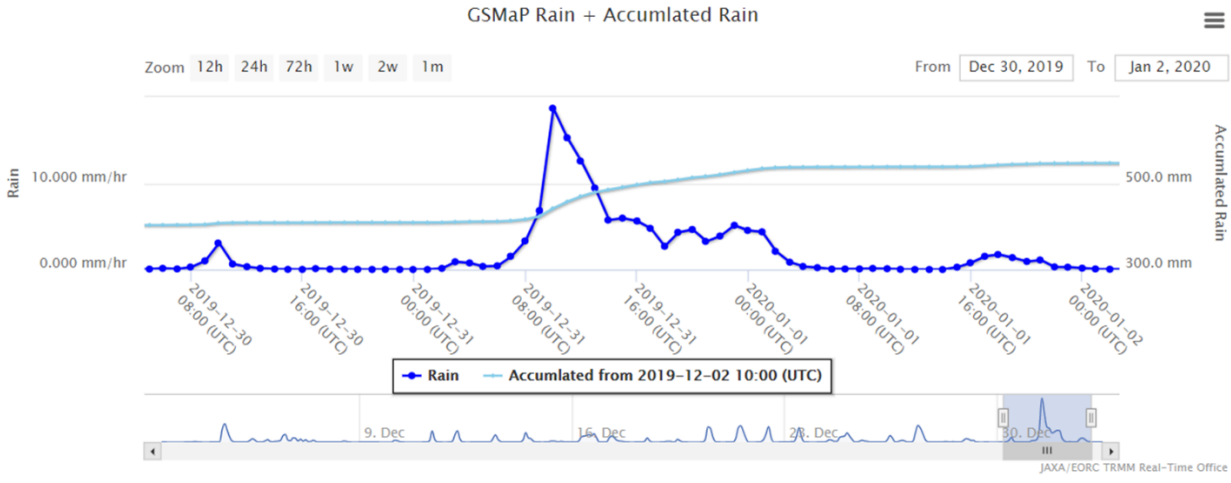

Figure 6.3. Rain rate and cumulative rain on December 31, 2019, according to the hourly rainfall data set from JAXA Global Rainfall Watch. The highest rainfall peak occurred around at 10.00 am (UT) on that day.

Next, I analyze the rainfall events on 31 December 2019, using data from JAXA Global Rainfall Watch, which offers hourly rainfall data. Figure 6.3 shows the hourly rainfall in the Jakarta and surrounding areas obtained from

this data set. The increase in rainfall starts at 07.00 (UT) until the peak at 10:00 (UT). Next, I compare this information with the hourly PWV values at GNSS stations shown in Figure 6.4,

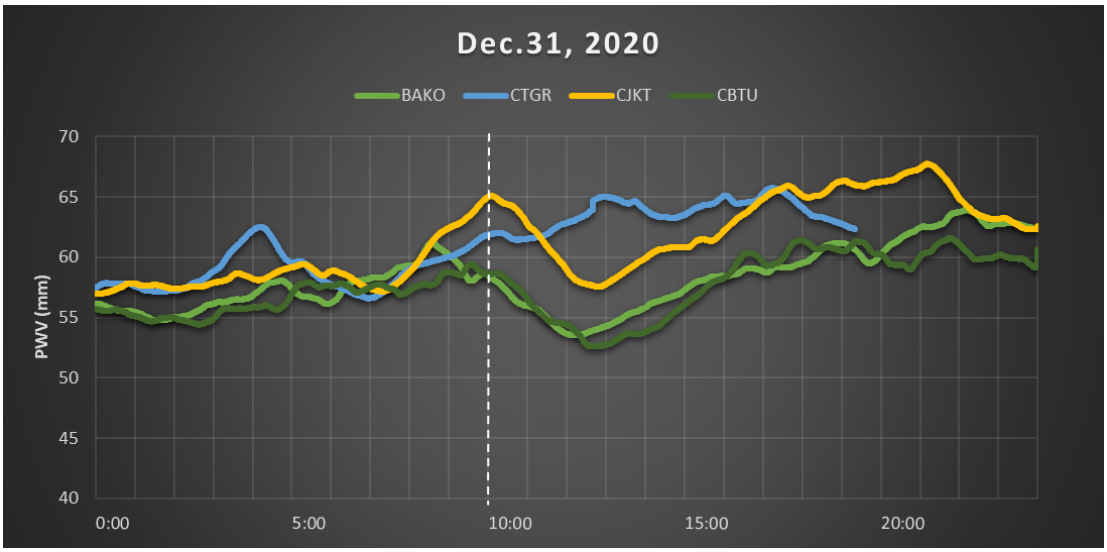

Figure 6.4. Hourly PWV values at 4 INACORS GNSS stations, BAKO, CTGR, CJKT, and CBTU stations during the day of December 31, 2019. PWV time series show maxima at 10.00, the peak rain rate time, at CJKT and BAKO stations.

As seen by comparing Figure 6.3 and Figure 6.4, the rainfall and PWV time series show consistent behaviors. This explains that the heavy rain peak occurs when the PWV value is at its peak. It also indicates that the heavy rain caused a sudden drop of PWV from 10:00 to 12:00, which means that water vapor changed into liquid water (heavy rain). This suggests that monitoring the GNSS-meteorology data from INACORS is useful as a meteorological observation.

6.3.2 Comparison of PWV INACORS with Jakarta Radiosonde Station

To compare the GNSS-PWV values with those by other sensors, I obtained the PWV data by radiosondes at BMKG, Jakarta. BMKG serves not only as the GNSS stations but also as a radiosonde station in Jakarta with the name WIII station. Its primary purpose is to serve for flight at the Soekarno Hatta Airport, Cengkareng, Jakarta. The radiosonde PWV data are compared with the PWV data obtained by an INACORS station in Jakarta CJKT in Figure 6.3.

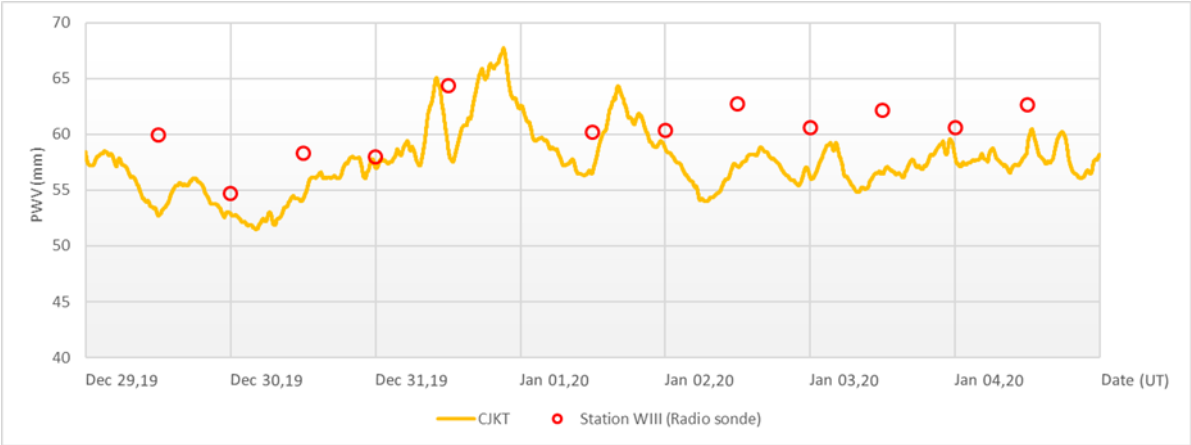

Figure 6.3 Comparison of PWV values between GNSS-PWV at CJKT stations estimated every 30 seconds (orange curve) and radiosonde-PWV recorded every 6 hours at the WIII station (red circle). Correlation coefficient between PWV data from GNSS and radiosonde is 0.541. The difference between the two stations is around 26 km.

The correlation between the two PWV values is not so high, probably because of the distance between the two stations. Nevertheless, at least the PWV from GNSS stations can complement the radiosonde data with their high spatial and temporal resolution.

6.3.3 Crustal movement analysis, GNSS station (INACORS-BIG)

Next, I test my hypothesis that temporary vertical movements of GNSS stations reflect, to some extent, surface loads such as rainwater. Here I estimate vertical positions of the GNSS stations to study vertical crustal movements during the floods on January 1, 2020, and heavy rains on December 31, 2019. I calculated vertical positions during a time span from 10 days before the flood (December 22-31 December 2019) to 9 days after the flood. (2-10 Jan 2020).

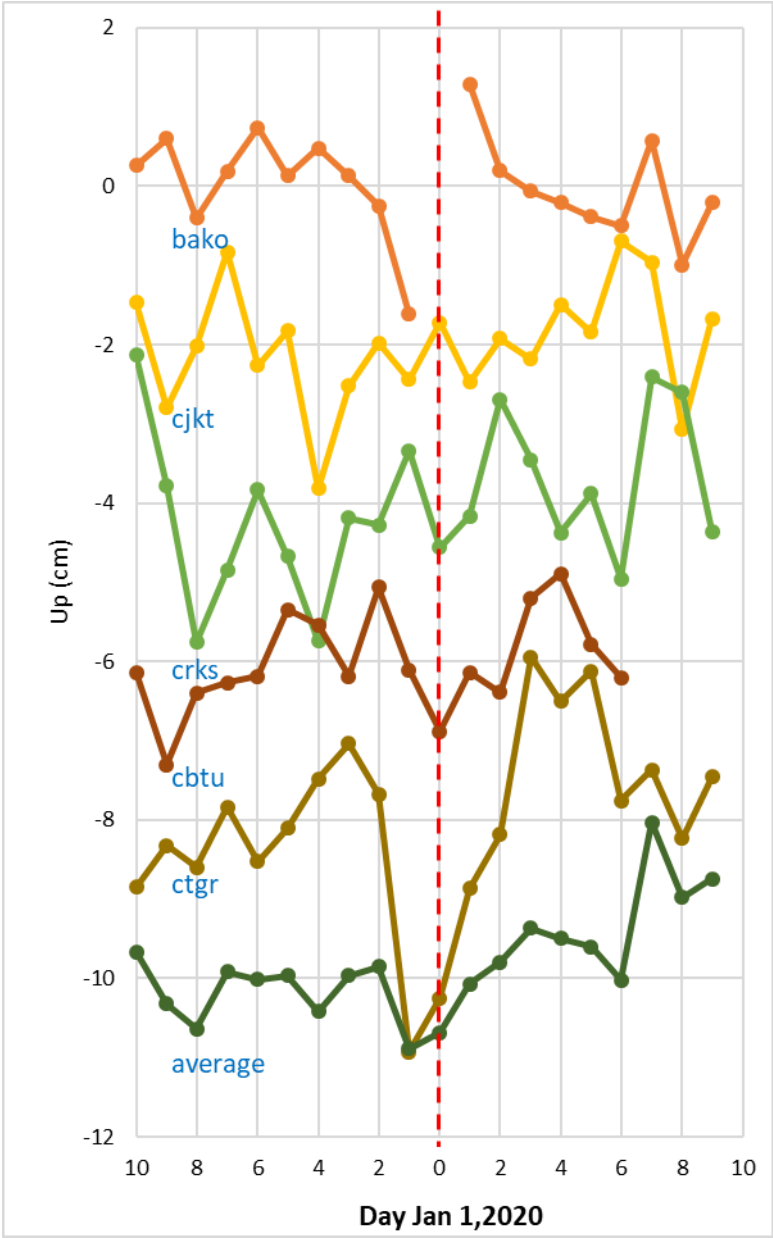

Figure 6.4, Vertical position time series over a period spanning 20 days for the 5 GNSS stations in the region flooded by the January 1st, 2020, Jakarta heavy rain. The station bako had a data interruption on January 1, 2020.

I used the GNSS data in RINEX format, with supporting data for the satellite ephemeris. The software outputs topocentric coordinates, composed of north-south, east-west, and vertical movement components. Here I am interested in the vertical movements, because the water load will depress the ground vertically. I plot the vertical coordinate time series in Figure 6.4. From the 5 GNSS-INACORS stations located in the Jakarta flood area, data on 1 Jan 2020 from the BAKO station could not be processed because the data had experienced an interruption during the acquisition process.

Figure 6.4 shows that the average vertical coordinates show significant subsidence of nearly 1 cm on December 31, 2019, and January 1, 2020. However, coordinates of the individual stations behave differently. For example,

subsidence on December 31, 2019 is clearly seen only at BAKO and CTGR stations. Subsidence on January 1, 2020 is clear for the CRKS, CTGR and CBTU stations. These stations are located in the flooded area (light blue colored region in Figure 6.1). On the other hand, CJKT is close to the coast and not included in the flooded area. Anyway, these results suggest that subsidence due to flood water load is quite non-uniform in space, and dense network would be needed to fully understand the crustal response to the surface stormwater load in Indonesia.

Chapter 7. Conclusion and Recommendation

7.1 Conclusion

The conclusions of this thesis are summarized as follows,

1. The atmospheric delay gradients are little influenced by station altitudes and provide useful information of spatial gradient of relative humidity in lower atmosphere. By using atmospheric delay gradients, I could estimate distributions of sea-level ZWD, reflecting relative humidity of the air column above the station. This is possible only in regions with dense GNSS networks like Japan because tropospheric delay gradients are related to horizontal spatial gradient of ZWD. I also showed the importance of the water vapor concentration (WVC) index, reflecting small scale enhancement of water vapor. As seen in the scatter diagrams in Figures 3.8 and 3.9, sea-level ZWD and WVC are not correlated, i.e., high sea-level ZWD does not always mean high WVC and vice versa. I showed that heavy rain occurs only when both quantities show high values.
2. The results suggest that monitoring these quantities is useful for the nowcast of heavy rains. However, their ability to forecast heavy rains is yet to be studied. As the next step, I will need to explore the way to use these two quantities for weather forecast, e.g., by putting them to numerical weather models by some means. Computation time of sea-level ZWD and WVC is short, and we can convert ZTD values estimated by GNSS data analysis in near real-time to sea-level ZWD and WVC.
3. Crustal subsidence was found to have occur by the water load brought by 2018 July SW Japan heavy rain, together with the heavy rains in 2017 July and 2019 August in the same area. In the day-to-day variability in crustal subsidence during 5-8 July 2018, I found a pattern of movement of the subsidence area from west to east in SW Japan. I have estimated the total water load using the crustal movement and compared them with the amount of precipitation from AMeDAS rain gauge data.
4. I used the open-source goGPS software to determine ZTD in Indonesia and found this software package quite useful in comparison with other commercial software packages in determining tropospheric parameters. ZTD values showed different behaviors for different seasons; in Indonesia, the value of ZTD tends to be high/low during a rainy/dry season.

5. I analyzed GNSS data from INACORS, a permanent GNSS network in Indonesia, to study tropospheric parameters and crustal subsidence. First, I determined the PWV values from GNSS data from Jakarta during the heavy rain event on January 1, 2020. Then, I confirmed their consistency with those by nearby radiosonde observations. Finally, I analyzed the crustal movement with the same GNSS data. The results showed vertical movements during the heavy rain episode in Jakarta, i.e. all of the GNSS stations in the Jakarta area showed significant changes from 31 December 2019 to 1 January 2020. They indicated that the flood in Jakarta caused temporary land subsidence.

7.2 Recommendation

1. The first recommendation from this thesis is for GNSS meteorology in Japan. From what I have done, the quality of numerical weather prediction may further improve by monitoring water vapor concentration index together with PWV converted to sea-level values. For this purpose, real-time calculation of these quantity would contribute.
2. The second recommendation is for the Indonesian GNSS meteorology, especially for BIG as an institution that manages GNSS in Indonesia. I recommend them to schedule workshops for the GNSS meteorology researches in Indonesia, and to start a long-term joint project aimed at the realization of GNSS meteorology in Indonesia.

Bibliography

Andreas, H. et al (2019) IOP Conf. Ser.: *Earth Environ. Sci*. 389 012034

Arief, S., and Heki, K. (2020). GNSS Meteorology for Disastrous Rainfalls in 2017–2019 Summer in SW Japan: A New Approach Utilizing Atmospheric Delay Gradients. *Front. Earth Sci*. 8, doi: 10.3389/feart.2020.00182

Askne, J., and H. Nordius (1987). Estimation of tropospheric delay for microwaves from surface weather data. *Radio Sci*. 22, 379–386. doi:10.1029/RS022i003p00379

Baby, H. B., P. Golé, and J. Lavergnat (1988). A model for the tropospheric excess path length of radio waves from surface meteorological measurements. *Radio Sci*. 23, 1023-1038.

Bevis, M., Businger, S., Herring, T. A., Rocken, C., Anthes, R. A., and Ware, R. H. (1992). GPS meteorology: remote sensing of atmospheric water vapor using the global positioning system. *J. Geophys. Res.* 97, 15787–15801.

Bevis, M., S Businger, and S. Chiswell (1994). GNSS meteorology: mapping zenith wet delays onto precipitable water. *Journal of Applied Meteorology*. 33(3), 379-386.

Blewitt, G., Hammond, W. C., and Kreemer, C. (2018). Harnessing the GPS data explosion for interdisciplinary science. *EOS* 99, 1–2. doi: 10.1029/2018EO104623

Böhm, J., Niell, A., Tregoning, P., and Schuh, H. (2006a). Global Mapping Function (GMF): a new empirical mapping function based on numerical weather model data. *J. Geophys. Res.* 33, 3–6. doi: 10.1029/2005GL025546

Böhm, J., and Schuh, H. (2013). Atmospheric Effects in Space Geodesy, p. 243, *Springer Berlin Heidelberg*.

Brenot, H., Neméghaire, J., Delobbe, L., Clerbaux, N., De Meutter, P., Deckmyn, A., et al. (2013). Preliminary signs of the initiation of deep convection by GNSS. *Atmos. Chem. Phys.* 13, 5425–5449. doi: 10.5194/acp-13-5425-2013

Businger, S., S. R. Chiswell, M. Bevis, J. Duan, R. A. Anthes, C. Rocken, R. H. Ware, M. Exner, F. S. Solheim (1996). The promise of GNSS in atmospheric monitoring. *Bull. Am. Meteorol. Soc*. 77, pp. 5-18.

Chao, C. C. (1974). The troposphere calibration model for mariner mars 1971. *Technical Report* 32-1587 pp. 61-76. NASA JPL. Pasadena. CA.

Chen, G., and Herring, T. A. (1997). Effects of Atmospheric Azimuthal Asymmetry on the Analysis of Space Geodetic Data. *J. Geophys. Res.* 102, 20489–20502. doi: 10.1029/97jb01739

Davis, J. L., T. A. Herring, I. I. Shapiro, A. E. E. Rogers, and G. Elgered (1985). Geodesy by radio interferometry effects of atmospheric modeling errors on estimates of baseline length. *Radio Sci*. 20, 1593-1607.

Duan J, et al. (1996). GPS meteorology: Direct estimation of the absolute value of precipitable water. *Journal of Applied Meteorology*. 35, 830-838.

Enge, P., and Misra, P. (2006). Global Positioning System (2 ed.). *Ganga-Jamuna Press*.

Farrell, W. E. (1972). Deformation of the Earth by surface loads. *Res. Geophys*. 10, 761-797.

Foelsche, U., and G. Kirchengast (2001). Tropospheric water vapor imaging by combination of ground-based and spaceborne GNSS sounding data. *Journal of Geophysical Research D: Atmospheres*. 106, 27221-27231.

Gabor, M. (1997). Remote Sensing of Water Vapor from GNSS Receivers. Retrieved May 16, 2018 http://www.csr.utexas.edu/texas_pwv/midterm/gabor/gabor.html#anchor561367

Gérard, P., and Luzum, B. (2010). *IERS Conventions 2010.* France: Bureau International Des Poids Et Mesures Sevres, 1–179.

Hall, M. P. M., B. L. W., and H. M. T. (1996). Propagation of radiowaves, Institution of Electrical Engineers, London.

Heki, K. (2001). Seasonal modulation of interseismic strain buildup in northeastern Japan driven by snow load. *Science vol.*293.5527 Pages 89-92.

Heki, K. (2004). Dense GNSS array as a new sensor of seasonal changes of surface loads, in "The State of the Planet: Frontiers and Challenges in Geophysics," edited by R.S.J. Sparks and C. J. Hawkesworth, Geophys. Monograph, 150, 177-196, American Geophysical Union, 2004.

Heki, K. (2020). Geodesy in Japan: Legends and highlights. *Earth Planets Space*, 72, 38, DOI:10.1186/s40623-020-0116408

Hopfield, H. S. (1969). Two-quartic tropospheric refractivity profile for correcting satellite data, *J. Geophys. Res*. 74. 4487-4499.

Hopfield, H. S. (1971). Tropospheric effect on electromagnetically measured range. Prediction from surface weather data. *Radio Sci*. 6, 357-367

Iwabuchi, T., Miyazaki, S., Heki, K., Naito, I., and Hatanaka, Y. (2003). An impact of estimating tropospheric delay gradients on tropospheric delay estimations in the summer using the Japanese nationwide GNSS array. *J. Geophys. Res*. 108. 10.1029/2002JD002214

Japan Meteorological Agency [JMA] (2019). *A Heavy Rain Episode Brought by a Stationary Front (2019 Aug. 26-29).* Tokyo: Japan Meteorological Agency.

Japan Meteorology Agency [JMA] (2017). *On the 2017 July Heavy Rain in Northern Kyushu.* Tokyo: Japan Meteorological Agency.

Japan Meteorology Agency [JMA] (2018). *2018 July Heavy Rain (heavy rain etc, by the stationary front and the typhoon no. 7).* Tokyo: Japan Meteorological Agency.

Kleijer, F. (2004). Troposphere modeling and filtering for precise GNSS leveling. *PhD dissertation*, Delft University of Technology, Delft, The Netherlands.

Koning, A. (2016). Precipitable water vapor estimation using GNSS in Uganda: A study on obtaining the Zenith Wet Delay. PhD dissertation, Delft, The Netherlands

Kouba, J. (2009). Testing of global pressure/temperature (GPT) model and global mapping function (GMF) in GNSS analyses. *Journal of Geodesy*. 83, 199-208.

Lagler, K., M. Schindelegger, Böhm, J., H. Krásná, and T. Nilsson (2013). GPT2: Empirical slant delay model for radio space geodetic techniques. *Geophys. Res. Lett*. 40, 1069-1073.

Langley, R. B. (1999). Dilution of precision. *GPS World*. 10, 52-59

Leandro, R. F., Langley, R. B., and Santos, M. C. (2008). UNB3m_pack: A neutral atmosphere delay package for radiometric space techniques. *GPS Solutions*. 12, 65-70.

MacMillan, D. S. (1995). Atmospheric Gradients from very long baseline interferometry observations. *Geophys. Res. Lett.* 22, 1041–1044. doi: 10.1029/95GL00887

Meindl, M., Schaer, S., Hugentobler, U., and Beutler, G. (2004). Tropospheric Gradient Estimation at CODE: Results from Global Solutions, in Applications of GPS Remote Sensing to Meteorology and Related Fields. *In Journal of the Meteorological Society of Japan*, 82, 331 – 338.

Mendes, V. B., and Langley, R. B. (1999), Tropospheric zenith delay prediction accuracy for high-precision GNSS positioning and navigation. *Navigation. 46, 25-34.*

Milliner, C., Materna, K., Burgmann, R., Fu, Y., Moore, A.W., Bekaert, D., Adhikari, S., Argus, D.F. (2018). Tracking the weight of Hurricane Harvey's stormwater using GNSS data. *Sci Adv* 4, eaau2477.

Miyazaki, S., Iwabuchi, T., Heki, K., and Naito, I. (2003). An impact of estimating tropospheric delay gradients on precise positioning in the summer using the Japanese nationwide GPS array. *J. Geophys. Res.* 108:4315. doi: 10.1029/2000JB000113

Mohr, P. J., B. N. Taylor, and D. B. Newell (2012). CODATA recommended values of the fundamental physical constants: 2010, REVIEWS OF MODERN PHYSICS. *Rev Mod Phys*. 84, 1527

Nakagawa, H., Toyofuku, T., Kotani, K., Miyahara, B., Iwashita, C., Kawamoto, S., et al. (2009). Development and validation of GEONET new analysis strategy (Version 4). *J. Geogr. Surv. Inst.* 118, 1–8.

Owens, J. C. (1967). Optical refractive index of air: dependence on pressure, temperature, and composition. *Applied Optics*. 6, 51-59.

Patel, K. (2020). Torrential Rains Flood Indonesia.*https://earthobservatory.nasa.gov/images/146113/torrential-rains-flood-indonesia.*

Realini, E. (2009). goGPS free and constrained relative kinematic positioning with low-cost receivers. Ph. D. thesis, http://www.researchgate.net/publication/237520116

Ruffini, G., Kruse, L. P., Rius, A., Biirki, I. B., and Cucurulll, L. (1999). A Flores. "Estimation of Tropospheric Zenith Delay and Gradients over the Madrid Area Using GPS and WVR Data.". *Geophys. Res. Lett.* 26, 447–450. doi: 10.1029/1998gl900238

Saastamoinen, J. (1972). Atmospheric correction for troposphere and stratosphere in radio ranging of satellites. The Use of Artificial Satellites for Geodesy. In *Papers presented at the Third International Symposium on The Use of Artificial Satellites for Geodesy*, Eds. S. W. Henriksen, A. Mancini, B. H. Chovitz, AGU, AIAA, NOAA, U.S.ATC, Washington, D. C., 15-17 April 1971, American Geophysical Union, Washington, D. C., Geophysical monograph 15, pages 247 – 252.

Saastamoinen, J. (1973). Contributions to the theory of atmospheric refraction part II. *In Bull. Geod*. 107, 13–34.

Shoji, Y., T. Iwabuchi, Y. Hatanaka, H. Seko, R. Ichikawa, R. Ohtani, and N. Mannoji. 2009. GNSS Meteorology: Research on the Construction of GNSS Water Vapor Information System and Application to Meteorology, Geodesy, and Hydrology. *Journal of the Geodetic Society of Japan* 55, 17–38.

Shoji, Y. (2013). Retrieval of water vapor inhomogeneity using the Japanese Nationwide GPS array and its potential for prediction of convective precipitation. *J. Meteorol. Soc. Jpn.* 91, 43–62. doi: 10.2151/jmsj.2013-103

Shoji, Y. (2015). Water vapor estimation using ground-based GNSS observation network and its application for meteorology. *Tenki* 62, 3–19.

Shoji, Y., K. Sato, M. Yabuki, and T. Tsuda, (2017). Comparison of shipborne GNSS-derived precipitable water vapor with radiosonde in the western North Pacific and in the seas adjacent to Japan. *Earth Planets Space*. 69, 153.

Smith, E. K., and S. Weintraub (1953). The constants in the equation for atmospheric refractive index at radio frequencies. *Proceedings of the IRE*. 41, 1035-1037.

Sturman, A. P., and N. J. Tapper (2006). The weather and climate of Australia and New Zealand, 2nd ed., pp. 520, Oxford University Press.

Thayer, G. D. (1974). An improved equation for the radio refractive index of air. *Radio Sci.* 9, 803-807.

Tsuda, T., Heki, K., Miyazaki, S., Aonashi, K., Hirahara, K., Nakamura, H., et al. (1998). GPS meteorology project of Japan – Exploring frontiers of geodesy -. *Earth Planet. Space* 50, 1–5.

Tsuji, H., and Hatanaka, Y. (2018). GEONET as Infrastructure for Disaster Mitigation. *J. Dis. Res.* 13, 424–432. doi: 10.20965/jdr.2018.p0424

Vaclavovic, P., and Dousa, J. (2015). Backward Smoothing for Precise GNSS Applications. *Adv. Space Res.* 56, 1627–1634. doi: 10.1016/j.asr.2015.07.020

Ware, R., Exner, M., Feng, D., Gorbunov, M., Hardy, K., Herman, B., Kuo, Y., Meehan, T., Melbourne, T., Rocken, C., Schreiner, W., Sokolovskiy, S., Solheim, F., Zou, X., Anthes, R., Businger, S., Trenberth, K. (1996). GPS Sounding of the Atmosphere from Low Earth Orbit: Preliminary Results. *Bull. Amer. Meteor. Soc.* 77, 19 - 40. https://doi.org/10.1175/1520-0477(1996)077<0019:GSOTAF>2.0.CO;2

Xu, G. (2007). GNSS: Theory Algorithms and Applications 2nd ed. *Springer*, Heidelberg.

Yan, S., Z. Li, K. Yu, and K. Zhang (2014). GNSS-R L1 interference signal processing for soil moisture estimation: an experimental study. *EURASIP Journal on Advances in Signal Processing*. 2014, 107

Yedukondalu, K. A. S. (2011). Estimation and Mitigation of GNSS Multipath Interference Using Adaptive Filtering. *Progress in Electromagnetics Research* M, 133-148.

Yuan, Y., Zhang, K., Rohm, W., Choy, S., Norman, R., and Wang, C. (2014). Real-Time Retrieval of Precipitable Water Vapor from GNSS Precise Point Positioning. *J Geophys Res. Atmos.* 119 ,10044–57. https://doi.org/10.1002/2014JD021486

Zinas, N. (2019). Satellite and receiver clock errors. Retrieved from *Tekmon Geomatics*, http://www.tekmon.eu/1-3-2-satellite-and-receiver-clock-errors/.

Zumberge, J. F., Heftin, M. B., Jefferson, D. C., Watkins, M. M., and Webb, F. H. (1997). Precise point positioning for the efficient and robust analysis of GPS data from large networks. *J. Geophys. Res.* 102, 5005–5017. doi: 10.1029/96JB03860.

Zus, F., Douša, J., Kaèmaøík, M., Václavovic, P., Balidakis, K., Dick, G., et al. (2019). Improving GNSS Zenith Wet Delay Interpolation by Utilizing Tropospheric Gradients: Experiments with a Dense Station Network in Central Europe in the Warm Season. *Remote Sens.* 11:674. doi: 10.3390/rs11060674